Imperial College London
Department of Physics

Development of high repetition rate intense laser driver and laser driven particle sources

Nuo Xu

Imperial College London

Submitted in part fulfilment of the requirements
for the degree of Doctor of Philosophy at
Imperial College London, October 2023



I hereby certify that the material of this thesis, which I now submit for the award of Doctor of Philosophy, is entirely my own work unless otherwise cited or acknowledged within the body of text.

Nuo Xu (2023)

The copyright of this thesis rests with the author. Unless otherwise indicated, its contents are licensed under a Creative Commons Attribution-Non Commercial-No Derivatives 4.0 International Licence (CC BY-NC-ND).

Under this licence, you may copy and redistribute the material in any medium or format on the condition that; you credit the author, do not use it for commercial purposes and do not distribute modified versions of the work.

When reusing or sharing this work, ensure you make the licence terms clear to others by naming the licence and linking to the licence text.

Please seek permission from the copyright holder for uses of this work that are not included in this licence or permitted under UK Copyright Law.

Abstract

This thesis covers a novel experiment in high repetition rate ion acceleration with high intensity solid state lasers. In particular, it discusses the design and realisation of previously unexplored energy level from a high repetition rate laser. It also discuss high repetition rate capable solid target delivery systems. These laser driven accelerator operating conditions are of interest to many novel applications that are detailed in this thesis. The thesis discusses results of a stable 100Hz 20TW high repetition rate femtosecond laser, which can be adapted to laser driven particle acceleration for application in specific fields such as imaging, radioisotope generation, and proton therapy. A remarkably stable (better than 1% energy jitter) laser system was designed and developed. The laser was ran without supervision for over 1 million full energy shots. Key to the performance was the implementation of cryogenic laser amplifier stages featuring completely passive UHV pumping system which is thus vibration free. These different feature of the high repetition rate laser will be analysed and discussed, and modelled.

The thesis also includes the results from recent experiments studying the interaction of an intense 0.8 µm laser with a solid target at high repetition rate, generating energetic particles. The thesis will include analysis of the plasma at high repetition rate, and discussion of the plasma diagnostic systems involved to achieve such through-put, including the potential for future work on rapid data sampling and image processing with FPGAs.

Acknowledgements

I wish to extend my deepest gratitude to my supervisor, Professor Zulfikar Najmudin, whose invaluable guidance and support have been instrumental in my research.

I find it crucial to acknowledge the self-financed aspect of this academic pursuit. My gratitude is extended to myself and my parents for providing the indispensable financial backing, which has been crucial to the successful execution of this research project.

I would be remiss if I did not extend my heartfelt thanks to my esteemed colleague, Dr. Oliver Ettlinger. His expert advice and extensive knowledge in the field of high-power lasers have greatly enriched my research experience.

I extend my sincere gratitude to Dr. Jonathan Wood for his exemplary coordination with technical support staff and suppliers. His outstanding management skills were demonstrated under challenging conditions. His unwavering commitment and leadership have been invaluable to the success of this thesis. Dr. Wood's invaluable insights on beam-driven plasma accelerators, leveraging his vast expertise gained from his previous work at DESY, combined with his work experience at DESY, Germany, has not only broadened but revolutionised the scope of my view of academic career.

Finally, I would like to give my sincere appreciation to our research collaborators from the Central Laser Facility, the John Adams Institute for Accelerator Science, and the Kansai Institute for Photon Science. Their collaboration has been invaluable in broadening the scope and enriching the quality of my research.

Contents

Abstract **3**

Acknowledgements **4**

1 Introduction **13**
1.1 Laser driven plasma accelerators . . . 13
1.2 Intense laser sources . . . 14
1.3 Potential use of high repetition rate laser driven particle sources . . . 15
1.3.1 Industrial and clinical imaging . . . 15
1.3.2 Hadron therapy . . . 16
1.4 Challenges in laser driven source properties . . . 17
1.5 Thesis summary and author's contributions . . . 17
1.6 List of Publications . . . 18
References . . . 21

2 Intense laser sources, theory and review **27**
2.1 Short pulse laser sources . . . 27
2.1.1 Q-switching . . . 28
2.1.2 Mode locking . . . 29
2.1.3 Chirp pulse amplification . . . 30
2.1.4 Gain medium for wide-band operation . . . 30
2.1.5 High repetition rate sources . . . 33
2.2 Short pulse laser diagnostics . . . 33
2.2.1 Wavefront sensing and adaptive optics . . . 34
2.2.2 Beam monitoring and compensation . . . 37
References . . . 40

3 Theory of laser-plasma ion accelerators **45**
3.1 Plasma theory . . . 45
3.1.1 Plasma frequency . . . 45
3.1.2 Dispersion relation . . . 46
3.1.3 Critical density . . . 46
3.1.4 Debye length . . . 47
3.2 Laser plasma interaction . . . 48
3.2.1 Field ionisation and Collision ionisation . . . 48
3.2.2 Single electron motion in E-M field and normalised vector potential . . . 49
3.2.3 Ponderomotive force . . . 51
3.2.4 Self-focusing . . . 52

3.3 Ion acceleration with intense laser . . . 53
3.3.1 Acceleration schemes . . . 53
3.3.2 Sheath acceleration . . . 54
3.3.3 Radiation pressure acceleration . . . 56
References . . . 58

4 High repetition rate laser source development and characterisation 61
4.0.1 System overview . . . 61
4.1 Ti:sapphire regenerative amplifier . . . 63
4.1.1 Thermal lensing and cavity stability . . . 64
4.1.2 Cryogenic regenerative amplifier . . . 69
4.2 Diode pumped high repetition rate YAG laser . . . 75
4.2.1 Gain module thermal lensing characterisation and compensation . . . 76
4.2.2 Single and double pass configuration efficiency . . . 77
4.2.3 Thermal depolarisation compensation . . . 78
4.2.4 Diffractive diffuser . . . 81
4.3 Multi-pass cryogenic Ti:sapphire amplifier . . . 83
4.3.1 Thermal lensing characterisation and design . . . 83
4.3.2 High load cryogenic amplifier . . . 84
4.4 Vacuum compressor with hybrid grating . . . 86
4.4.1 High rigidity grating mount . . . 87
4.4.2 Damage threshold testing . . . 90
4.5 Wavefront sensing . . . 91
4.5.1 Shack Hartmann . . . 91
4.5.2 Diffractive elements . . . 92
4.5.3 Diffractive element array based wavefront sensor design . . . 94
4.5.4 Image sensor . . . 96
4.5.5 Thermal design . . . 97
4.5.6 Wavefront sensor characterisation . . . 98
4.5.7 Sensitivity evaluation . . . 100
4.5.8 Performance conclusion . . . 101
4.5.9 Future directions for pinhole array based wavefront sensor . . . 102
4.5.10 Wavefront measurement on short pulse laser . . . 102
References . . . 104

5 High repetition rate targetry 109
5.1 High repetition rate target diagnostics . . . 109
5.1.1 White light confocal - CHROCODILE . . . 109
5.1.2 Heterodyne interferometry . . . 110
5.2 Tapedrive . . . 110
5.2.1 Introduction to tape target . . . 111
5.2.2 Tape target design background . . . 112
5.2.3 Thermal considerations . . . 114
5.2.4 Modal analysis and motor tuning . . . 114
5.2.5 Electronics for high repetition rate targetry . . . 116
5.2.6 Motor selection . . . 117
5.2.7 Mechanical design and manufacturing . . . 119
5.2.8 Review of characterising methods for tape-drive performance . . . 120

5.2.9 Tape-drive performance in a real world laser–plasma interaction setup . . 121
5.2.10 Experimental use of the developed tape target 124
References 129

6 High repetition rate ion sources and diagnostics 135
6.1 Brief review of experimental results at high repetition rate 135
6.2 Experimental setup 136
6.3 High repetition rate ion diagnostic methods 139
6.4 Time-of-flight data and artifact mitigation 140
6.5 Ion energy comparing 3 different polarisations 146
References 152

7 Conclusion and Future work 155
7.1 Conclusions 155
7.2 Future works 156
7.2.1 Regenerative amplifier 156
7.2.2 Multi-pass amplifier 156
7.2.3 Tape target 157
7.2.4 ToF 157
7.2.5 Target position on-shot monitoring 157
7.2.6 High repetition rate support diagnostics 158
References 158

List of Tables

4.1 Statistical results from regenerative amplifier, comparison between cryogenic and water cooled amplifier with same pumping condition. 73
4.2 Comparison of different sensors. 96

5.1 Positional jitter for various tape materials. The 50 µm Kapton tape exhibited the best RMS performance at 0.28 µm. Limitations in surface quality samples restricted optimal tape-drive performance assessment. Previously published by author in 2023 [7]. 123

List of Figures

1.1 High repetition rate proton acceleration experiment using sub-1 µm stability solid target delivery system and sub - 1% (RMS) energy stability driver laser described in this thesis, operating at 100 Hz. 15

2.1 0.7 Joule 100 Hz Q-switched pump laser and its amplifier, used to pump a Ti:sapphire amplifier, described in chapter 4 29
2.2 Illustration of wavefront 35
2.3 Abberated wavefront and focal spot 35

3.1 Example of the shielded and unshielded Coulomb potentials, both stemming from a point test charge $q_t = +e$. 48
3.2 Single electron motion in static (left) and drift frame (right) 50
3.3 Ponderomotive energy, at different a_0 commonly achieved using focused Ti:sapphrie lasers. 52
3.4 TNSA process 54

4.1 System diagram of high repetition rate laser. 61
4.2 Oscillator and stretcher performance. 63
4.3 Block diagram, regenerative amplifier 64
4.4 Thermal image of an water cooled Ti:sapphire crystal with pumping load, local heating can be observed where absorption of pump energy occurs 65
4.5 Comparison of Water-Cooled Crystal Mounts: On the left, a traditional design prevalent in low repetition rate amplifiers, featuring a loosely fitted crystal without controlled clamping force. On the right, an advanced design with optimised thermal performance, incorporating controlled clamping pressure and a refined low surface roughness contact area. 66
4.6 COMSOL simulation with ray tracing and ray heating, pumping with 500 mJ laser at 100 Hz, 12 mm diameter crystal at 15 mm in length 67
4.7 Thermal lensing radius calculation 67
4.8 Regen cryogenic amplifier CAD design and operation. 69
4.9 Example of poor vacuum level during cryogenic operation. Crystal coating gradually deteriorate after only about 1 million shots. 70
4.10 Bulk material and coating damage due to poor vacuum cleanliness and trapped volumes 71
4.11 Optical damage crater under microscope, showing suspected carbon residual, scratches were due to post damage cleaning attempts 71
4.12 Output beam profile of cryogenically cooled regenerative amplifier. 12 mJ output pumped with 100 mJ 532nm laser at 100 Hz. 72
4.13 performance at 12mJ, 0.9% RMS stability under good vacuum conditions. . . . 74

4.14 performance at 8mJ after cleaning Pockel cell. No visible drift is observed after many days of operation, 2 to 4 hour each day, and was only interrupted by lab air conditioning unit failure. 74
4.15 DPSS side pumped QCW Gain module setup, with LBO as frequency doubling crystal. 75
4.16 Thermal lensing and depolarisation of a YAG laser amplifier for pumping high repetition rate Ti:sapphire amplifier. From left to right shows output beam profile at 0% to 100% thermal loads. Pumping with laser diode array operating at 100 Hz 76
4.17 Gain module measured thermal lensing focal length 77
4.18 Gain module output energy at single pass and double pass configuration, outputing 690 mJ at 100 Hz with 2 passes, seeding with 120 mJ. 78
4.19 Gain module fundamental output power added efficiency at single pass and double pass configuration. 78
4.20 Depolarisation return beam damaging polarised beam splitter cube, also ablating Faraday isolator housing. 79
4.21 Gain module measured depolarisation ratio, with and without Faraday rotator, demonstrating the large depolarisation gain when operating at 100 Hz, compared to 25 Hz. 80
4.22 Gain module block diagram with depolarisation and thermal lensing compensation 81
4.23 Pump profile at crystal plane, hot spots are due to intrinsic property of diffractive diffuser 82
4.24 Comparison of a poor nearfield profile from a commercial YAG laser, before and after a diffrative element diffuser 82
4.25 Simulated beam size at different point of the 4-pass amplifier with 100Hz 460 mJ pumping 83
4.26 4-pass amplifier CAD design and assembled during initial pumping 84
4.27 Recessed window to maximise acceptance angle for optimum pumping geometry 85
4.28 4 pass amplifier output beam profile, 60 mJ 86
4.29 Drawing for vacuum compatible grating mount, consisting of rotational joints from elastically averaged balls with high stiffness highlighted in blue. 88
4.30 Setup drawing for vacuum compressor with rigid grating mounts and roof mirror mount 89
4.31 Rigid grating mount with preloaded angular contact bearing pairs, providing elastic averaging of motions and high stiffness under small signal vibration conditions. The mounts are loaded with hybrid dialectric gratings, and vacuum compatible picomotors. 90
4.32 Hybrid dielectric grating laser induced damage 91
4.33 Illustration of wavefront detection 92
4.34 Pinhole image of a localised wave direction 92
4.35 Airy's disk 93
4.36 Ansys Zemax was utilised to design the optimal pinhole size and pinhole spacing, with realistic wavefront including spherical aberration and near-field distribution. 95
4.37 Size comparison of different commercially available silicon based focal plane arrays 96
4.38 Comsol was used to simulate 2 W absorbed optical power on a 50 micron pinhole array with adjustable mount 97
4.39 Optical CMM measurement of laser drilled hole sample 98
4.40 Calibration of wavefront sensor with beam expander and diode laser 99

4.41 Calibration of pinhole array geometry, some distortion and pinhole irregularity can be noticed 100

4.42 Sensitivity evaluation in air, mostly due to air turbulence 101

4.43 Measuring femtosecond laser with 4mJ of energy, using commercially available portable mirror-less camera and permanently mounted pinhole array mask . . . 103

5.1 CHROCODILE white light confocal measurement setup 110

5.2 Modal Response of the Tape Drive at 122.9 Hz: A finite element analysis highlighting the displacement of tape drive components under resonant oscillations, fixed to a rigid breadboard. The associated structural resonant frequency modes are enumerated. A relative displacement amplitude is used as colour bar, normalised peak amplitude to 1. 115

5.3 CHRocodile measured target tape vibrations during tape drive start-up, indicated by the red arrow. Background noise and intrinsic breadboard vibrations are evident before 10 seconds. After start-up, tape surface position is tracked for slightly over 1 minute. The entire measurement, sampled every 15 microseconds, is shown in blue, while a low-pass filtered signal with a 1 Hz cut-off illustrates long-term drift behavior. 117

5.4 Optical profiling of the 12.7 μm Kapton tape through high magnification microscopy (left) and white light interferometry (right) reveals bubble defects visible as dark spots on the left. The right image's unevenness results from the tape being measured without tension. Figure previously published by author in 2023 [7].121

5.5 Using the Precitec CHRocodile, tape jitter was assessed over 1 minute at varying speeds. The red line depicts the tape's low-frequency (< 1 Hz) motion. RMS positional variation is specified in each subplot. In c), oscillations arise from the tape drive's resonance. Speeds exceeding 8 mm/s yield lower jitters because of diminished stepper motor resonances [39]. Stated tape speeds relate to the smallest motor setting and spool diameter (16 mm). As the spool's radius grows, speed can triple [7]. 123

5.6 Tape jitter was measured with the Precitec CHRocodile over 1 minute at 2 mm/s. Except the top-left, all measurements targeted the laser interaction point. The top-left gauged the brass plate's stability. The red arrow marks the drive's activation. The blue line, sampled every 15 microseconds, shows surface roughness effects. The red line displays the tape's low-frequency (< 1 Hz) motion [7]. 124

5.7 Using the Precitec CHRocodile, tape guide surface stability was evaluated at 125 mm/s, maximising potential thermal drift effects. The blue line shows measurements with a 0.2 s sampling period, capturing room vibrations. The red line reflects the tape-drive support's low-frequency (< 50 mHz) thermal drift, influenced by laboratory temperature fluctuations from the air conditioning loop [7]. 125

5.8 Experimental setup illustrates the target and diagnostics. The laser hit at 30° to the target normal, with the electron spectrometer capturing forward-accelerated electrons. The proton scintillator, aligned with the rear target-normal, had a centre hole for the TOF diode. The tape drive was movable along the target normal, employing an off-axis diagnostic for on-shot target plane positioning [7]. 125

5.9 a) Proton average profile from ten shots on 50 μm Kapton tape at $z_T = 0$, captured using an EJ-440 scintillator 16 cm away. It was filtered with 6 μm aluminised Mylar. Dark stripes have additional aluminium filters, with a horizontal hole for rear diagnostics. The time-of-flight spectrometer's axis is marked by a white star. b) Proton spectra for each shot (grey), their mean (red line), and RMS (red shade) from a diamond-diode 36 cm away at 3°. Laser intensity fluctuated by 5%, but the laser-plasma interaction led to proton flux variations [7]. 127
5.10 Waterfall plot displays the normalized forward electron spectrum from 50 μm Kapton tape, integrated over 35 μSr. Negative z values indicate laser pulse arrivals before its best focus on the tape. Each strip represents a single-shot spectrum at its z position, incremented by 10 μm across 10-shot bursts. Red lines delineate burst boundaries; shots at $z_T = 0$ align with those in Figure 5.9. Published previously by author [7]. 128

6.1 Experimental setup in 3D drawing [6]. 137
6.2 Experimental setup for manipulating polarisation [6]. 137
6.3 Experimental setup in 3D drawing and still image captured during experiment [6]. 138
6.4 Focal spot intensity distribution. 139
6.5 Experimental setup illustrates the diagnostic layout [6]. 139
6.6 Proton energy data captured with cable and connector induced reflections. Ripples can be observed resulting from the non-flat frequency response of the system with some contribution from the EMP. 141
6.7 Comparison on loss of temporal details and efficiency on removing broadband interference with no spectral features for rolling average filter and FIR low-pass filter with different chosen parameter. The FIR filter maintains more high frequency information and higher signal fidelity while removing more ripples. . 142
6.8 (left) X-ray flash can be seen on temporal domain data. (right) It's ripple is exaggerated when converted to the proton energy axis. 143
6.9 With filtering for EMP, the ripples due to cable and connectors can be seen affecting the proton data on all 3 different runs from the experiment. (left) P-polarisation (centre) circular polarisation (right) s-polarisation. 143
6.10 Spectral intensity normalised to x-ray flash amplitude. The striations from the x-ray can be identified. (left) P-polarisation (centre) circular polarisation (right) s-polarisation. 144
6.11 Comparison of background removal efficacy on temporal domain samples. Reflections from x-ray flash pulses were removed without introducing significant artifacts or resolution loss. (left) original temporal data (right) after the ripple removal process. 145
6.12 Comparison of background removal efficacy on proton spectra. (left) Original spectral data (right) data after the ripple removal process. 145
6.13 Comparison of P, S, and circular polarisation on proton spectra at best focus. . 146
6.14 Comparison of p, s, and circular polarisation on proton spectra with focus scan waterfall plot. 147
6.15 Maximum energy envelope for p, s, and circular polarisation. 147
6.16 Loss of stability and peak energy around best focus, p-polarisation. 148
6.17 Comparison on a_0, ponderomotive energy scaling times the normalised interaction area, and experimental data. 150

Chapter 1

Introduction

1.1 Laser driven plasma accelerators

Since the development of linear [1] and cyclotron [2] accelerators in the 1920s, the acceleration gradient has steadily improved, driven by innovations in material science, surface treatments, and the adoption of superconducting cavities, surpassing [3] the Kilpatrick limit [4]. But now, as accelerating gradients near the breakdown limits of advanced superconducting materials, the next generation of high-energy accelerator facilities will demand expansive land and substantial financial resources, both initially and throughout operation.

By contrast, laser-driven plasma accelerators exploit laser-induced relativistic interactions in plasma to sustain immense electric fields [5]. The seminal theory for accelerating particles with laser driven plasma accelerators can be found in 1979 PRL publication by T. Tajima et al. [6]. Electron acceleration with laser driver such as milestone work on monoenergetic beam production in 2004 [7] and betatron radiation production of spatially coherent synchrotron X-rays [8][9][10][11] have promising industrial applications.

Thick target generating energetic ions was demonstrated in 1986 [12], in 1999 with gas jet target [13], in 2000 with thin foil target [14] [15]. The importance of laser contrast yielding good ion acceleration performance was experimentally recognised with thin targets [16]. The theory of TNSA (Target normal sheath acceleration) [17] leading to the scaling from TNSA to RPA (Radiation pressure acceleration) was numerically demonstrated in 2006 [18]. Small size

targets demonstrating electron refluxing [19] and near critical density relativistic transparency acceleration region was explored [20]. Beam structure such as collimated output was demonstrated [21]. The transient accelerator structure generated temporarily by laser-plasma dynamics, can be rapidly be re-established with solid target replenishing system[22], supporting frequent operations. Unlike their conventional counterparts which retain their structures, laser-driven structures are transient, allowing for electric fields beyond typical material limits, heralding unparalleled acceleration gradients [23].

Such laser-driven systems promise compact, cost-efficient high-energy particle sources. Their affordability facilitates local accelerator access for diverse research groups, thus democratising high-energy beams for plasma and particle physics, obviating the need for expansive shared facilities [24].

1.2 Intense laser sources

Since the first appearance of lasers in the 1960s [25], high-power laser technology has increased rapidly in peak power capabilities [26], propelling applications like laser-driven plasma accelerators (LPAs). Chirped Pulse Amplification (CPA) has been pivotal in these advancements.

Adapting principles from radar-based radiowave amplifier and receiver designs [27], CPA amplifies ultrafast laser pulses to elevated energies, safeguarding amplifying materials and optics from damage. This technique, introduced by Gérard Mourou and Donna Strickland in the 1980s [28], who subsequently received the 2018 Nobel Prize in Physics, revolutionised laser amplification. By elongating the laser pulse's duration, it reduces the peak power experienced by amplifying optics. After amplification, the pulse undergoes recompression, reaching unprecedented peak powers. Details of CPA systems and their modern high repetition rate implementations will be discussed in later chapters.

The integration of CPA with parametric amplification [29][30]—a concept also rooted in radio frequency amplification [31]—has enabled the emergence of high-power lasers exceeding 10 petawatts, with even mightier 100 PW systems in the pipeline [32].

Beyond the sheer power metrics, the versatility and precision of these state-of-the-art laser

systems have started a new era of scientific exploration. The precision offered by CPA allows researchers to delve into ultrafast mechanics [33], spanning from attosecond physics to observing real-time electron dynamics in complex molecules.

1.3 Potential use of high repetition rate laser driven particle sources

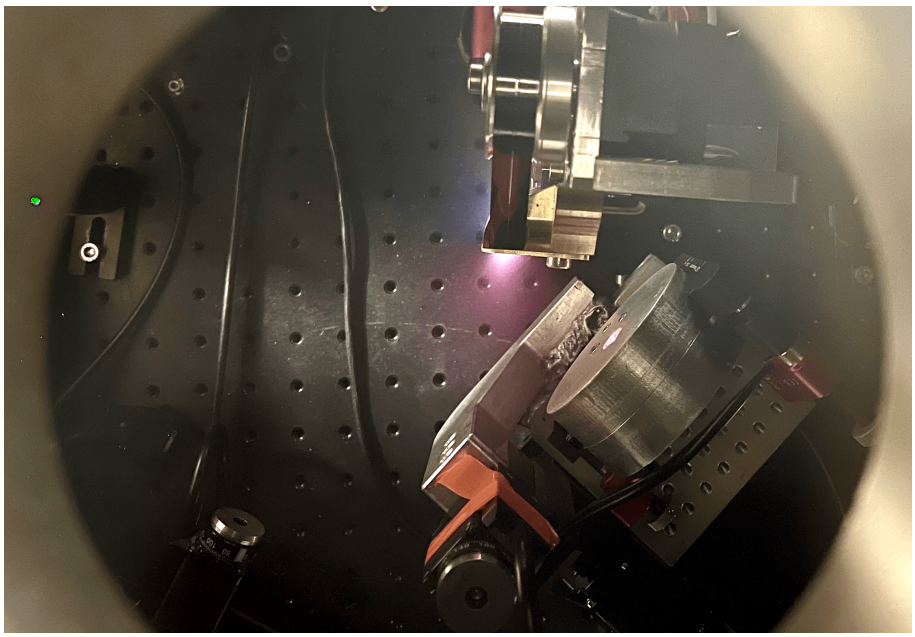


Figure 1.1: High repetition rate proton acceleration experiment using sub-1 µm stability solid target delivery system and sub - 1% (RMS) energy stability driver laser described in this thesis, operating at 100 Hz.

Compact laser-driven plasma accelerators offer high-energy radiation and intense electromagnetic fields generation with short pulse durations, presenting numerous potential applications in both industrial and medical settings.

1.3.1 Industrial and clinical imaging

Laser-driven high-energy particle sources also have broad industrial applications, potentially replacing traditional linear accelerators and cyclotrons, currently these are crucial in sectors like radiography, radioisotope production [34], and non-destructive testing [35][36][37].

Distinct from conventional accelerators, these laser-driven sources offer remarkable benefits such as reduced size, cost, and power consumption, along with robustness against external factors like vibration [35]. Furthermore, they have the potential to promise comparable energy outputs at a similar form factor. A commercial, container-sized laser system can yield GeV class electron beams, providing significantly more penetration compared to prevalent 9 MeV betatron portable accelerator sources [38].

Beyond industrial applications, they hold promise in medical imaging domains. Their compactness and superior spectral brilliance compared to conventional x-ray generators enable high-resolution imaging with decreased dose rates. Moreover, they introduce phase-contrast imaging, layering phase information atop absorption for a more detailed diagnosis [39], expanding the horizons of clinical imaging.

1.3.2 Hadron therapy

Laser-driven plasma accelerators are emerging as potential tools in medical hadron therapy [40], a treatment technique that uses high-energy particles like protons or carbon ions to target diseases, especially cancer.

Traditional hadron therapy employs sizable, high-cost accelerators, such as synchrotrons for microbeam radiation therapy [41] and cyclotrons for standard proton and ion therapies. These specialised accelerators usually reside in research facilities, treatment centres, or select hospitals, constraining patient accessibility to this advanced treatment.

By contrast, laser-driven plasma accelerators promise a compact, cost-efficient pathway to generate these high-energy particles. Their potential lies in decentralising hadron therapy—making it available not just in large treatment centres but in smaller healthcare establishments too. Such ubiquity could democratise access to advanced cancer treatments, especially in areas previously deemed financially nonviable for such investments [42].

Nevertheless, these laser-based systems are still in development phase. They face hurdles like enhancing beam quality, achieving lower energy variances, ensuring consistent shot-to-shot performance, and navigating stringent medical regulations. Despite these challenges, their potential is undeniable: laser-driven plasma accelerators might be the key to affordable and

widely accessible hadron therapy in the future.

1.4 Challenges in laser driven source properties

In the field of plasma-driven accelerators, current research is still dominated by efforts to refine beam quality, mitigate instabilities, and achieve better energy spread through better understanding of laser-plasma interactions. These challenges are accentuated by the dynamics between laser pulses and plasma, compounded by the non-existence of commercially viable high energy at high repetition rate laser systems necessary to meet the flux requirement for industrial and medical uses. Advancing towards commercial applicability demands research on laser drivers with higher repetition rates, improved plasma targetry, and optimised accelerator designs.

One primary challenge is ensuring high repetition rate targetry for these accelerators. The plasma accelerator often require delivery systems having high stability and durability against intense electromagnetic fields and particle bombardment. Higher repetition rates amplify stress and thermal effects, resulting in faster wear, performance drifts, and potentially premature breakdowns.

Additionally, the rapid succession of accelerator pulses in plasma-driven systems requires a target setup with fast replenishment capability. This involves advanced target construction, alignment, and placement methodologies resilient enough for harsh operational settings. For alignment and placement to be repeatable, a consistent target delivery system is indispensable.

Moreover, the interactions inherent to high repetition rate plasma-driven accelerators can generate secondary challenges, like debris production and target premature damage. These requires measures in the design phase to protect the accelerator's optical and target delivery components.

1.5 Thesis summary and author's contributions

This thesis demonstrated the formulation of a high repetition rate femtosecond laser source complemented by a low jitter solid targetry system and a proficient data capture infrastructure.

This innovation enhances parameter scanning capacities and paves the way for near future industrial and medical applications.

Chapter 2 provides a brief look into the theory and empirical studies related to high-intensity laser sources.

Chapter 3 delves into the foundational theories underpinning laser-propelled ion acceleration and its associated plasma concepts.

Chapter 4 consolidates advancements associated with a 100 Hz cryogenic laser system, emphasising elevating the technology readiness of a vibration-resistant cryogenic amplifier integrated with a 100 Hz compact laser source and a high-vacuum compressor. The author designed, manufactured, implemented, and characterised the regenerative amplifier and multi-pass amplifier apparatus.

Chapter 5 provides methods of high repetition rate target characterisation, as well as presents the design outcomes and evaluation of a high repetition rate target system, designed for precise and repeatable target positioning and fast target renewal, particularly for high numerical aperture laser drivers. Characterisation highlight a remarkably stable 100 Hz tape delivery system employed in recent proton acceleration studies. The author designed, manufactured, implemented, and characterised the high repetition rate target delivery apparatus.

Chapter 6 described experimental work undertaken with the laser and targetry systems previously discussed, also spotlighting the beginning of a high-throughput data acquisition architecture. The author performed experimental work in collaboration with other investigators, setup diagnostics, and gathered data, as well as performing the necessary data analysis.

Chapter 7 summarised the work and demonstrated future plans.

1.6 List of Publications

Work contributed by the author has yielded the following publications.

Xu, N., Streeter, M.J.V., Ettlinger, O.C., Ahmed, H., Astbury, S., Borghesi, M., Bourgeois, N., Curry, C.B., Dann, S.J.D., Dover, N.P. and Dzelzainis, T., 2023. Versatile tape-drive target for high-repetition-rate laser-driven proton acceleration. High Power Laser Science and Engineering, 11,

p.e23.

B Loughran, MJV Streeter, H Ahmed, S Astbury, M Balcazar, M Borghesi, N Bourgeois, CB Curry, SJD Dann, S DiIorio, NP Dover, T Dzelzainis, OC Ettlinger, M Gauthier, L Giuffrida, GD Glenn, SH Glenzer, JS Green, RJ Gray, GS Hicks, C Hyland, V Istokskaia, M King, D Margarone, O McCusker, P McKenna, Z Najmudin, C Parisuaña, P Parsons, C Spindloe, DR Symes, AGR Thomas, F Treffert, N Xu, CAJ Palmer, 2023. Automated control and optimization of laser-driven ion acceleration. High Power Laser Science and Engineering, 11, p.e35.

Stephen DiIorio, Matthew Streeter, Griffin Glenn, Franziska Treffert, Brendan Loughran, Hamad Ahmed, Sam Astbury, Mario Balcazar, Marco Borghesi, Nicolas Bourgeois, Chandra Breanne Curry, Stephen Dann, Nicholas Dover, Tom Dzelzainis, Oliver Ettlinger, Maxence Gauthier, Lorenzo Giuffrida, Siegfried Glenzer, James Green, Ross Gray, George Hicks, Cormac Hyland, Valeriia Istokskaia, Martin King, Daniele Margarone, Orla McCusker, Paul McKenna, Zulfikar Najmudin, Claudia Parisuana, Peter Parsons, Christopher Spindloe, Dan Symes, Alexander Thomas, Nuo Xu, Charlotte Palmer, 2023. Stable collimation of MeV proton beams by self-driven magnetic pinching. Bulletin of the American Physical Society.

Griffin Glenn, Hamad Ahmed, Sam Astbury, Mario Balcazar, Marco Borghesi, Nicholas Bourgeois, Christopher Crissman, Chandra Breanne Curry, Stephen Dann, Daniel Deponte, Stephen Dilorio, Nicholas Dover, Tom Dzelzainis, Oliver Ettlinger, Maxence Gauthier, Lorenzo Giuffrida, Siegfried Glenzer, Ross Gray, James Green, George Hicks, Cormac Hyland, Valeriia Istokskaia, Martin King, Brendan Loughran, Daniele Margarone, Orla McCusker, Paul McKenna, Zulfikar Najmudin, Charlotte Palmer, Claudia Parisuana, Peter Parsons, Christopher Spindloe, Matthew J Streeter, Dan Symes, Alec GR Thomas, Franziska Treffert, Nuo Xu, 2022. High repetition rate ion acceleration platform using ambient-temperature liquid jets. Bulletin of the American Physical Society.

Charlotte Palmer, Matthew J Streeter, Brendan Loughran, Hamad Ahmed, Sam Astbury, Marco Borghesi, Nicolas Bourgeois, Chandra Breanne Curry, Stephen Dann, Nicholas Dover, Tom Dzelzainis, Oliver Ettlinger, Maxence Gauthier, Lorenzo Giuffrida, Griffin Glenn, Siegfried Glenzer, Ross Gray, James Green, George Hicks, Cormac Hyland, Valeriia Istokskaia, Martin King, Daniele Margarone,

Orla McCusker, Paul McKenna, Zulfikar Najmudin, Claudia Parisuana, Peter Parsons, Chris Spindloe, Dan Symes, Alec GR Thomas, Franziska Treffert, Nuo Xu, 2021. Automated control and optimisation of high-intensity laser-solid interactions at up to 5 Hz. In APS Division of Plasma Physics Meeting Abstracts (Vol. 2021, pp. JM10-003).

Charlotte Palmer, Matthew J Streeter, Brendan Loughran, Hamad Ahmed, Sam Astbury, Marco Borghesi, Nicolas Bourgeois, Chandra Breanne Curry, Stephen Dann, Nicholas Dover, Tom Dzelzainis, Oliver Ettlinger, Maxence Gauthier, Lorenzo Giuffrida, Griffin Glenn, Siegfried Glenzer, Ross Gray, James Green, George Hicks, Cormac Hyland, Valeriia Istokskaia, Martin King, Daniele Margarone, Orla McCusker, Paul McKenna, Zulfikar Najmudin, Claudia Parisuana, Peter Parsons, Chris Spindloe, Dan Symes, Franziska Treffert, Nuo Xu, Alec GR Thomas, 2021. Optimisation of high-intensity laser-solid interactions using gaussian process regression. In APS Division of Plasma Physics Meeting Abstracts (Vol. 2021, pp. PP11-148).

References

[1] G Ising. Prinzip einer Methode zur Herstellung von Kanalstrahlen hoher Voltzahl. *Ark. Mat. Astron. Fys.*, 18(30):1–4, 1924.

[2] Ernest O. Lawrence and M. Stanley Livingston. The production of high speed protons without the use of high voltages. *Phys. Rev.*, 38:834–834, 1931.

[3] D Broemmelsiek, B Chase, D Edstrom, E Harms, J Leibfritz, S Nagaitsev, Y Pischalnikov, A Romanov, J Ruan, W Schappert, and et al. Record high-gradient srf beam acceleration at fermilab. *New Journal of Physics*, 20(11):113018, 2018.

[4] W. D. Kilpatrick. Criterion for Vacuum Sparking Designed to Include Both rf and dc. *Review of Scientific Instruments*, 28(10):824–826, 1957.

[5] J Badziak. Laser-driven ion acceleration: Methods, challenges and prospects. *Journal of Physics: Conference Series*, 959:012001, 2018.

[6] Toshiki Tajima and John M Dawson. Laser electron accelerator. *Physical review letters*, 43(4):267, 1979.

[7] Stuart PD Mangles, CD Murphy, Zulfikar Najmudin, Alexander George Roy Thomas, JL Collier, Aboobaker E Dangor, EJ Divall, PS Foster, JG Gallacher, CJ Hooker, et al. Monoenergetic beams of relativistic electrons from intense laser–plasma interactions. *Nature*, 431(7008):535–538, 2004.

[8] E Esarey, BA Shadwick, P Catravas, and WP Leemans. Synchrotron radiation from electron beams in plasma-focusing channels. *Physical Review E*, 65(5):056505, 2002.

[9] Antoine Rousse, Kim Ta Phuoc, Rahul Shah, Alexander Pukhov, Eric Lefebvre, Victor Malka, Sergey Kiselev, Fréderic Burgy, Jean-Philippe Rousseau, Donald Umstadter, et al. Production of a kev x-ray beam from synchrotron radiation in relativistic laser-plasma interaction. *Physical review letters*, 93(13):135005, 2004.

[10] Stefan Kneip, C McGuffey, Joana Luis Martins, SF Martins, C Bellei, V Chvykov, F Dollar, Ricardo Fonseca, C Huntington, G Kalintchenko, et al. Bright spatially coherent synchrotron x-rays from a table-top source. *Nature Physics*, 6(12):980–983, 2010.

[11] JC Wood, DJ Chapman, K Poder, NC Lopes, ME Rutherford, TG White, F Albert, KT Behm, N Booth, JSJ Bryant, et al. Ultrafast imaging of laser driven shock waves using betatron x-rays from a laser wakefield accelerator. *Scientific reports*, 8(1):1–10, 2018.

[12] SJ Gitomer, RD Jones, F Begay, AW Ehler, JF Kephart, and R Kristal. Fast ions and hot electrons in the laser–plasma interaction. *The Physics of fluids*, 29(8):2679–2688, 1986.

[13] K Krushelnick, EL Clark, Z Najmudin, Marco Salvati, MIK Santala, M Tatarakis, AE Dangor, Victor Malka, D Neely, R Allott, et al. Multi-mev ion production from high-intensity laser interactions with underdense plasmas. *Physical review letters*, 83(4):737, 1999.

[14] EL Clark, K Krushelnick, M Zepf, FN Beg, M Tatarakis, A Machacek, MIK Santala, I Watts, PA Norreys, and AE Dangor. Energetic heavy-ion and proton generation from ultraintense laser-plasma interactions with solids. *Physical Review Letters*, 85(8):1654, 2000.

[15] Anatoly Maksimchuk, Shaoting Gu, Kirk Flippo, Donald Umstadter, and V Yu Bychenkov. Forward ion acceleration in thin films driven by a high-intensity laser. *Physical Review Letters*, 84(18):4108, 2000.

[16] D Neely, P Foster, A Robinson, Filip Lindau, Olle Lundh, Anders Persson, C-G Wahlström, and P McKenna. Enhanced proton beams from ultrathin targets driven by high contrast laser pulses. *Applied Physics Letters*, 89(2), 2006.

[17] S. C. Wilks, a. B. Langdon, T. E. Cowan, M. Roth, M. Singh, S. Hatchett, M. H. Key, D. Pennington, A. J. Mackinnon, and R. A. Snavely. Energetic proton generation in ultra-intense laser–solid interactions. *Physics of Plasmas*, 8(2):542, 2001.

[18] T Esirkepov, M Yamagiwa, and T Tajima. Laser ion-acceleration scaling laws seen in multiparametric particle-in-cell simulations. *Physical review letters*, 96(10):105001, 2006.

[19] S Buffechoux, J Psikal, M Nakatsutsumi, L Romagnani, A Andreev, K Zeil, M Amin, P Antici, T Burris-Mog, A Compant-La-Fontaine, et al. Hot electrons transverse refluxing in ultraintense laser-solid interactions. *Physical review letters*, 105(1):015005, 2010.

[20] L Willingale, SR Nagel, AGR Thomas, C Bellei, RJ Clarke, AE Dangor, R Heathcote, MC Kaluza, C Kamperidis, S Kneip, et al. Characterization of high-intensity laser propagation in the relativistic transparent regime through measurements of energetic proton beams. *Physical review letters*, 102(12):125002, 2009.

[21] L Willingale, SPD Mangles, PM Nilson, RJ Clarke, AE Dangor, MC Kaluza, S Karsch, KL Lancaster, WB Mori, Z Najmudin, et al. Collimated multi-mev ion beams from high-intensity laser interactions with underdense plasma. *Physical review letters*, 96(24):245002, 2006.

[22] N Xu, MJV Streeter, OC Ettlinger, H Ahmed, S Astbury, M Borghesi, N Bourgeois, CB Curry, SJD Dann, NP Dover, et al. Versatile tape-drive target for high-repetition-rate laser-driven proton acceleration. *High Power Laser Science and Engineering*, 11:e23, 2023.

[23] A.C. Ting. Ultra-high gradient acceleration of electrons by laser wakefield plasma waves. *IEEE Conference Record - Abstracts. 1999 IEEE International Conference on Plasma Science. 26th IEEE International Conference (Cat. No.99CH36297).*

[24] Kazuhisa Nakajima, Min Chen, and Zhengming Sheng. Very compact linear colliders comprising seamless multistage laser-plasma accelerators. *Accelerators and Colliders*, 2020.

[25] T. H. Maiman. Stimulated optical radiation in ruby. *Nature*, 187(4736):493–494, 1960.

[26] Gerard Mourou. Ultrahigh peak power lasers present and future. *Applications of High Field and Short Wavelength Sources VII*, 1997.

[27] August W. Rihaczek. *Principles of high-resolution radar.* Artech House, 1969.

[28] Donna Strickland and Gerard Mourou. Compression of amplified chirped optical pulses. *Optics Communications*, 56(3):219–221, 1985.

[29] Ian N Ross, Pavel Matousek, Geoffrey HC New, and Karoly Osvay. Analysis and optimization of optical parametric chirped pulse amplification. *JOSA B*, 19(12):2945–2956, 2002.

[30] J. Bromage, S.-W. Bahk, I. A. Begishev, C. Dorrer, M. J. Guardalben, B. N. Hoffman, J. B. Oliver, R. G. Roides, E. M. Schiesser, M. J. Shoup III, and et al. Technology development for ultraintense all-opcpa systems. *High Power Laser Science and Engineering*, 7:e4, 2019.

[31] R. C. Knechtli and R. D. Weglein. Low-noise parametric amplifier. *Proceedings of the IRE*, 48(7):1218–1226, 1960.

[32] Colin Danson, Constantin Haefner, Jake Bromage, Thomas Butcher, Jean-Christophe Chanteloup, Enam Chowdhury, Almantas Galvanauskas, Leonida Gizzi, Joachim Hein, David Hillier, Nicholas Hopps, Yoshiaki Kato, Efim Khazanov, Ryosuke Kodama, Georg Korn, Ruxin Li, Yutong Li, Jens Limpert, Jingui Ma, and Jonathan Zuegel. Petawatt and exawatt class lasers worldwide. *High Power Laser Science and Engineering*, 7, 2019.

[33] Ferenc Krausz and Misha Ivanov. Attosecond physics. *Rev. Mod. Phys.*, 81:163–234, 2009.

[34] Martina Salvadori, Federica Baffigi, Damiano Del Sarto, Lorenzo Fulgentini, Petra Koester, Andrea Marasciulli, Fernando Brandi, Luca Umberto Labate, and Leonida Antonio Gizzi. Perspectives for application of sub 10-mev laser-driven proton beams: Pixe and medical radioisotopes production (conference presentation). *Laser Acceleration of Electrons, Protons, and Ions VII*, 2023.

[35] J. N. Gruse, M. J. V. Streeter, C. Thornton, C. D. Armstrong, C. D. Baird, N. Bourgeois, S. Cipiccia, O. J. Finlay, C. D. Gregory, Y. Katzir, N. C. Lopes, S. P. D. Mangles, Z. Najmudin, D. Neely, L. R. Pickard, K. D. Potter, P. P. Rajeev, D. R. Rusby, C. I. D. Underwood, J. M. Warnett, M. A. (Mark A.) Williams, J. C. Wood, C. D. Murphy, C. M. Brenner, and D. R. Symes. Application of compact laser-driven accelerator x-ray sources for industrial imaging. *Nuclear Instruments and Methods in Physics Research Section A : Accelerators, Spectrometers, Detectors and Associated Equipment*, 983, 2020.

[36] JM Cole, JC Wood, NC Lopes, K Poder, RL Abel, S Alatabi, JSJ Bryant, A Jin, S Kneip, K Mecseki, et al. Laser-wakefield accelerators as hard x-ray sources for 3d medical imaging of human bone. *Scientific reports*, 5(1):13244, 2015.

[37] Jason M Cole, Daniel R Symes, Nelson C Lopes, Jonathan C Wood, Kristjan Poder, Saleh Alatabi, Stanley W Botchway, Peta S Foster, Sarah Gratton, Sara Johnson, et al. High-resolution μct of a mouse embryo using a compact laser-driven x-ray betatron source. *Proceedings of the National Academy of Sciences*, 115(25):6335–6340, 2018.

[38] 9 Mev betatron system - jme ltd. `https://www.jme.co.uk/products-our-solutions/betatron-range/9mev-betatron-system/`.

[39] A. Döpp, L. Hehn, J. Götzfried, J. Wenz, M. Gilljohann, H. Ding, S. Schindler, F. Pfeiffer, and S. Karsch. Quick x-ray microtomography using a laser-driven betatron source. *Optica*, 5(2):199–203, 2018.

[40] S. V. Bulanov. Laser ion acceleration for hadron therapy. *2014 International Conference Laser Optics*, 2014.

[41] Elke Bräuer-Krisch, Jean-Francois Adam, Enver Alagoz, Stefan Bartzsch, Jeff Crosbie, Carlos DeWagter, Andrew Dipuglia, Mattia Donzelli, Simon Doran, Pauline Fournier, John Kalef-Ezra, Angela Kock, Michael Lerch, Ciara McErlean, Uwe Oelfke, Pawel Olko, Marco Petasecca, Marco Povoli, Anatoly Rosenfeld, Erik A. Siegbahn, Dan Sporea, and Bjarne Stugu. Medical physics aspects of the synchrotron radiation therapies: Microbeam radiation therapy (mrt) and synchrotron stereotactic radiotherapy (ssrt). *Physica Medica*, 31(6):568–583, 2015. Radiation Therapy with Synchrotron Radiation: Achievements and Challenges.

[42] Ken Ledingham, Paul Bolton, Naoya Shikazono, and C.-M. Ma. Towards laser driven hadron cancer radiotherapy:nbsp; a review of progress. *Applied Sciences*, 4(3):402–443, 2014.

Chapter 2

Intense laser sources, theory and review

This chapter provides a summary on the development of short pulse laser sources throughout history. The review aims to present an overview of the key advancements that have shaped the field of ultrafast laser technology.

2.1 Short pulse laser sources

The evolution of short pulse laser sources began with Theodore Maiman's introduction of the first ruby laser in 1960 [1]. Originally with low peak power and long pulse durations, shorter and more powerful pulses soon were generated.

Very quickly, the Q-switched laser emerged [2], starting an era of intense optical pulses condensed into shorter pulses. Techniques like passive Q-switching with saturable absorbers [3] and active Q-switching with Kerr-cell shutters [2] helped achieve pulse durations on the nanosecond scale, heightening peak power and broadening the laser's potential, especially in fields of nonlinear optics.

Between the mid and late 1960s, modelocking using ruby [4] and He-Ne lasers [5] resulted in short yet low-energy pulses. When combined with Q-switching, mode-locking was integrated into wide-gain bandwidth dye lasers [6], pushing the envelope further. The beginning of the Continuous Wave (CW) modelocked dye laser in 1972 started the development of mode-locking and broad-gain spectra [7].

Key subsequent developments include the 1982 innovation of pulse compression [8], the 1985

conception of chirped pulse amplification [9], the 1986 recognition of Ti:sapphire's potential as a broad bandwidth gain medium [10], and the Kerr-lens modelocking method in 1991 [11]. Together, these milestones have formed the landscape of today's high-intensity laser technology.

2.1.1 Q-switching

Q-switching is a method used in lasers to produce intense, short optical pulses, specifically used in this work in generating high-energy nanosecond pump pulses for Ti:sapphire laser amplifiers. It controls energy release from the laser medium to create these short, high-energy pulses.

The technique revolves around suppressing the standard continuous wave (CW) emission of a laser, enabling energy accumulation in the gain medium. A Q-switch introduces a high-loss component into the laser cavity, temporarily blocking the optical feedback essential for CW emission. This interruption allows energy to accumulate, resulting in a marked population inversion.

When a substantial population inversion forms, the Q-switch shifts to a low-loss mode, promptly releasing the accumulated energy as a high-energy pulse. This change allows the laser to extract stored energy into an intense, brief pulse.

Q-switching can be passive or active. Passive Q-switching uses saturable absorbers like dyes or crystals to achieve spontaneous Q-switching. However, this process lacks precise timing control and thus is not suitable for Ti:sapphire amplifier pump systems.

Active Q-switching uses external devices like Kerr cells, Pockel cells, or acousto-optic modulators (AOM) to manage cavity loss. Pockel cells, employing the polarisation shifts in certain materials under an electric field, are preferred for high energy pump lasers due to rapid response times and electronic trigger control over the Q-switching process. [12]

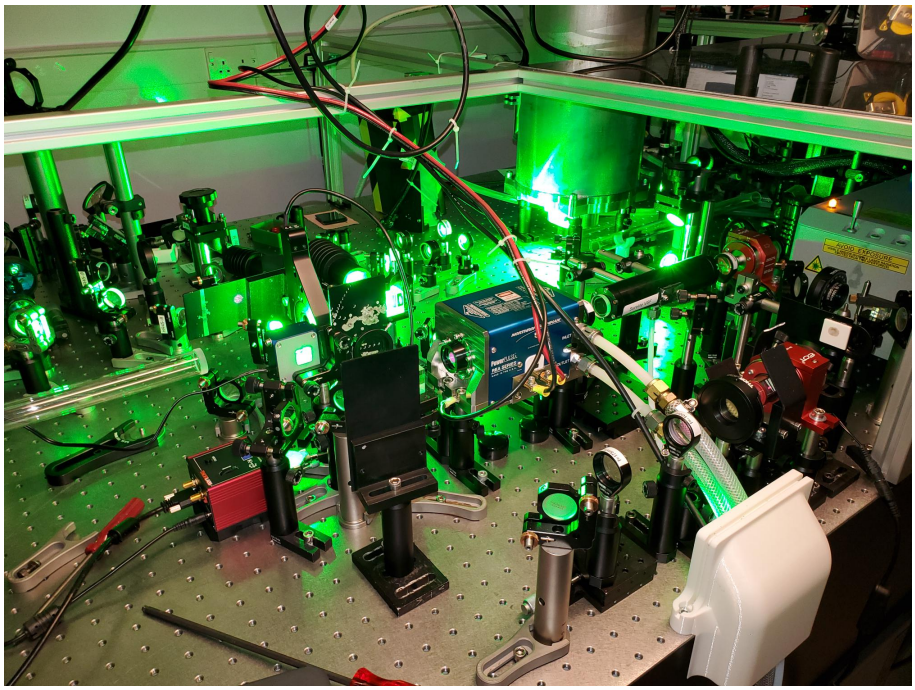


Figure 2.1: 0.7 Joule 100 Hz Q-switched pump laser and its amplifier, used to pump a Ti:sapphire amplifier, described in chapter 4

2.1.2 Mode locking

Mode locking is a technique in laser systems to produce ultrashort, high peak power optical pulses. It synchronises the phases of different longitudinal modes of slightly different frequency in the laser cavity, which are then coherently combined to generate a train of short pulses. These pulses are then used as seed pulses for further amplification in ultrafast laser systems.

Active mode locking uses external modulation, like electro-optic modulators, to control the laser field's phase and amplitude. Devices such as Kerr-cell shutters or acousto-optic modulators introduce time-varying modulation, achieving phase synchronisation among modes. This results in a consistent ultrashort pulse train. [13]

Passive mode locking involves a device like a saturable absorber or Kerr-lens cavity. This device increases cavity loss at low light intensities. As intracavity light intensity rises, the device changes its characteristics, favoring the emission of shorter pulses over longer ones. Typically, a Ti:sapphire laser system's seed laser uses a passively mode-locked Ti:sapphire oscillator synchronised with the laser system using phase-locked loop electronics.

2.1.3 Chirp pulse amplification

Without chirped pulse amplification (CPA), laser systems confront significant challenges in reaching high peak power, primarily due to the constraints imposed by peak power density on optics. Such constraints mean high-energy laser systems are often limited to longer, nanosecond pulse durations to avoid optical damage and saturation. This greatly limits their applicability in fields that demand both high energy and ultrashort pulses, like high field physics and plasma accelerators.

A particular technical issue that arises when attempting to scale up these non-CPA lasers is self-phase modulation. This non-linear effect can distort the pulse and reduce its coherence as the intensity increases. Self-phase modulation can introduce a frequency chirp, broaden the spectrum and the temporal length of the pulse, leading to challenges in maintaining pulse quality and fidelity.

Furthermore, amplifying these short pulses to higher energies without inducing damage to the system's components, especially mirrors and amplifier stages, becomes increasingly problematic. Direct amplification would require the use of very large optical components, which can be impractical and costly.

The CPA technique addresses these problems. It involves stretching the initial pulse temporally, thus reducing its peak power, then amplifying this stretched pulse, and finally compressing it to achieve a pulse with higher energy and short duration. This approach allows for substantial amplification without reaching the damage threshold of the system's components, effectively also solves the issues associated with self-phase modulation and other non-linear effects. [14]

2.1.4 Gain medium for wide-band operation

To achieve short pulse operation, wide bandwidth is needed. The time-bandwidth product (TBP) is an inherent characteristic of the spectrum utilisation efficiency when transmitting pulses. $TBP = \Delta t \times \Delta\omega$, where Δt is the pulse duration and $\Delta\omega$ is the bandwidth of the pulse.

Originating from the Fourier transform relationships, the product of the pulse duration and

its bandwidth is subject to constraints based on the uncertainty principle. Depending on the pulse shape, there is a minimum achievable product of its temporal width and spectral width.

For instance when TBP was originally introduced to describe a microwave pulse [15], a radar with flat top square wave pulse envelope profile width of τ, considered to be on/off modulated, will have a occupied bandwidth of $1/\tau$, resulting in TBP of 1. This is an inefficient way of utilising the electromagnetic spectrum. Later advancement in power electronics enabled different power envelope. Specifically, a Gaussian pulse which produce a minimum value of TBP (0.44) is characterised by its unique Gaussian shape in both time and frequency domains. It has maximum steepness in transition without overshoot and a minimised group delay. These characteristics render the Gaussian pulse especially advantageous in radar systems and lasers, maximising spectral efficiency to produce the shortest pulse.

A pulse is considered to be transform-limited when it reaches this minimum possible pulse length achievable with its bandwidth. Achieving a transform-limited pulse, as compressed as possible in time for its given spectral width, will produce the maximum peak power from a CPA system. Deviation from this condition usually suggests that the pulse is temporally stretched or that there are phase distortions across its spectrum.

Traditionally dye lasers have played a significant role in achieving wideband operation in laser systems. Dye lasers are a type of tunable laser that utilise organic dye molecules as the gain medium. These dyes exhibit broad emission bands

Dyes were selected and synthesised with broad absorption spectra, such that they could efficiently absorb pump light across a wide range of wavelengths, and with high fluorescence quantum yields and photostability, which ensured efficient energy transfer and long operational lifetimes. To achieve laser amplification, the dye molecules are dissolved in a suitable solvent, forming a dye solution or dye cell. However, dye lasers have limited satuation fluence and poor operability due to toxicity and replenishing system reliability. Therefore they are mostly obsolete.

The demand for laser components capable of emitting and amplifying light over a broad spectral range has led to the exploration and optimisation of various gain media. Titanium sapphire, also known as Ti:sapphire, has emerged as one of the most promising materials for

achieving wide-band operation in lasers.

Typically, transition metal dopant such as Cr^{3+} and Ti^{3+} provides significantly broader gain bandwidth, compared to rare earth dopant such as Nd^{3+} and Tm^{3+}.

Transition metals have outer electrons in the 3d orbitals, which have relatively lower shielding effects compared to the 4f orbitals of rare earth metals. The 4f electrons in rare earth metals are shielded by the inner electron shells, leading to a more localised and narrow electronic energy level structure. On the other hand, the 3d electrons in transition metals experience less shielding, which results in a broader electronic energy level structure. [16][17]

In laser systems, the broader electronic energy level structure of transition metal ions allows for a wider range of energy states that can participate in the laser transition process, providing a broader gain bandwidth. As a result, lasers based on transition metal ions can cover a wider range of frequencies and produce shorter pulses, making them suitable for applications that require a broad spectrum to achieve ultrashort pulses. On the other hand, lasers based on rare earth metals such as nanosecond Nd:YAG laser Nd^{3+} with 4f electrons tend to have very limited bandwidth but have long fluorescent lifetime. Utilising relatively low peak power laser diodes as pump laser, Nd:YAG gain medium can release more energy but more slowly, they are therefore useful for pumping Ti:sapphire amplifiers at high repetition rate. [18]

The success of titanium doped sapphire as a gain medium can be attributed to its unique properties. It is a solid-state crystal that exhibits a broad absorption and emission band [19] in the visible and near-infrared regions of the electromagnetic spectrum. This inherent spectral versatility allows for the generation of laser light with a wide range of wavelengths.

The development of titanium sapphire gain media for wide-band operation started with the synthesis and purification of high-quality crystals. Various growth techniques, such as the Czochralski method and heat exchanger method (HEM) [20] have been employed to obtain large, single crystals of titanium sapphire with high optical quality (FOM higher than 300). [21]

One key aspect to a economical laser system is the selection of the appropriate pump wavelength to match the absorption characteristics of the crystal. For Ti:sapphire, the peak of the absorption spectrum is around 500 nm, which is close to the wavelength of frequency doubled Nd:YAG. Hense, it is possible effectively pump these amplifiers with commonly used Nd:YAG

laser developed for industrial applications, therefore reducing system cost and complexity.

Additionally, the design of the laser cavity plays a crucial role in achieving wide-band operation. Careful consideration is given to factors such as cavity length and mirror reflectivity over the gain bandwidth to suppress gain narrowing.

2.1.5 High repetition rate sources

The rising demand for high repetition rate lasers results from evolving scientific and industrial needs. Laser systems delivering pulses at repetition rates ranging from 25 Hz to 1 kHz and beyond are desired for increased throughput and precision in areas such as fundamental research.

In industrial sectors, high repetition rate lasers expedite processes like laser micromachining and ablation, translating to quicker material processing. They enable a higher pulse throughput, thus enhancing efficiency and cost-effectiveness. Innovations like diode-pumped solid state YAG lasers and QCW laser diode arrays as pump sources have arisen from this need. [22]

In research, such lasers permit faster data collection and a superior signal-to-noise ratio from statistic. Techniques like transient absorption spectroscopy benefit immensely from these lasers, providing better precision and speed in investigating ultrafast processes. They also support high-speed parametric scans, allowing comprehensive data gathering over large sample regions promptly. [23]

However, designing these lasers presents challenges. Key among them are managing thermal effects and ensuring the laser's stability and beam quality. Addressing these requires engineering of elements such as gain media, pump sources, and cooling systems. [24]

2.2 Short pulse laser diagnostics

Short pulse laser diagnostics are essential to any ultrafast laser system. In scientific research and experiments involving lasers, knowledge of the pulse duration, intensity, and other pulse parameters is required. It ensures accurate and reproducible results, enabling researchers to achieve conclusions with robust statistic and make meaningful comparisons between different experiments with significant noise level. Characterising laser pulses also helps in understanding

how the laser interacts with materials and how these interactions influence the overall process or phenomenon being studied.

Laser systems often require specific pulse characteristics to achieve optimal performance. For example, in ultrafast laser applications, having a well-characterised short pulse is essential for achieving high peak powers and producing ultrashort pulses, which are crucial for phenomena such as nonlinear optical effects or generation of extremely short light pulses.

In industrial and medical environments where short-pulse lasers are utilised, it is vital to have a thorough knowledge of the laser's operational parameters. Regularly monitoring of long-term performance is essential to ensure consistent and accurate energy delivery. Proper oversight and maintenance prevent the risk of delivering incorrect doses, which could compromise the safety and efficacy of procedures.

Laser systems may experience fluctuations in pulse parameters due to various factors such as aging components or environmental changes. Regular pulse characterisation helps identify any changes in the laser's performance, enabling preventative maintenance and compensation of drift within the optics system.

Applications requiring specific pulse parameters involving complex interaction between plasma and drive laser demand laser pulses with specific parameters, such as precise pulse duration and chirp.

2.2.1 Wavefront sensing and adaptive optics

A wavefront refers to the locus of points having the same phase of oscillation in a wave. For waves propagating through space, such as light or sound waves, the wavefront represents the surface over which the wave has the same phase at any given moment.

For a plane wave, like a laser beam traveling long distances without much divergence, the wavefront is essentially flat or planar. However, for a wave emitting from a point source, the wavefront is spherical. Illustration of abberated and spherical wavefront can be seen on Figure 2.2.

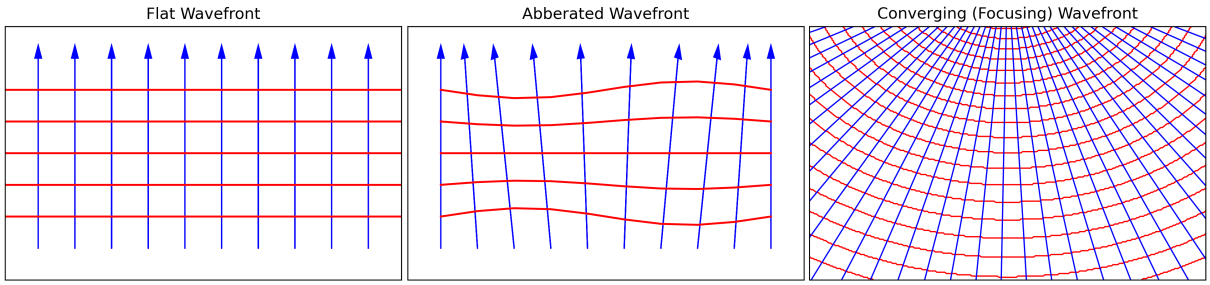


Figure 2.2: Illustration of wavefront

In optics, the quality of a wavefront is crucial. Deviations from a planar wavefront shape, often due to imperfections in the optical system, can result in aberrations which reduces focal spot enclosed energy, limiting the focused peak intensity.

Wavefront sensors can measure these deviations, and the data they produce can be used to correct the wavefront using adaptive optics. This is widely used in modern large telescopes, to correct for atmospheric turbulence and obtain clearer images of celestial objects, and laser systems, to correct for optical train imperfections. Wavefront sensing is a crucial aspect of high-repetition-rate lasers due to the rapid pulse rate at which they operate heating up optics therefore deforming them. [25]

High-repetition-rate lasers often have complex optical setups to mitigate thermal lensing effects, making it susceptible to slight misalignment, introducing wavefront aberrations. Wavefront sensing helps in focal spot quality. Figure 2.3 shows abberated wavefront and its affect on focal spot quality.

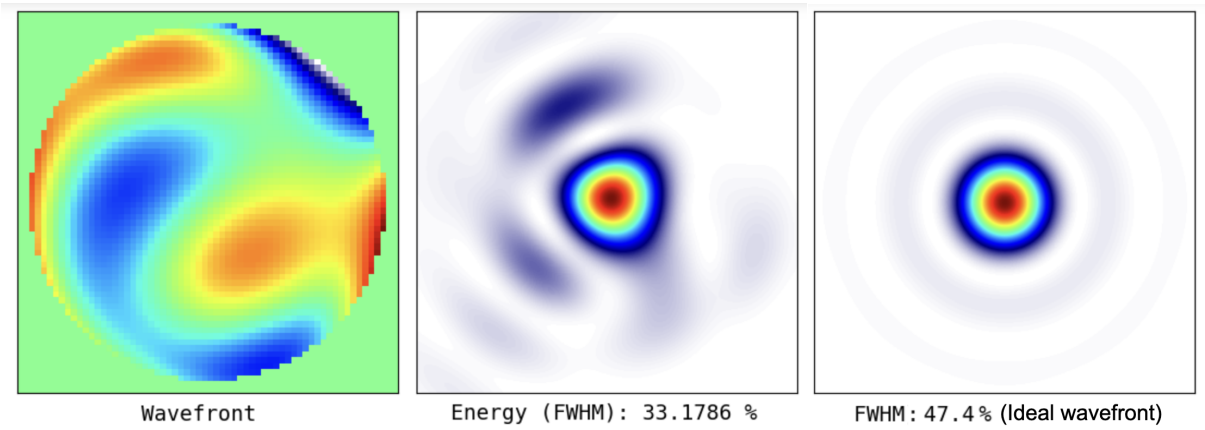


Figure 2.3: Abberated wavefront and focal spot

Within chirped pulse amplification (CPA) systems, diffraction gratings are employed to

compress ultrashort laser pulses. When a high repetition rate laser operates at a significant average power, the energy from each pulse can cause heating of these diffraction gratings. The heating effect on the grating can introduce thermal deformations. [26]

The outcome is a distorted wavefront from what should ideally be a plane wave or another well-defined wavefront shape. This wavefront aberration can degrade the focusability of the beam, increase the pulse duration, and introduce other unwanted spatial and temporal coupling effects. [27]

In most applications, understanding laser parameter is vital. Even advanced laser systems with real-time compensation can drift due to thermal and other mechanical drifts. Wavefront sensing not only provides on-shot focal spot data but can also be integrated with feedback systems for dynamic, real-time optical adjustments to maintain quality and compensate for various changes.

The Strehl ratio is a common metric used in optics to characterise the quality of an imaging system, especially with respect to aberrations. It gives a measure of how well an optical system focuses light compared to a perfect system. Specifically, the Strehl ratio provides a quantitative measure of the degradation in the peak of the point spread function (PSF) due to aberrations.

The Strehl ratio S is defined as:

$$S = \frac{\text{Peak intensity of the aberrated PSF}}{\text{Peak intensity of the perfect PSF}}$$

Where the perfect PSF refers to the PSF of an ideal optical system with no aberrations often represented by an Airy disk for circular apertures in the case of diffraction-limited systems, an example of a ideal focal spot is shown in figure 2.3.

In high-intensity applications, precise wavefront sensing helps avoid damage to optical elements, especially compressor gratings, and maintains a good focus spot. This ensures that the laser beam's focal point is stable and achieving a high Strehl ratio, leading to improved performance in laser-induced plasma experiments.

Overall, the technique of adaptive optics combined with wavefront sensing play a crucial role in high power lasers systems, especially one with high-repetition-rate. Adaptive optics (AO) is

a technique that can be used to correct for thermally induced optical aberrations and optimise the quality of the laser beam. The primary goal of adaptive optics is to improve the beam's spatial and temporal characteristics before compressor, and focal spot quality after compressor.

The adaptive optics system starts with wavefront sensing, where the wavefront distortions in the laser beam are measured using various techniques such as Shack-Hartmann sensors or interferometers. The wavefront data is then processed by a control system, which calculates the necessary corrections. [28] This type of wavefront sensor will be discussed later.

To apply the corrections, adaptive optics typically use deformable mirrors (DMs) [29] as active elements in the optical path. These devices have an array of controllable actuators that can deform their surfaces, allowing them to introduce controlled phase changes to compensate for wavefront distortions. [30]

The control system adjusts the deformable mirror or spatial light modulator in real-time based on the wavefront measurements. By continuously updating the corrective phase pattern, adaptive optics can rapidly and precisely compensate for any changing distortions in the laser beam from thermally induced wavefront changes.

The corrected laser beam exits the adaptive optics system before and / or after the compressor, with reduced aberrations and improved beam quality. This results in a pulse with better compression. The corrected beam after compressor produce focal spot with higher intensity and improved spatial enclosed energy.

2.2.2 Beam monitoring and compensation

In high-power laser systems, long-term drift is mainly caused by thermal effects and environmental factors. Thermal drift, specifically, refers to changes in the laser system's performance over time due to fluctuations in temperature. These temperature variations can occur within the laser components and from external environmental conditions. Such long-term drifts can have significant implications for the laser's pointing and energy stability, making them important considerations in high-power laser systems. [31]

One of the key contributors to thermal drift is the differential expansion and contraction of materials in the laser system. Different components of the laser setup, such as optical elements,

gain media, and mirrors, have varying coefficients of thermal expansion. As the temperature changes, these materials expand or contract at different rates, leading to mechanical stress and changes in the laser system's alignment. These shifts can cause misalignments and distortions in the laser beam's path, resulting in a degradation of the beam quality and a decrease in power output. [32]

Another thermal effect in high-power lasers is thermal lensing. In these systems, intense laser pulses interact with optical elements, and some of the laser energy is absorbed by these elements. The absorption of energy leads to localised heating and creates thermal gradients in the optical elements. These gradients induce refractive index variations, causing the formation of thermal lenses. The presence of thermal lenses alters the way the laser beam propagates, leading to changes in its focus and divergence. This effect can be especially problematic for maintaining precise beam characteristics over extended periods. Methods and realisation of effective thermal lensing compensation will be discussed in chapter 4.

External environmental factors can also contribute to thermal drift. Ambient temperature fluctuations, air conditioning, and even the heat generated by nearby equipment or lighting can influence the laser system's temperature, leading to long-term drift in the laser performance.

To mitigate the impact of thermal drift in high-power laser systems, various strategies are employed. These include using materials with low coefficients of thermal expansion, thermal management techniques such as active cooling.

Auto-alignment system can be used in a high-power laser setup to compensate for thermal drifts and other environmental variations that can cause misalignments or changes in the optical path. These systems employ advanced sensing and feedback mechanisms to detect deviations in the laser beam's alignment and make real-time adjustments to bring the laser back to its desired alignment.

The auto-alignment system typically includes various sensors and detectors that continuously monitor the laser beam's position, direction, and quality. These sensors can be based on various principles such as position-sensitive detectors, four-quadrant photodiodes, lateral effect sensors, interferometers, or wavefront sensors. The data collected from these sensors provide feedback on any misalignment in the laser beam caused by thermal drifts or other external factors.

Using this feedback data, the auto-alignment system processes the information through a control algorithm. The control algorithm calculates the necessary adjustments needed to bring the laser beam back to its desired position and alignment. It then sends appropriate commands to the active elements in the laser setup, such as motorised mounts or deformable mirrors, to make the required changes.

The active elements respond to the commands and adjust the optical components accordingly, effectively compensating for the thermal drift-induced misalignments or distortions. These adjustments are made in close to real-time, allowing the laser system to maintain its optimal alignment and beam quality even as environmental conditions change over time. This is specially important for high repetition rate laser systems, requiring a low latency feedback loop.

A Proportional-Integral-Derivative (PID) controller is one of the most commonly used feedback controllers in industry and engineering systems to maintain parameters such as laser pointing. The PID controller is designed to minimise the error between a setpoint and the process variable by adjusting the control inputs in a manner based on the proportional, integral, and derivative terms of that error.

$$u(t) = K_p \cdot e(t) + K_i \int_0^t e(\tau)d\tau + K_d \frac{de(t)}{dt}, \tag{2.1}$$

where $e(t)$ represents the error at time t, typically defined as $e(t) = \text{setpoint} - \text{process variable}$, K_p is the proportional gain, K_i is the integral gain, K_d is the derivative gain. This can be realised in modern micro-controllers and FPGAs, alone with actuators.

Experimental details of such high repetition rate laser system will be discussed in chapter 4.

References

[1] T. H. Maiman. Stimulated optical radiation in ruby. *Nature*, 187(4736):493–494, 1960.

[2] F. J. McClung and R. W. Hellwarth. Giant optical pulsations from ruby. *Appl. Opt.*, 1(S1):103–105, 1962.

[3] Georges Bret and Francois Gires. Giant-pulse laser and light amplifier using variable transmission coefficient glasses as light switches. *Applied Physics Letters*, 4(10):175–176, 1964.

[4] K. Gürs and R. Müller. Breitband-modulation durch steuerung der emission eines optischen masers (auskoppelmodulation). *Physics Letters*, 5(3):179–181, 1963.

[5] Hermann Statz and C. L. Tang. Phase locking of modes in lasers. *Journal of Applied Physics*, 36:3923–3927, 1965.

[6] W. Schmidt and F.P. Schäfer. Self-mode-locking of dye-lasers with saturated absorbers. *Physics Letters A*, 26(11):558–559, 1968.

[7] E.P. Ippen, C.V. Shank, and A. Dienes. Passive mode locking of the cw dye laser. *Applied Physics Letters*, 21(8):348–350, 1972.

[8] D. Grischkowsky and A. C. Balant. Optical pulse compression based on enhanced frequency chirping. *Applied Physics Letters*, 41(1), 1982.

[9] Donna Strickland and Gerard Mourou. Compression of amplified chirped optical pulses. *Optics Communications*, 56(3):219–221, 1985.

[10] P. F. Moulton. Spectroscopic and laser characteristics of ti:al2o3. *J. Opt. Soc. Am. B*, 3(1):125–133, 1986.

[11] D. E. Spence, P. N. Kean, and W. Sibbett. 60-fsec pulse generation from a self-mode-locked ti:sapphire laser. *Opt. Lett.*, 16(1):42–44, 1991.

[12] R. Carman, J. Reintjes, and H. Furumoto. Time synchronization of a single-mode-locked nd:glass laser pulse with aq-switched ruby-laser pulse. *IEEE Journal of Quantum Electronics*, 6(11):751–752, 1970.

[13] P. F. Curley and A. I. Ferguson. Actively mode-locked ti:sapphire laser producing transform-limited pulses of 150-fs duration. *Opt. Lett.*, 16(13):1016–1018, 1991.

[14] Tae Moon Jeong and Jongmin Lee. Femtosecond petawatt laser. *Annalen der Physik*, 526(3-4):157–172, 2014.

[15] J. R. Klauder, A. C. Price, S. Darlington, and W. J. Albersheim. The theory and design of chirp radars. *Bell System Technical Journal*, 39(4):745–808, 1960.

[16] G. H. Dieke and H. M. Crosswhite. The spectra of the doubly and triply ionized rare earths. *Appl. Opt.*, 2(7):675–686, 1963.

[17] B. R. Judd. Optical absorption intensities of rare-earth ions. *Phys. Rev.*, 127:750–761, 1962.

[18] A. Sullivan, J. Bonlie, D. F. Price, and W. E. White. 1.1-j, 120-fs laser system based on nd:glass-pumped ti:sapphire. *Opt. Lett.*, 21(8):603–605, 1996.

[19] G.F. Albrecht, J.M. Eggleston, and J.J. Ewing. Measurements of Ti3+:Al2O3 as a lasing material. *Optics Communications*, 52(6):401–404, 1985.

[20] David B. Joyce and Frederick Schmid. Progress in the growth of large scale ti:sapphire crystals by the heat exchanger method (hem) for petawatt class lasers. *Journal of Crystal Growth*, 312(8):1138–1141, 2010. The 17th American Conference on Crystal Growth and Epitaxy/The 14th US Biennial Workshop on Organometallic Vapor Phase Epitaxy/The 6th International Workshop on Modeling in Crystal Growth.

[21] J.F. Pinto, L. Esterowitz, G.H. Rosenblatt, M. Kokta, and D. Peressini. Improved ti:sapphire laser performance with new high figure of merit crystals. *IEEE Journal of Quantum Electronics*, 30(11):2612–2616, 1994.

[22] Robert Van Leeuwen, Yihan Xiong, Laurence S. Watkins, Jean-Francois Seurin, Guoyang Xu, Qing Wang, and Chuni Ghosh. High power 808 nm VCSEL arrays for pumping of compact pulsed high energy Nd:YAG lasers operating at 946 nm and 1064 nm for blue and UV light generation. In W. Andrew Clarkson, Norman Hodgson, and Ramesh Shori, editors, *Solid State Lasers XX: Technology and Devices*, volume 7912, page 79120Z. International Society for Optics and Photonics, SPIE, 2011.

[23] Charlotte Palmer. Paving the way for a revolution in high repetition rate laser-driven ion acceleration. *New Journal of Physics*, 20(6):061001, 2018.

[24] E. Sistrunk, T. Spinka, A. Bayramian, S. Betts, R. Bopp, S. Buck, K. Charron, J. Cupal, R. Deri, M. Drouin, A. Erlandson, E. S. Fulkerson, J. Horner, J. Horacek, J. Jarboe, K. Kasl, D. Kim, E. Koh, L. Koubikova, R. Lanning, W. Maranville, C. Marshall, D. Mason, J. Menapace, P. Miller, P. Mazurek, A. Naylon, J. Novak, D. Peceli, P. Rosso, K. Schaffers, D. Smith, J. Stanley, R. Steele, S. Telford, J. Thoma, D. VanBlarcom, J. Weiss, P. Wegner, B. Rus, and C. Haefner. All diode-pumped, high-repetition-rate advanced petawatt laser system (hapls). In *Conference on Lasers and Electro-Optics*, page STh1L.2. Optica Publishing Group, 2017.

[25] Justin D. Mansell, Joseph Hennawi, Eric K. Gustafson, Martin M. Fejer, Robert L. Byer, David Clubley, Sanichiro Yoshida, and David H. Reitze. Evaluating the effect of transmissive optic thermal lensing on laser beam quality with a shack–hartmann wave-front sensor. *Appl. Opt.*, 40(3):366–374, 2001.

[26] Patrick P. Lu, Amber L. Bullington, Peter Beyersdorf, Stefan Traeger, Justin Mansell, Ray Beausoleil, Eric K. Gustafson, Robert L. Byer, and Martin M. Fejer. Wavefront distortion of the reflected and diffracted beams produced by the thermoelastic deformation of a diffraction grating heated by a gaussian laser beam. *J. Opt. Soc. Am. A*, 24(3):659–668, 2007.

[27] Vincent Leroux, Timo Eichner, and Andreas R. Maier. Description of spatio-temporal couplings from heat-induced compressor grating deformation. *Opt. Express*, 28(6):8257–8265, 2020.

[28] Valentina Ye. Zavalova and Alexis V. Kudryashov. Shack-Hartmann wavefront sensor for laser beam analyses. In John D. Gonglewski, Mikhail A. Vorontsov, and Mark T. Gruneisen, editors, *High-Resolution Wavefront Control: Methods, Devices, and Applications III*, volume 4493, pages 277 – 284. International Society for Optics and Photonics, SPIE, 2002.

[29] Zhen Guo, Lianghong Yu, Jianye Wang, Cheng Wang, Yanqi Liu, Zebiao Gan, Wenqi Li, Yuxin Leng, Xiaoyan Liang, and Ruxin Li. Improvement of the focusing ability by double deformable mirrors for 10-pw-level ti: sapphire chirped pulse amplification laser system. *Opt. Express*, 26(20):26776–26786, 2018.

[30] Koshichi Nemoto, Takashi Fujii, Naohiko Goto, Takuya Nayuki, and Yoshi kazu Kanai. Transformation of a laser beam intensity profile by a deformable mirror. *Opt. Lett.*, 21(3):168–170, 1996.

[31] Steven C. Irick. Improved measurement accuracy in a long trace profiler: Compensation for laser pointing instability. *Nuclear Instruments and Methods in Physics Research Section A: Accelerators, Spectrometers, Detectors and Associated Equipment*, 347(1):226–230, 1994.

[32] Peter Giesen and Erik Folgering. Design guidelines for thermal stability in optomechanical instruments. 5176:126 – 134, 2003.

Chapter 3

Theory of laser-plasma ion accelerators

To comprehensively understand the ion and proton acceleration in laser-plasma interactions, it becomes important to thoroughly understand the physical processes at each stage of the interaction. This chapter initiates with a review of the necessary theory to appreciate the results of chapters 6.

From this, practical considerations essential for accelerator design are introduced, such as limiting factors on proton acceleration, proton energy scaling with laser and plasma parameters.

Proceeding further, the chapter investigates each of the key ion acceleration mechanisms, accompanied by a comprehensive review of recent experimental findings.

3.1 Plasma theory

3.1.1 Plasma frequency

When an electron is displaced from its neutral position, it encounters a restoring force generated by the breaking of quasi-neutrality, which pulls it back to its original position. However, momentum propels the electron further, causing it to oscillate around its initial point. The period of this oscillation is defined as the plasma frequency, ω_{pe}.

It can be expressed as [1]:

$$\omega_{pe} = \sqrt{\frac{n_e \cdot e^2}{m_e \cdot \varepsilon_0}},$$

where n_e is the electron density, e is the elementary charge, m_e represents the electron's mass, and ε_0 is the vacuum permittivity.

3.1.2 Dispersion relation

The dispersion relation [1]:

$$\omega^2 = \omega_p^2 + c^2 k^2,$$

where k is the wave number, ω represents the angular frequency of laser light, ω_p is the plasma frequency.

For a low intensity EM wave propagating through plasma [2]:

phase velocity is given by $v_p = \frac{c}{\sqrt{1-\frac{\omega_p^2}{\omega^2}}} \approx c\sqrt{1+\frac{\omega_p^2}{2\omega^2}}$

group velocity is given by $v_g = c\sqrt{1-\frac{\omega_p^2}{\omega^2}}$, assuming $\omega \gg \omega_p$, $v_g \approx c\left(1-\frac{\omega_p^2}{2\omega^2}\right)$

High intensity laser can modify the local refractive index of the plasma, from local plasma density and laser local laser intensity: $\eta = \frac{c}{v_p} = \sqrt{1-\frac{\omega_p^2}{\gamma\omega_0^2}}$. The non-linear refractive index, influenced by a high-intensity laser pulse, travels with the laser. This change results from the ponderomotive force affecting density and the electron mass variation caused by their relativistic quiver motion in the laser field. The transverse refractive index gradient causes wavefront tilting, resulting in the self-focusing effect.

The refractive index (η) of a medium is related to the wavenumber by [3]:

$$\eta = \frac{c}{v_{\text{phase}}},$$

where v_{phase} is the phase velocity of the wave.

3.1.3 Critical density

The critical density refers to the electron number density at which the plasma frequency is equal to the frequency of an incident electromagnetic wave. In other words, it is the threshold density at which the plasma becomes dense enough that their current can fully shield the EM wave that drives them. The critical density is originated from plasma waves, and from the dispersion

relation, when group velocity described previously goes to 0, em wave cannot propagate any further.

When the plasma frequency (ω_{pe}) becomes lower than the wave frequency (ω) due to a high electron number density, the wavenumber k becomes imaginary, and it is given by $k = i\frac{\omega_{pe}}{c}$ when $\omega_{pe} \gg \omega_L$. The propagation of waves in plasmas is affected by the plasma frequency ω_p. The damping length scale for these waves is $\frac{c}{\omega_p}$.

Critical density is important in ion acceleration primarily because above this density, the group velocity of the laser pulse approaches zero. This slowdown means that the ions are exposed to the accelerating fields of the laser for a significantly longer time, thereby receiving a more substantial energy boost. The prolonged interaction enhances the efficiency of ion acceleration.

For a typical Ti:sapphrie laser with a wavelength of 0.8 µm, the critical density is $1.73 \times 10^{27}\,\mathrm{m}^{-3}$, and for a Nd:glass laser such as Vulcan Petawatt operating at 1.05 µm, the critical density will be $1.0 \times 10^{27}\,\mathrm{m}^{-3}$.

3.1.4 Debye length

In plasmas, particles are free to move, allowing them to redistribute in response to external fields. This behavior leads to the phenomenon of screening, where electric fields are counteracted by the motion and arrangement of charged particles.

The Debye length (λ_D) is a parameter that describes the scale over which electric fields are effectively screened due to the presence of charged particles in a plasma.

In a plasma, electric fields created by charge imbalances can extend over relatively long distances. However, the electric field's impact is mitigated by the collective response of the charged particles.

The Debye length is defined as the distance at which the electrostatic potential drops to about $1/e$ (approximately 37%) of its value at a given point in the plasma. it can be expressed as [3]:

$$\lambda_D = \sqrt{\frac{\varepsilon_0 k_B T_e}{n_e e^2}}$$

Figure 3.1 shows the shielded and unshielded Coulomb potentials at condition commonly

found in the centre of laser-solid target interactions.

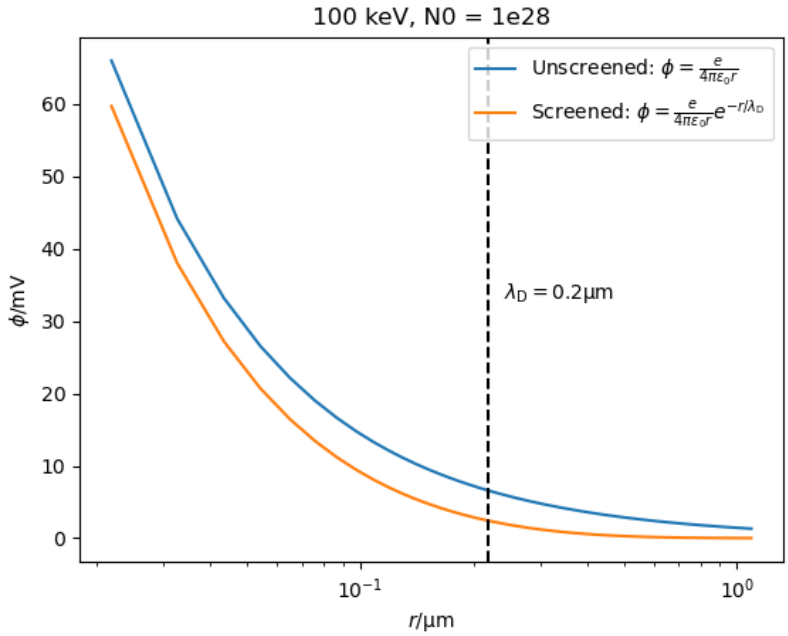


Figure 3.1: Example of the shielded and unshielded Coulomb potentials, both stemming from a point test charge $q_t = +e$.

3.2 Laser plasma interaction

3.2.1 Field ionisation and Collision ionisation

Field ionisation is a process where the strong electric field induces bound electrons in atoms or molecules to gain sufficient energy for liberation from their parent ions. This phenomenon occurs when the electric field intensity surpasses a critical threshold known as the ionisation threshold.

The Keldysh parameter (γ) quantifies the likelihood of field ionisation. This dimensionless parameter represents the ratio of the characteristic tunneling time to the period of the laser or electric field oscillation.

$$\gamma_K = \sqrt{\frac{e_i}{2U_p}},$$

where e_i represents the ionisation potential of the atom or molecule that is being subjected to

the intense laser field, and U_p is the ponderomotive potential. The ponderomotive potential is taken from the time-averaged motion of charged particles in the oscillating electric field of the laser. Ponderomotive potential will be discussed in the following section.

For a large Keldysh parameter ($\gamma \gg 1$), ionisation is predominantly governed by multi-photon absorption mechanisms, where multiple photons combine their energies to liberate an electron. Conversely, a small Keldysh parameter ($\gamma \ll 1$) indicates that tunneling ionisation becomes more dominant, wherein an electron overcomes the ionisation barrier through tunneling under the influence of the strong external field. In this regime, ionization occurs rapidly, on the order of femtoseconds.

In overdense plasma interactions, where the electron density is relatively high compared to the critical density, other ionisation mechanisms come into play. One such important process is collisional ionisation. In this mechanism, energetic electrons within the plasma collide with neutral atoms, transferring enough energy during the collision to liberate bound electrons from their parent atoms. These collisions can lead to the release of a substantial number of bound electrons, contributing to the plasma's ionisation level. Typically, collisional ionization becomes important when $T_e > e_i$.

3.2.2 Single electron motion in E-M field and normalised vector potential

The normalised vector potential, often denoted by $\vec{a}$ provides a convenient way to describe the strength of the laser field and how it influences the motion of charged particles, such as electrons.

For a simple plane wave with a Gaussian temporal profile, the normalised vector potential can be represented as: $a(z,t) = a_0 \exp\left(-\frac{t^2}{2\tau^2}\right) \cos(kz - \omega t + \phi)$. For the laser envelope, the slow time varying part is $a_0(t) = \exp\left(-\frac{t^2}{2\tau^2}\right)$.

In laser-plasma interactions or intense laser fields, the amplitude a_0 is related to the peak electric field strength of the laser. It quantifies how strong the laser field is and plays a crucial role in understanding the interaction of charged particles, particularly electrons, with the laser

field.

$$a_0 = \frac{eA_0}{mc} = \frac{eE_L}{mc\omega_0} = \sqrt{\frac{e^2\lambda^2 I_0}{2\pi^2 m_e^2 c^5 \varepsilon_0}} \approx 0.86\lambda_0[\mu m]\sqrt{I_0[10^{18} W/cm]}$$

For a commonly found femtosecond laser wavelength of 0.8 μm, with 30 fs pulse length and 100 mJ energy focused with $f/1.0$ optics onto a transform limited spot size of 1 μm, we can expect 1×10^{25} W/m^2, resulting in an a_0 of 24.5.

For linear polarisation along the x-axis, the electron traces out a figure-of-eight trajectory in the xz plane when observed from a frame moving at the electron's drift speed, $v_D/c = \frac{a_0^2}{4+a_0^2}$. On the other hand, for circular polarisation, the electron moves in the xy plane but appears stationary in the z plane in the moving frame. Conversely, for circular polarization, the electron moves in a helical trajectory in the xy plane. However, when observed from the same moving frame, the electron appears stationary along the z axis .

This motion is important when studying the interactions of circularly and linearly polarised light with an overdense plasma. The distinctions between their trajectories are significant and offer crucial insights into the behaviour of laser-plasma interactions and related phenomena.

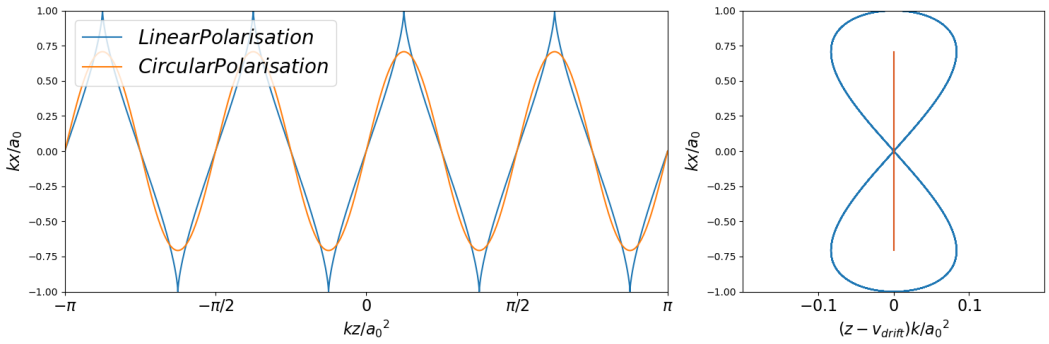


Figure 3.2: Single electron motion in static (left) and drift frame (right)

Particle motion significantly influences target heating, especially in the presence of intense lasers. In the Brunel vacuum heating context, electrons driven by a laser can cause plasma heating as they move into a target. With linear polarization, electrons can move both parallel and perpendicular to the target, potentially intensifying heating. However, with circular polarization, the helical, always-perpendicular motion of electrons reduces the depth of energy deposition, thus potentially mitigating plasma heating. Thus, choosing the right laser polarisation can

optimise target heating for specific applications [4]. Particles can gain up to the ponderomotive potential U_p from the laser field in energy.

3.2.3 Ponderomotive force

In laser-plasma interactions, the ponderomotive force is important as it acts as the dominant mechanism for transferring energy and momentum from the high-intensity laser to the plasma particles. This force pushes charged particles out of regions of high laser intensity, creating plasma density gradients and driving various phenomena like plasma cavitation, wakefield generation, and harmonic generation.

The ponderomotive force does not occur in a uniform intensity field; it exist in an intense electromagnetic field with spatial intensity and temporal variations, such as the intensity distribution of a laser's focal spot.

When a high-intensity laser is focused to a tight spot, the intensity of the electromagnetic field varies across the spatial region of the focal spot. In such a spatially non-uniform field, the ponderomotive force acts on charged particles, causing them to experience an average force due to the intensity variations.

The oscillating electrons tend to drift away from regions of maximum intensity, experiencing a diminished restoring force in the process. This results in a distinct shift in their trajectory and direction of motion. A notable consequence of this behavior is the migration of electrons away from the laser's focal spot. Under the ponderomotive force, these charged particles move towards areas of lower intensity. As a collective effect, this force modifies the local electron density and consequently alters the refractive index of the plasma.

The ponderomotive force F_p on the charged particle can be described as [5]

$$F_p = -\frac{e^2}{2m_e\omega^2}\nabla\langle E^2\rangle = -\frac{1}{2}m_e c^2 \nabla\langle a^2\rangle,$$

$\langle E^2\rangle$ represents the time-averaged square of the electric field magnitude. a is the normalised vector potential magnitude, and so $\langle a^2\rangle = a_0^2/2$.

It is important to account for relativistic effects in the analysis. When considering the

ponderomotive force in a relativistic context, by replacing the particle's rest mass, m_e, with the relativistic mass, γme, where γ is the Lorentz factor, the expression for the ponderomotive force takes on its relativistic form [5]:

$$F_p = -\frac{m_e c^2}{2\langle\gamma\rangle}\nabla\langle a^2\rangle$$

Ponderomotive energy is given by $U_p = 0.5\, a_0^2\, mc^2$, and its relativistic form: $U_{p,rel} = m_e c^2\left(\sqrt{1+a_0^2}-1\right)$.

Figure 3.3 shows the ponderomotive energy at different a_0. With realistic focal spot quality, a 250 mJ laser focused by a f/2.5 parabola can achieve a_0 of 4, this parameter was measured with CLF Astra laser in TA2 target chamber with a commercial grade off-axis parabolic mirror.

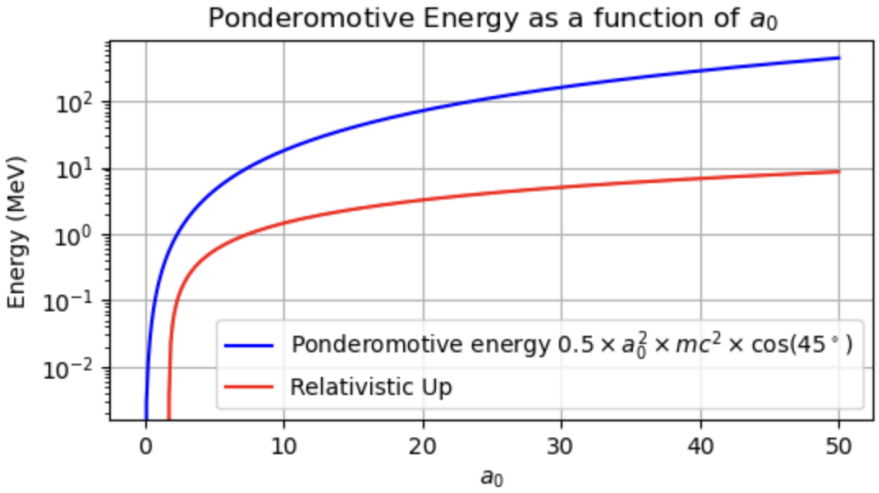


Figure 3.3: Ponderomotive energy, at different a_0 commonly achieved using focused Ti:sapphrie lasers.

3.2.4 Self-focusing

In underdense plasmas where EM waves from the drive laser can propagate through the plasma, the convergence or divergence of a laser pulse is subject to modification through a phenomenon known as self-focusing. This arises primarily from two influential factors: relativistic effects and the ponderomotive force. As a result of these effects, there is a corresponding change in the transverse refractive index of the medium. As a consequence, the phase velocity local to the laser's trajectory undergoes alterations. Such variations essentially impart a curvature to the

laser's wavefront. Depending on the nature of this curvature, the laser might experience either a focusing or a defocusing effect, significantly altering its propagation characteristics within the plasma.

Electrons within the central region of the laser pulse undergo a significant change in mass, particularly with an increased a_0. This results in variations in the plasma frequency across the laser spot. The refractive index of the plasma, denoted as η, can be expressed by [6]:

$$\eta = \sqrt{1 - \frac{\omega_p^2}{\gamma \omega_l^2}} = \sqrt{1 - \frac{n_e}{\gamma n_{\text{crit}}}},$$

where ω_p denotes the angular frequency of the plasma, ω_l symbolizes the angular frequency of the laser, and γ represents the Lorentz factor indicative of relativistic influences. As γ increases, η also rises. This relationship typically results in relativistic focusing at the center of a propagating laser pulse, where the intensity I and γ are at their peak.

3.3 Ion acceleration with intense laser

3.3.1 Acceleration schemes

At very high laser intensities, ions in the plasma can gain appreciable velocity due to the Lorentz force $\mathbf{F} = q\left(\mathbf{E} + \mathbf{v} \times \mathbf{B}\right)$. However it requires $10^{24}\,\mathrm{W/m^2}$ of intensity for ions to accelerate close to the speed of light.

For laser intensities below $10^{24}\,\mathrm{W/cm^2}$ [7], the Lorentz force acts upon both plasma electrons and ions. However, due to the significant mass difference between electrons and ions, the direct effect of the force on ions can often be neglected, leaving only the electrons to be influenced by it. Consequently, the force drives the electrons away from their equilibrium positions, creating an electric field between the moving electron cloud and the ions.

As a result of this field, the ions move in tandem with the electron cloud. The strength of this electric field enables the ions to attain high velocities within short distances and time intervals.

Various ion acceleration mechanisms have been extensively studied, each contributing to

the diverse range of possibilities. These mechanisms include sheath acceleration [8], light-sail [9] and hole-boring [10] radiation pressure acceleration (RPA) [11] and others which are less relevant for the energy range provided by near-future high repetition rate lasers [12][13].

3.3.2 Sheath acceleration

Sheath acceleration is an important and simple mechanism involved in ion acceleration during the interaction of intense lasers with a solid target. In sheath acceleration, the laser pulse is focused onto the front surface of the solid target, causing rapid heating and ionisation of the material. As the laser interacts with the target, a dense plasma forms near the surface due to ionisation. The electrons start the rapid expulsion from the target because of strong heating.

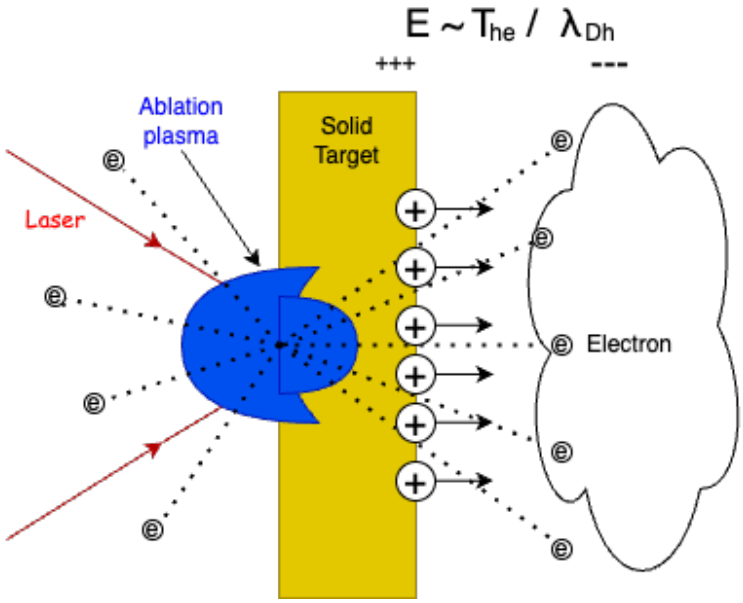


Figure 3.4: TNSA process

Illustrated in Figure 3.4, the plasma's expanding electrons create a strong electric field known as the sheath field in the region between the vacuum and the target surface. This electric field accelerates the newly created ions away from the target surface. The ions gain energy and are propelled into space as high-speed beams, resulting in ion acceleration.

A 1D isothermal model of the interaction was given by Mora [14]. In essence, the sheath transit time refers to the duration during which the sheath experiences the continuous influence of high-temperature electrons generated during the laser-plasma interaction. However, it is important

to note that this approach does not account for the subsequent transfer of energy between the hot electrons and the ions after the laser pulse ceases. Despite this limitation, truncating the acceleration process at approximately $t_{\text{acc}} \sim 1.3\tau_L$ and $E_{\max} = 2Zk_BT_e \ln\left(\tau + \sqrt{\tau^2+1}\right)^2$ has demonstrated favorable agreement in certain scenarios. To improve the explanation of the late-time evolution, a revised two-phase model has been introduced in 2005 [15].

Schreiber et al. [16] adopted a novel approach to formulate a model for sheath acceleration. They estimated that the high-temperature electrons generated at the front surface exhibit a radially confined surface charge on the rear surface with a radius $B = r_L + d\tan\theta$, where r_L represents the focal spot size, d is the target thickness, and θ is the half-angle of electron injection.

Under the assumptions mentioned, solving Poisson's equation in a cylindrically symmetric geometry along the axis of the centre of the radially confined surface charge allows us to estimate the maximum energy of the ion species when dealing with an infinitely long laser pulse. This maximum energy, denoted as $E_{i,\infty}$, is given by the expression:

$$E_{i,\infty} = \frac{q_i^2 mc^2}{\sqrt{\eta \frac{P_R}{P_L}}}$$

Here, $P_R = mc^3/r_e = 8.71\,\text{GW}$ is a constant, q_i represents the charge of the ion species, and r_e stands for the classical electron radius, The parameter η_L refers to the efficiency of laser absorption into hot electrons.

The maximum energy of the accelerated ions in sheath acceleration is proportional to the square root of the laser power and thus laser intensity. Therefore, if $\mathcal{E}$ represents the cut-off energy of the accelerated ions, $\mathcal{E} \propto I^{1/2}$ [17].

It is interesting to note that this expression contrasts with the Mora model, which suggests that as τ_L approaches infinity, the ion energy also approaches infinity. Here $E_{i,\infty}$ does not depend on the temperature of the hot electrons but is primarily influenced by the absorption fraction of laser energy into hot electrons.

The sheath acceleration process is highly sensitive to the laser intensity and target properties, and it generally produces ion beams with a broad energy spectrum.

3.3.3 Radiation pressure acceleration

The principle of Radiation Pressure Acceleration (RPA) revolves around propelling electrons utilising the photon's radiation pressure [18]. The theoretical underpinning of RPA was initially put forth by Esirkepov et al. [19]. The phenomenon manifests when the laser pulse's radiation pressure, driven by the photon's momentum, surpasses the thermal pressure from the plasma expansion.

The radiation pressure, P_R, can be expressed as:

$$P_R = (1 + R)\frac{I_l}{c}$$

R denotes the reflectivity of the target's surface. For $R = 0$, the target completely absorbs the incident radiation, whereas for $R = 1$, it fully reflects the radiation, and the radiation pressure is doubled. I_l represents the laser intensity. When the laser's intensity is around $I_l \approx 10^{24}\,\mathrm{W/m^{-2}}$, the corresponding pressure can reach values of $P_R \approx 30\,\mathrm{Gbar}$.

RPA has two primary forms: hole-boring and light-sail acceleration. These forms primarily differ based on laser density and the thickness of plasma they engage with.

Hole-boring RPA operates in contexts where the plasma can be perceived as infinitely thick during the acceleration phase. In such scenarios, the intense laser pulse pushes against the plasma front, repelling electrons and subsequently boring a hole into the dense plasma. As this happens, an electric field forms at the forefront of the plasma, accelerating ions. HB-RPA is most effective at densities only just above the critical density [20].

Conversely, light-sail acceleration, involves the acceleration of an entire thin plasma slab, much like a sail catching wind. When a sufficiently intense and short laser pulse interacts with a thin foil—ideally one with a thickness less than the laser wavelength—it propels the foil forward at speeds that can approach significant fractions of the speed of light. The cohesion between the foil's electrons and ions is relatively maintained during this acceleration, if the target stays cold. This is important in order to maintains the characteristics of the target and prevents the laser penetrating thought them.

Both hole-boring and light-sail mechanisms stand out due to their shared and appealing

characteristics. They exhibit favorable peak ion energy scaling with the laser intensity and have the potential to produce monoenergetic ion bunches. These attributes make both hole-boring and light-sail mechanisms highly valuable in the future applications of plasma driven proton sources. This can be aided by using circular polarisation and having normal incidence which inhibits strong target heating [21].

References

[1] D. Bohm and Eugene P. Gross. Theory of plasma oscillations. a. origin of medium-like behavior. *Physical Review*, 75:1851–1864, 1949.

[2] WB Mori. The physics of the nonlinear optics of plasmas at relativistic intensities for short-pulse lasers. *IEEE Journal of Quantum Electronics*, 33(11):1942–1953, 1997.

[3] Donald A. Gurnett and Amitava Bhattacharjee. *Introduction to Plasma Physics: With Space, Laboratory and Astrophysical Applications*. Cambridge University Press, 2 edition, 2017.

[4] L Chopineau, A Leblanc, G Blaclard, A Denoeud, M Thévenet, JL Vay, G Bonnaud, Ph Martin, H Vincenti, and F Quéré. Identification of coupling mechanisms between ultraintense laser light and dense plasmas. *Physical Review X*, 9(1):011050, 2019.

[5] R. Dragila. Heinrich Hora, Physics of Laser Driven Plasmas, Wiley-Interscience, 1981, New York xiv 317 pp. *Laser and Particle Beams*, 1(1), 1983.

[6] Heinrich Hora. Theory of relativistic self-focusing of laser radiation in plasmas. *J. Opt. Soc. Am.*, 65(8):882–886, 1975.

[7] J Badziak. Laser-driven ion acceleration: Methods, challenges and prospects. *Journal of Physics: Conference Series*, 959:012001, 2018.

[8] Nishiuchi Mamiko Pirozhkov Alexander Daido, Hiroyuki. Review of laser-driven ion sources and their applications. *Reports on progress in physics. Physical Society (Great Britain)*, 75:056401, 2012.

[9] B. Qiao, M. Zepf, M. Borghesi, B. Dromey, M. Geissler, A. Karmakar, and P. Gibbon. Radiation-pressure acceleration of ion beams from nanofoil targets: The leaky light-sail regime. *Physical Review Letters*, 105(15), 2010.

[10] A. P. L. Robinson. Production of high energy protons with hole-boring radiation pressure accelerationa). *Physics of Plasmas*, 18(5):056701, 2011.

[11] T. Esirkepov, M. Borghesi, S. V. Bulanov, G. Mourou, and T. Tajima. Highly efficient relativistic-ion generation in the laser-piston regime. *Phys. Rev. Lett.*, 92:175003, 2004.

[12] Nicholas P Dover, Tim Ziegler, Stefan Assenbaum, Constantin Bernert, Stefan Bock, Florian-Emanuel Brack, Thomas E Cowan, Emma J Ditter, Marco Garten, Lennart Gaus, et al. Enhanced ion acceleration from transparency-driven foils demonstrated at two ultraintense laser facilities. *Light: Science & Applications*, 12(1):71, 2023.

[13] Hiroyuki Daido, Mamiko Nishiuchi, and Alexander S Pirozhkov. Review of laser-driven ion sources and their applications. *Reports on Progress in Physics*, 75(5):056401, 2012.

[14] P. Mora. Plasma expansion into a vacuum. *Phys. Rev. Lett.*, 90:185002, 2003.

[15] P. Mora. Thin-foil expansion into a vacuum. *Phys. Rev. E*, 72:056401, 2005.

[16] J. Schreiber, F. Bell, F. Grüner, U. Schramm, M. Geissler, M. Schnürer, S. Ter-Avetisyan, B. M. Hegelich, J. Cobble, E. Brambrink, J. Fuchs, P. Audebert, and D. Habs. Analytical model for ion acceleration by high-intensity laser pulses. *Phys. Rev. Lett.*, 97:045005, 2006.

[17] J Fuchs, Y Sentoku, Stefan Karsch, J Cobble, P Audebert, Andreas Kemp, A Nikroo, P Antici, E Brambrink, A Blazevic, et al. Comparison of laser ion acceleration from the front and rear surfaces of thin foils. *Physical Review Letters*, 94(4):045004, 2005.

[18] Arthur Ashkin. Acceleration and trapping of particles by radiation pressure. *Physical Review Letters*, 24(4):156, 1970.

[19] T. Esirkepov, M. Borghesi, S. V. Bulanov, G. Mourou, and T. Tajima. Highly efficient relativistic-ion generation in the laser-piston regime. *Physical Review Letters*, 92(17), 2004.

[20] Charlotte AJ Palmer, NP Dover, I Pogorelsky, M Babzien, GI Dudnikova, M Ispiriyan, MN Polyanskiy, Jörg Schreiber, P Shkolnikov, V Yakimenko, et al. Monoenergetic proton beams accelerated by a radiation pressure driven shock. *Physical Review Letters*, 106(1):014801, 2011.

[21] APL Robinson, M Zepf, S Kar, RG Evans, and C Bellei. Radiation pressure acceleration of thin foils with circularly polarized laser pulses. *New Journal of Physics*, 10(1):013021, 2008.

Chapter 4

High repetition rate laser source development and characterisation

4.0.1 System overview

A high repetition rate laser source was developed and partially characterised, providing low energy jitter beam from regenerative amplifier output, and promising preliminary results from a scalable multipass amplifier. A detailed block diagram is shown in figure 4.1

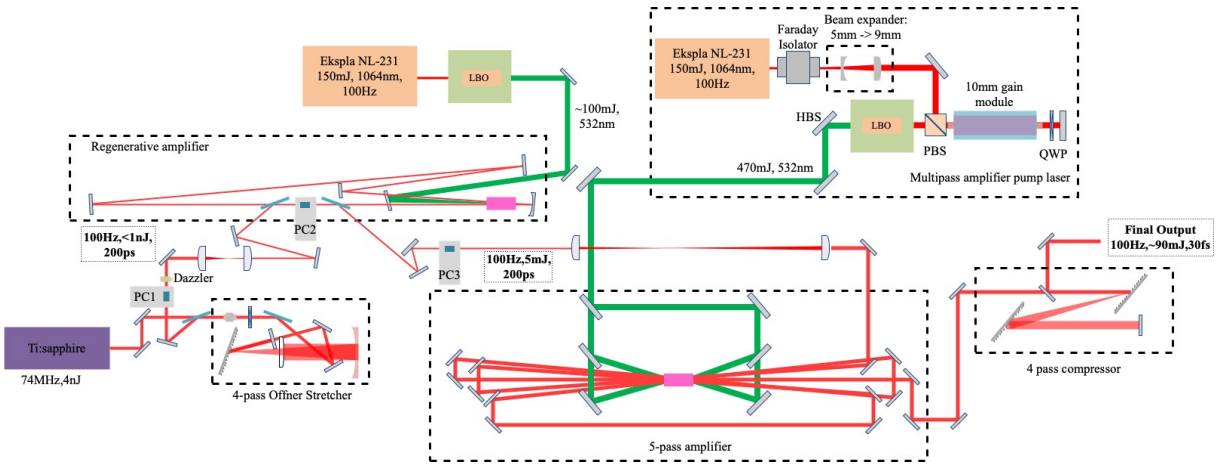


Figure 4.1: System diagram of high repetition rate laser.

A fully diode laser pumped amplifier chain was chosen to reach high repetition rate and average power whilst minimising system cost. Diode pumped pulsed laser development has benefit from recent industrial requirement for small hole drilling and micro manufacturing.

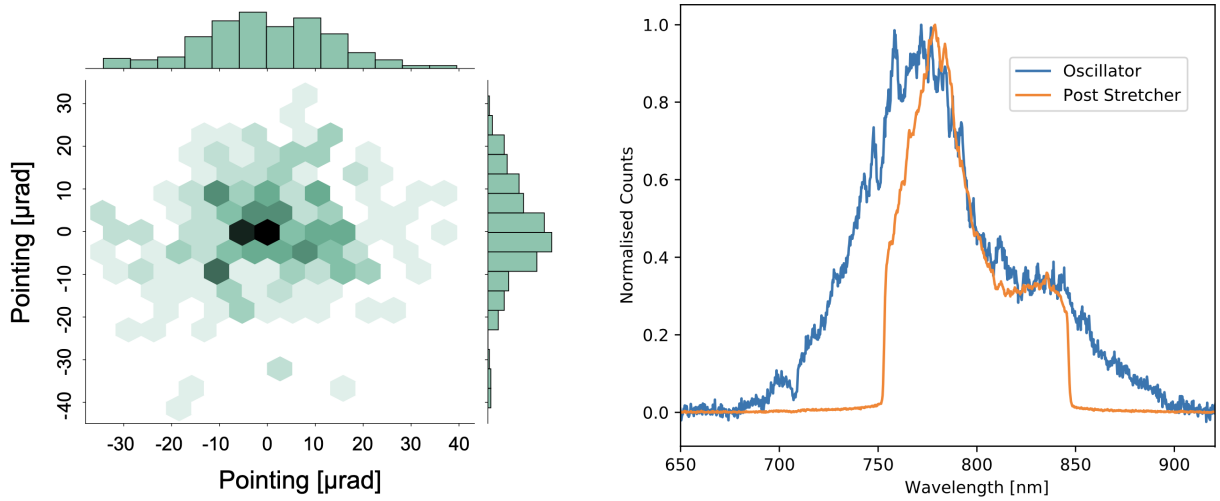
Diode pumped 100 Hz seed lasers operating at nanosecond pulse duration and 100 mJ energy level can be purchased off-the-shelf, along with side pumped gain modules, thus drastically reducing system cost and complexity, as well as footprint, compared to flashlamp based systems.

The laser system begins with a femtosource seed oscillator pumped by a 5W Axiom CW laser, which generates low-energy (4 nJ), short-duration pulses at a free running repetition rate (75 MHz) defined by the cavity length with some fluctuation as it is not regulated, Figure 4.2a shows its pointing stability.

The short oscillator pulses are then passed through an all reflective triplet telescope Offner stretcher with no transmission element which will induce chromatic aberration [1]. This design benefits from its symmetry. It only introduces symmetrical aberrations such as spherical and astigmatism, which can be easily corrected either by a custom aspherical correction mirror, or with adaptive optics. Owing to the geometry and limited telescope optic size, the stretcher only covers limited bandwidth (100 nm); there is a spectral clipping on blue and red end, as shown in Figure 4.2b. Since a full CPA system is chosen for its simplicity, rather than an OPCPA system, a 100 nm seeding bandwidth is adequately broad to not lose pulse width potential due to amplifier spectral narrowing.

An Acousto-Optic Programmable Dispersive Filter (AOPDF) can be used to adjust the spectral phase of the stretched pulses, enabling control over the pulse phase and amplitude. After the AOPDF, a pulse picking Pockel cell is used in conjunction with a phase-lock loop timing generator locked to the oscillator repetition rate, following slight fluctuation and predicting the accurate timing of future pulses. The stretched pulses are injected with another Pockel cell, and then amplified to higher energies in a cryogenic regenerative amplifier, which uses cryogenic cooling to improve its thermal performance and efficiency, followed by a pulse contrast enhancing Pockel cell, and further amplification in a cryogenic four-pass amplifier, as well as provision for another amplifier stage. After achieving the desired energy levels, the pulses are recompressed.

The aspects of the system that were implemented during by the author are presented in greater details in the following.



(a) Oscillator pointing stability

(b) Oscillator and stretcher output spectrum

Figure 4.2: Oscillator and stretcher performance.

4.1 Ti:sapphire regenerative amplifier

In the block diagram illustrated in Figure 4.3, a ring regenerative amplifier is employed for its superior contrast potentials. By integrating a Faraday isolator into the cavity, we ensure that the amplification predominantly occurs in the counter-clockwise direction, vastly suppressing the clockwise counterpart. This unique design aspect of the ring cavity, in contrast to the linear cavity, curtails the possibility of dual-directional gain. The result is a reduction in amplified spontaneous emission, leading to an enhanced system contrast. Additionally, the ring design facilitates a larger mode size on the crystal. This ensures that the damage threshold across various components of the amplifier cavity remains balanced, therefore producing more energy than similarly configured linear regenerative amplifier. Furthermore, this design promotes better isolation from the oscillator [2][3].

A 1064 nm commercial pump laser (EKSPLA NL230) generating 110 mJ of 532 nm pump energy with LBO crystal was transported through an adjustable telescope to fine tune the exact pumping diameter. A programmable half wave retarder combined with a polarising beam splitter cube provides necessary energy adjustment and warm-up ramping. These optics introduces some losses, resulting in an energy of 95 mJ onto the crystal face at full energy setting.

Fast turn-on and turn-off Pockel cells were used for cavity injection and ejection, as well

as pulse cleaning. These were combined with 10,000 to 1 high extinction ratio Brewster plate beam splitters.

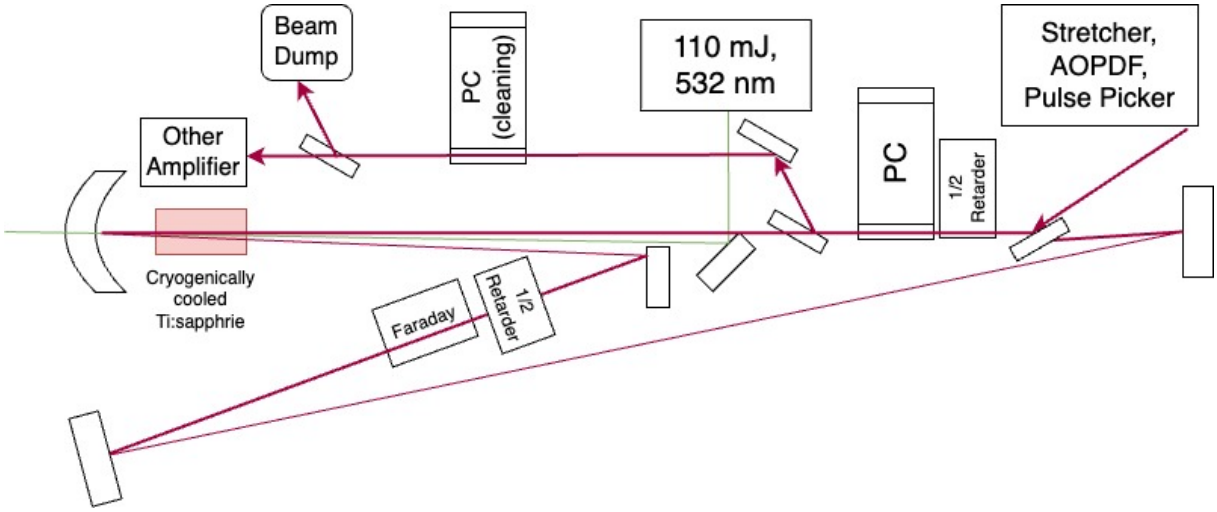


Figure 4.3: Block diagram, regenerative amplifier

4.1.1 Thermal lensing and cavity stability

We attempted to operate the regenerative amplifier at 100 Hz repetition rate with only water cooling and its thermal lensing compensated cavity design. However, due to poor thermal - extraction coupling and other engineering reasons such as sensitivity to structural drift and vibration, stability was worse than 6% RMS, and output energy was lower than 4 mJ. Whilst operating in this mode, the qualitative thermal image shown in Figure 4.4 was used to confirm the findings of finite element calculations that are presented below.

An example from a series of thermal images of the crystal surface, depicted in Figure 4.4, were captured in start-up and cool-down phase of the amplifier to diagnose the thermal transfer efficiency between the crystal, indium, and copper. Two sections of black electrical tape (typical emmisivity of 0.95), one large section on the outer water jacket and one smaller section added to the inner copper insert, were used to measure reflective copper surface temperature with low emissivity. The core that appears in the figure is the 12 millimeter diameter crystal, with the off-centred hot spot being due to the local temperature difference due to localised pumping with the pump laser. However, these measurements were not calibrated due to the unknown emissivity of coated Ti:sapphire crystal surface.

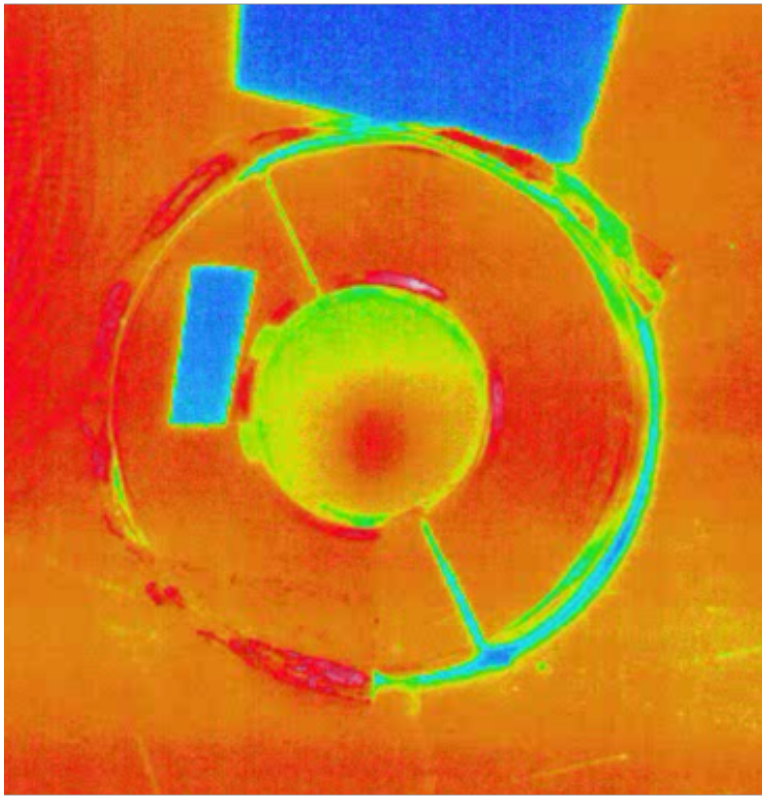


Figure 4.4: Thermal image of an water cooled Ti:sapphire crystal with pumping load, local heating can be observed where absorption of pump energy occurs

As shown in Figure 4.5, the original crystal water block was assembled with friction, while gap filling was provided by many layers of relatively hard aluminium oven foil, with no pressure applying mechanism. A newly designed water cooled crystal holder was manufactured with wire electrical discharge machining (EDM), providing better hole roundness and surface roughness. Combined with indium foil as interface, this provides significantly lower thermal resistance. An adjustable pressure applying mechanism was also implemented, with two guild pins and two known pitch screws.

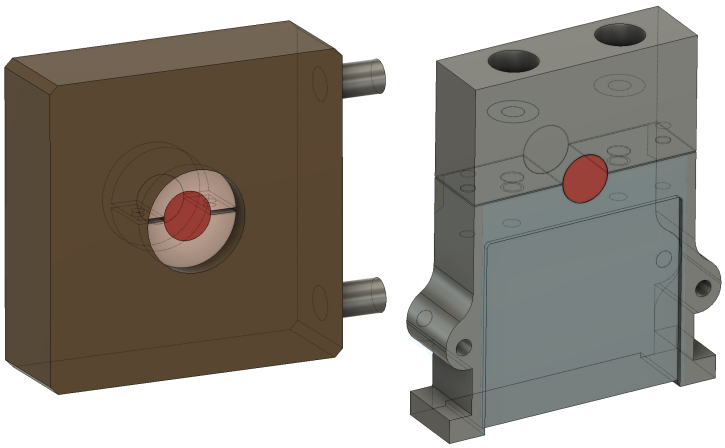
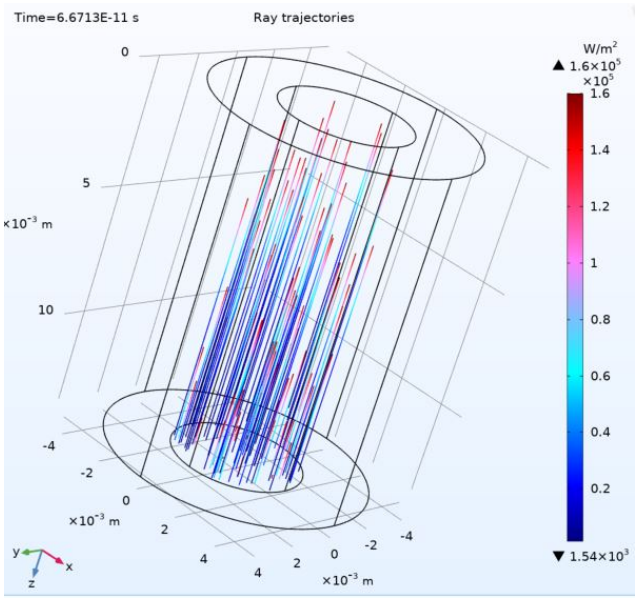


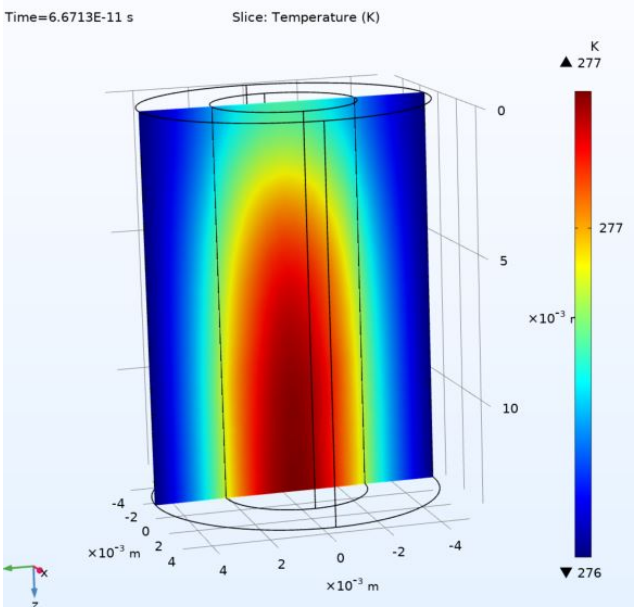
Figure 4.5: Comparison of Water-Cooled Crystal Mounts: On the left, a traditional design prevalent in low repetition rate amplifiers, featuring a loosely fitted crystal without controlled clamping force. On the right, an advanced design with optimised thermal performance, incorporating controlled clamping pressure and a refined low surface roughness contact area.

While the author has observed notable thermal performance improvements to the copper water block shown in Figure 4.5, the enhancements in optical performance were marginal. These limited gains can be attributed to the inherent thermal and optical extraction coupling happening within the cavity. Due to the inability to extract thermal energy from the crystal, temperature rises in the pumped region, accentuating the thermal lensing effect. This coupling between cavity performance and thermal lensing behaviour results in poor energy stability that cannot be optimised beyond 6%. These random fluctuations also occasionally push the thermal lensing beyond the cavity stability region, damaging optics.

COMSOL simulation with ray tracing and ray heating, are shown in Figure 4.6a and Figure 4.6b. The generated optical path lengh difference due to various thermal lensing effects are combined. Matlab was used to generate a best spherical fit, over only the optical aperture used by the cavity, shown in Figure 4.7a and Figure 4.7b. This shows agreement with measured thermal lensing focal length. Further experimentation with varying the cavity mirror focal length to compensate for the thermal lensing was attempted. However we decided to abandon the route of compensating thermal lensing due to reasons mentioned previously and also discussed later.

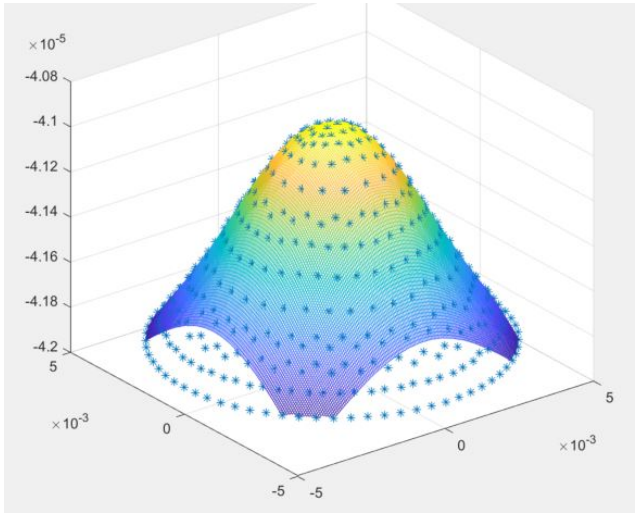


(a) Ray tracing and ray heating

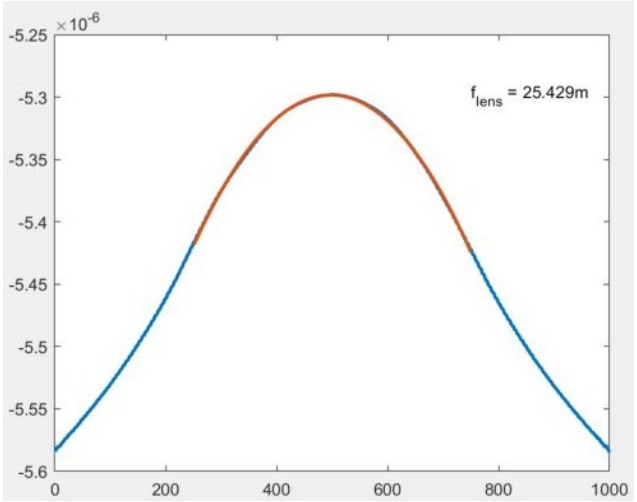


(b) Crystal internal temperature

Figure 4.6: COMSOL simulation with ray tracing and ray heating, pumping with 500 mJ laser at 100 Hz, 12 mm diameter crystal at 15 mm in length



(a) Optical path difference from simulated thermal lensing



(b) Spherical radius of curvature fit of focal length on region of optical aperture. The thermal lensing simulation agrees well with He-Ne beam measurement in various pumping power.

Figure 4.7: Thermal lensing radius calculation

For a simpler implementation and a safer start-up process, we later opted for a cryogenic amplifier, which will be elaborated upon in subsequent sections. An effectively compensated amplifier, operating at 100 Hz and utilising water cooling, can in principle be realised with a cavity design that accounts for the thermal lensing focal length and boasts a sturdy cavity structure with temperature regulation. However, during the laser's ramp-up phase, the cavity often operates outside its stability parameter zone. This can inadvertently focus the amplified beam onto the cavity optics. Such an occurrence was noted, leading to a decision, to pivot to a cryogenic design. This decision was further motivated by the cost involved in implementing the necessary infrastructure to support a sensitive room-temperature regenerative amplifier with the necessary optics safety systems.

4.1.2 Cryogenic regenerative amplifier

A few cryostat designs as well as the subsequent manufacturing was attempted by the author. Figure 4.8 shows the final revision. Due to the ring regenerative amplifier design, one cavity mirror needs to be as close to the crystal as possible [2][4][5], to maximise cavity mode size on the crystal and therefore maximise energy extraction. This poses difficulty for the cryostat window design and in achieving good pumping speed to compensate for outgassing of the window gluing epoxy, as well as adjacent contaminants.

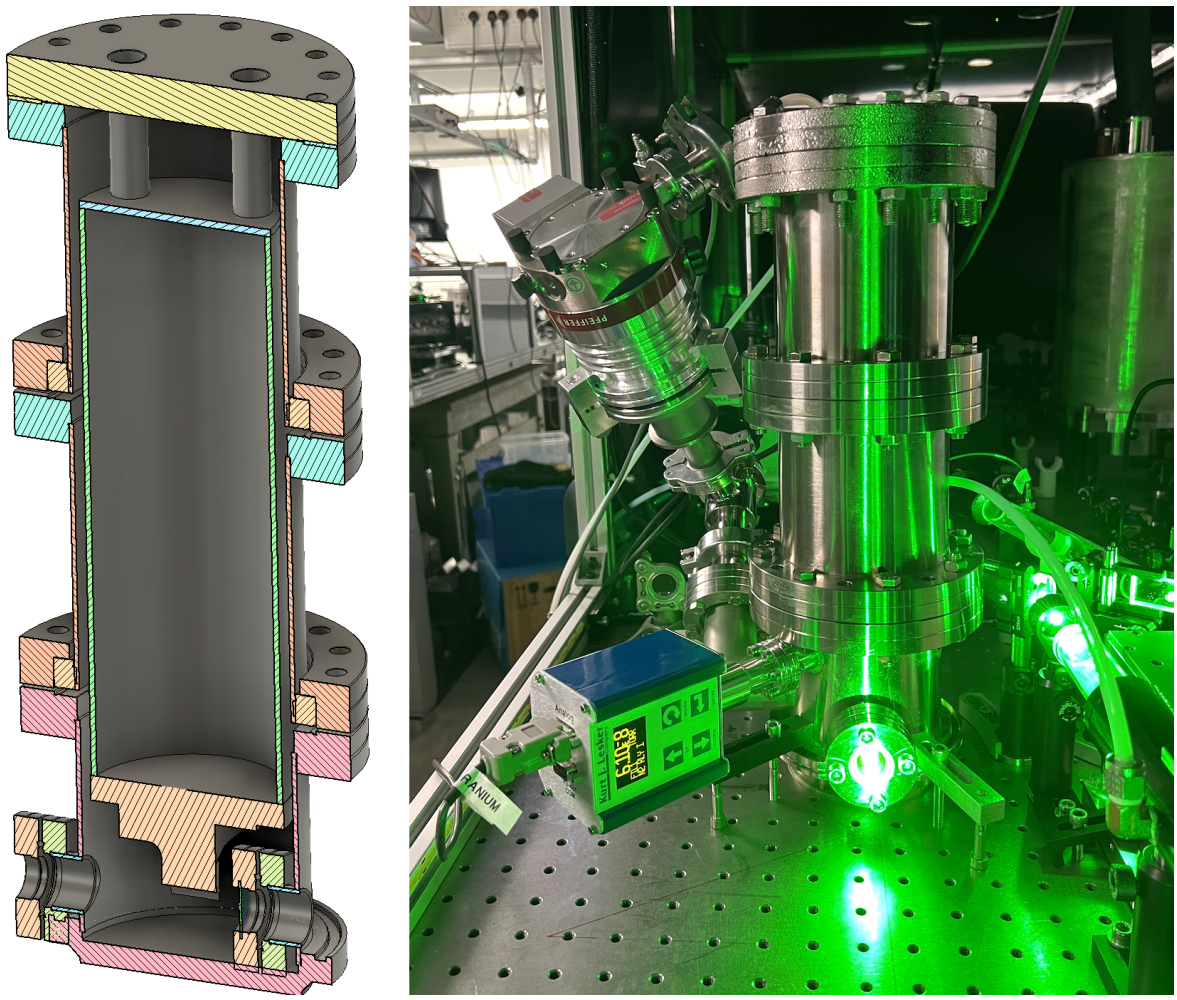


Figure 4.8: Regen cryogenic amplifier CAD design and operation.

Vacuum cleanliness is particularly important for cryogenic amplifier longevity. Comprehensive tests were conducted on various welding and cleaning methods to achieve a vacuum level of 1×10^{-9} millibar in the fully assembled state, without the need for final baking. This required deviations from standard vacuum practices. A manufacturing process utilising specialised

welding techniques that eliminated trapped volumes was employed. An extensive bake-out of major components were carried out under the monitoring of a residual gas analyser. Additionally, an argon purge chamber was used to install heat-sensitive components, such as glued windows and indium foil for heat transfer. These measures collectively ensured the longevity of the crystals and windows, especially under operating conditions that approached their damage thresholds.

Shown in Figure 4.9, a loss of output energy can be observed occurring gradually through 1 million shots. This was operating at a system vacuum level of 1×10^{-7} millibar. However, condensation of organic contaminants is still servere enough to cause bulk material damage in Ti:sapphire. The damaged crystal surface due to condensation followed by later damage shown in Figure 4.10, and its epi-illumination image with suspected carbon residual is shown in Figure 4.11

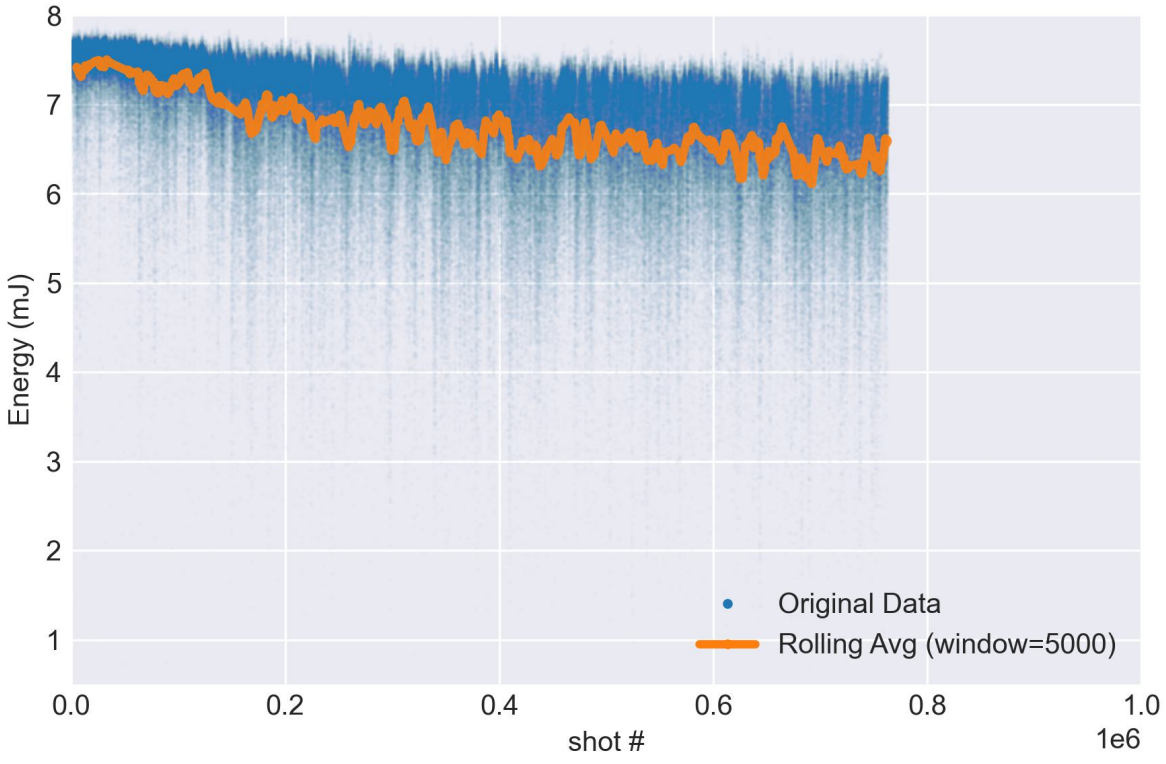


Figure 4.9: Example of poor vacuum level during cryogenic operation. Crystal coating gradually deteriorate after only about 1 million shots.

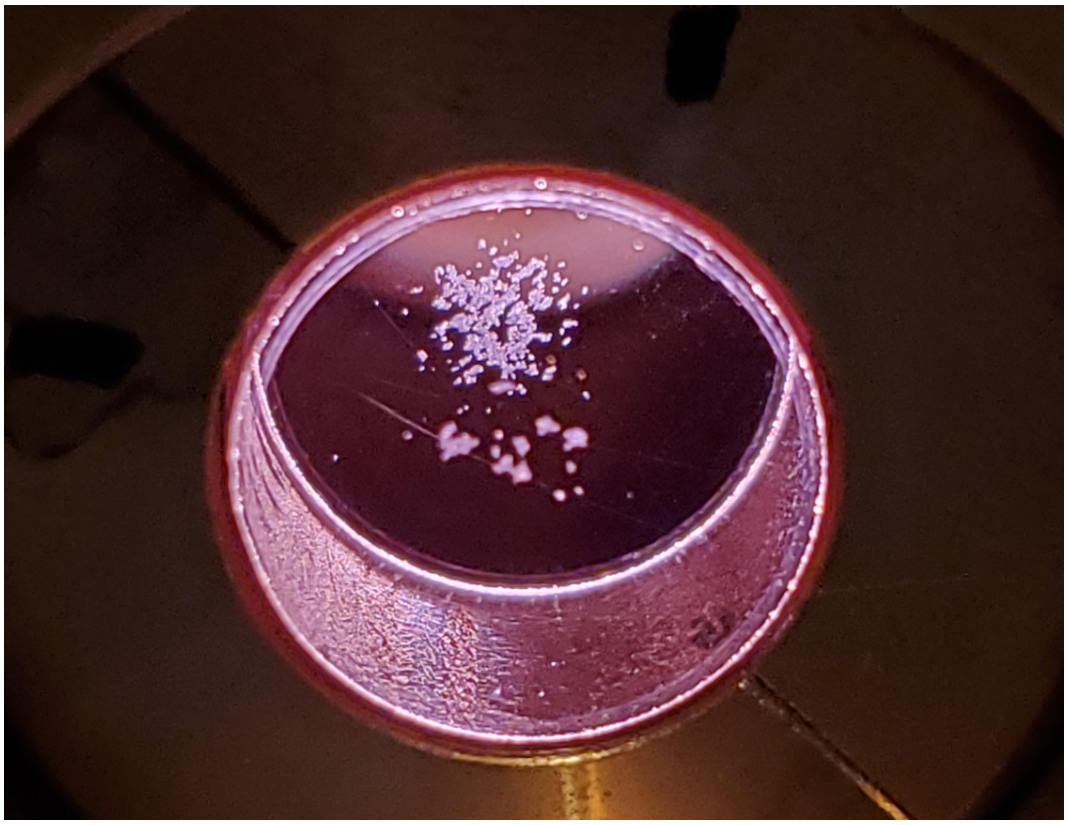


Figure 4.10: Bulk material and coating damage due to poor vacuum cleanliness and trapped volumes

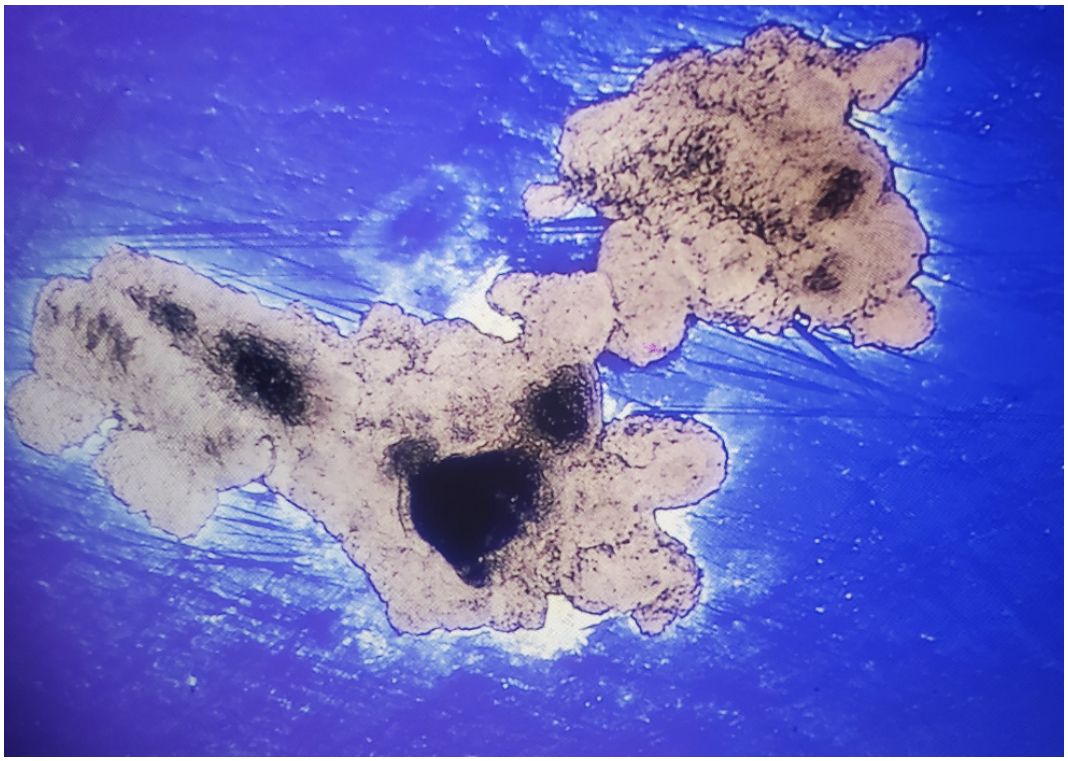


Figure 4.11: Optical damage crater under microscope, showing suspected carbon residual, scratches were due to post damage cleaning attempts

This amplifier achieved a relatively uniform output beam profile (Figure 4.12) with good stability (Figure 4.14) operating at cryogenic temperature. This was due to a combination of many effects in favour for cryogenic operation of Ti:sapphire. One effect which is the significant increase (40 times) in thermal conductivity [6][7]. The other effect working in conjunction is the reduction (7 times) in dn/dT (temperature dependent refractive index change) [8]. This results in 0.35% the thermal lensing effect at 77K compared to room temperature.

Even without thermal lensing concerns, cryogenic cooling of the Ti:Sapphire gain medium at 77K offers distinct advantages in energy extraction. At this temperature, the quantum efficiency reaches a value of 1, compared to 0.8 at room temperature, ensuring that all absorbed pump photons are utilised without non-radiative losses [9][10].

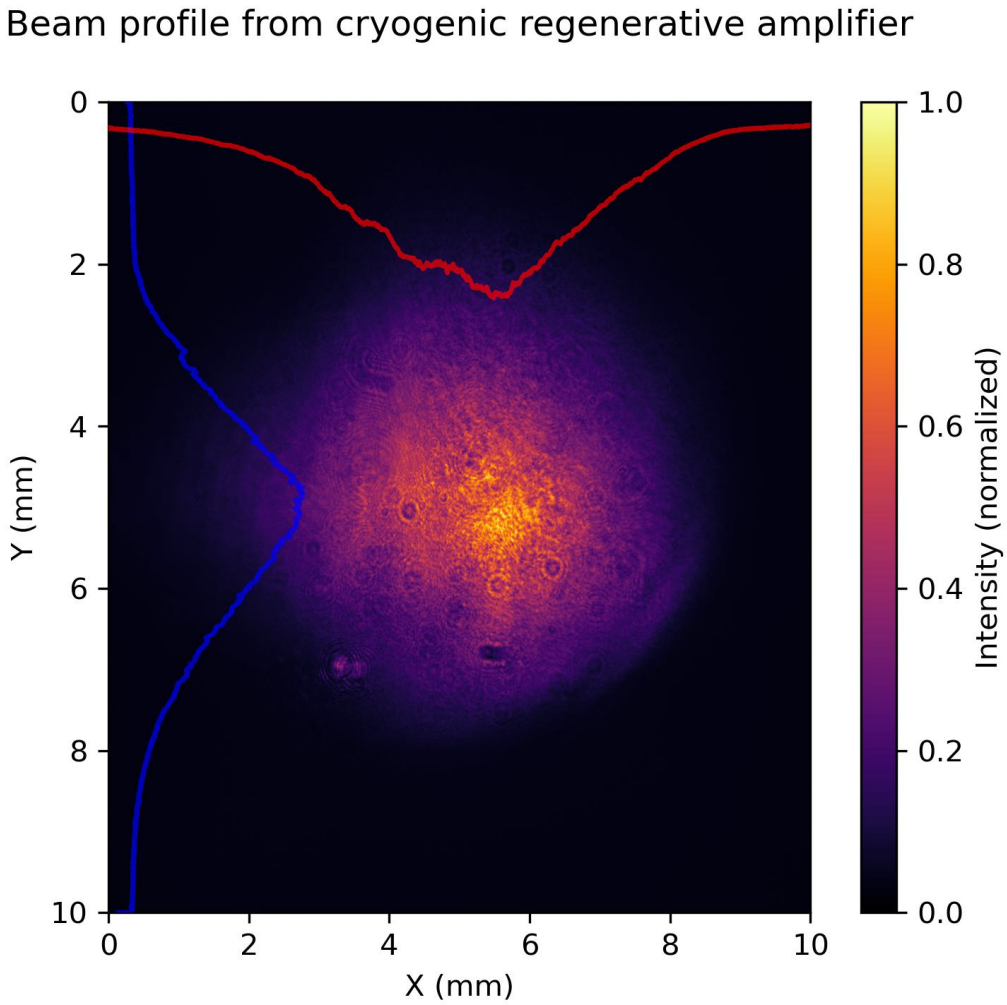


Figure 4.12: Output beam profile of cryogenically cooled regenerative amplifier. 12 mJ output pumped with 100 mJ 532nm laser at 100 Hz.

The output energy was monitored at the regenerative amplifier output using the statistical logging function of a calibrated pyroelectric energy meter with a diffusive attenuator. The data is shown in table 4.1. This shows a drastic performance increase from the previous 10 Hz system which operated at 3.8 mJ with 7.8% rms jitter.

Table 4.1: Statistical results from regenerative amplifier, comparison between cryogenic and water cooled amplifier with same pumping condition.

Parameter	**Value (Cryogenic)**	**Value (Water cooled)**
Average Value	12.26 mJ	3.45 mJ
Maximum Value	12.5 mJ	3.80 mJ
Minimum Value	10.7 mJ	1.82 mJ
RMS Stability	0.9114 %	7.805 %
PTP Stability	14.61 %	57.59 %
Repetition Rate	100.0 Hz	100.0 Hz
Average Power	1.23 W	0.34 W
Std Deviation	112 μJ	269 μJ

In Figure 4.13 and Figure 4.14, the long term energy stability example data of the described regenerative amplifier is shown. The regenerative amplifier is insusceptible to moderate vibration caused by nearby vacuum pumps, unlike previously with water cooling. This is due to the larger cavity stability margin. This was due to mainly the larger margin of stable mode sizes on different optical elements inside the cavity. This results in a more tightly focused cavity, which due to under filling of the pump laser to achieve optimum saturation, meaning that the cavity can accept relatively large amount of misalignment. This also helps to compensate for the daily drift of the optical table and floor. This was observed from the significantly longer interval required between realignment and optimisation, from almost everyday previously, to one month without intervention; only interrupted by an air conditioning unit failure.

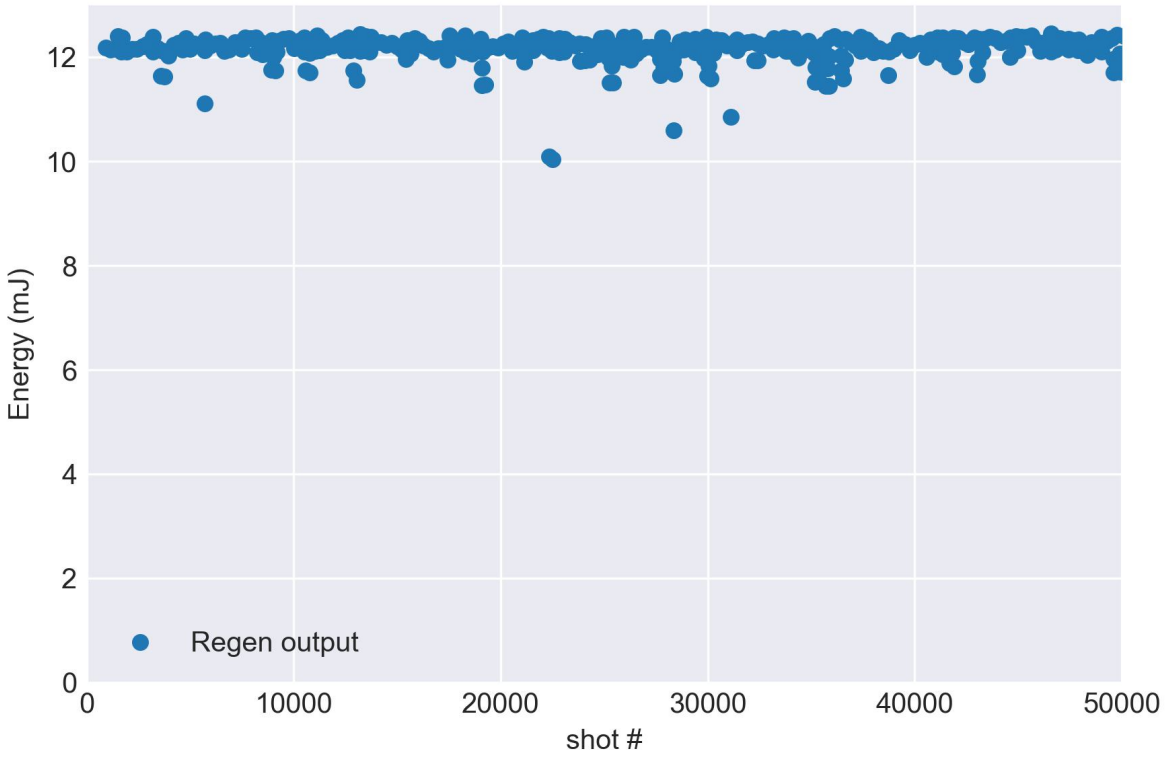


Figure 4.13: performance at 12mJ, 0.9% RMS stability under good vacuum conditions.

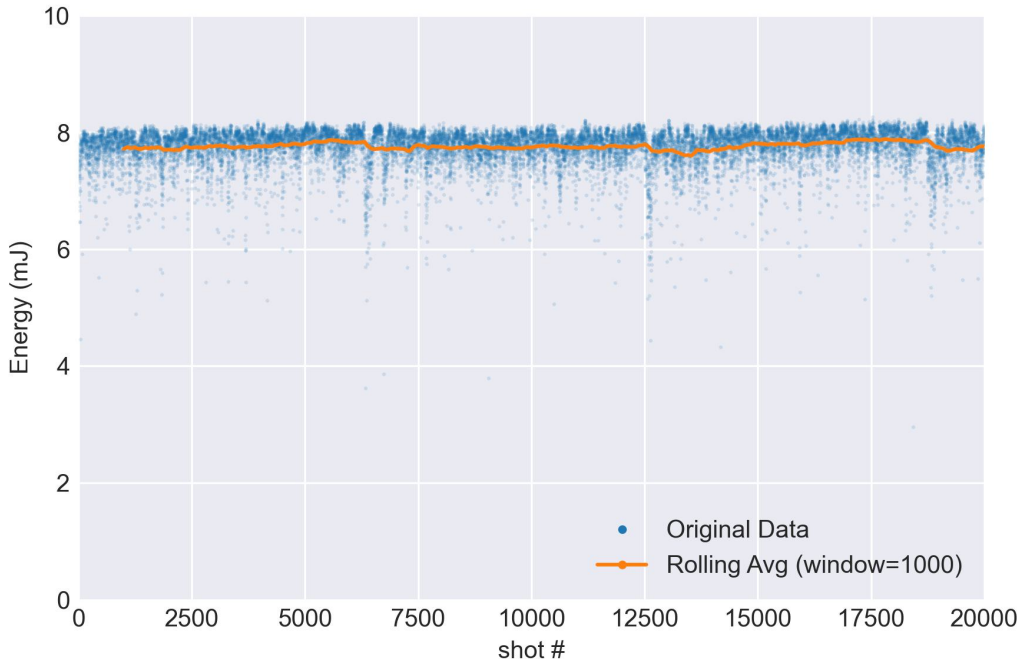


Figure 4.14: performance at 8mJ after cleaning Pockel cell. No visible drift is observed after many days of operation, 2 to 4 hour each day, and was only interrupted by lab air conditioning unit failure.

4.2 Diode pumped high repetition rate YAG laser

Diode-pumped lasers offer several advantages over traditional flashlamp-pumped lasers. They are more efficient, converting more electricity into optical energy, which results in cost and energy savings and a reduced thermal footprint. By contrast, flashlamp lasers produce more waste heat, affecting system stability and longevity due to increased thermal lensing, limiting also the repetition rate. Diode lasers also match the absorption peak of the YAG gain medium, ensuring effective absorption, while the broad spectrum of flashlamps can cause inefficiencies. Additionally, diode lasers are compact and robust, making them more reliable in various environments, whereas flashlamp systems are bulkier. Given these benefits, diode-pumped lasers are preferred for modern high-repetition-rate applications.

In Figure 4.15, the experimental setup for generating 100Hz nanoseconds pump beam is shown. Details will be discussed in the next few section.

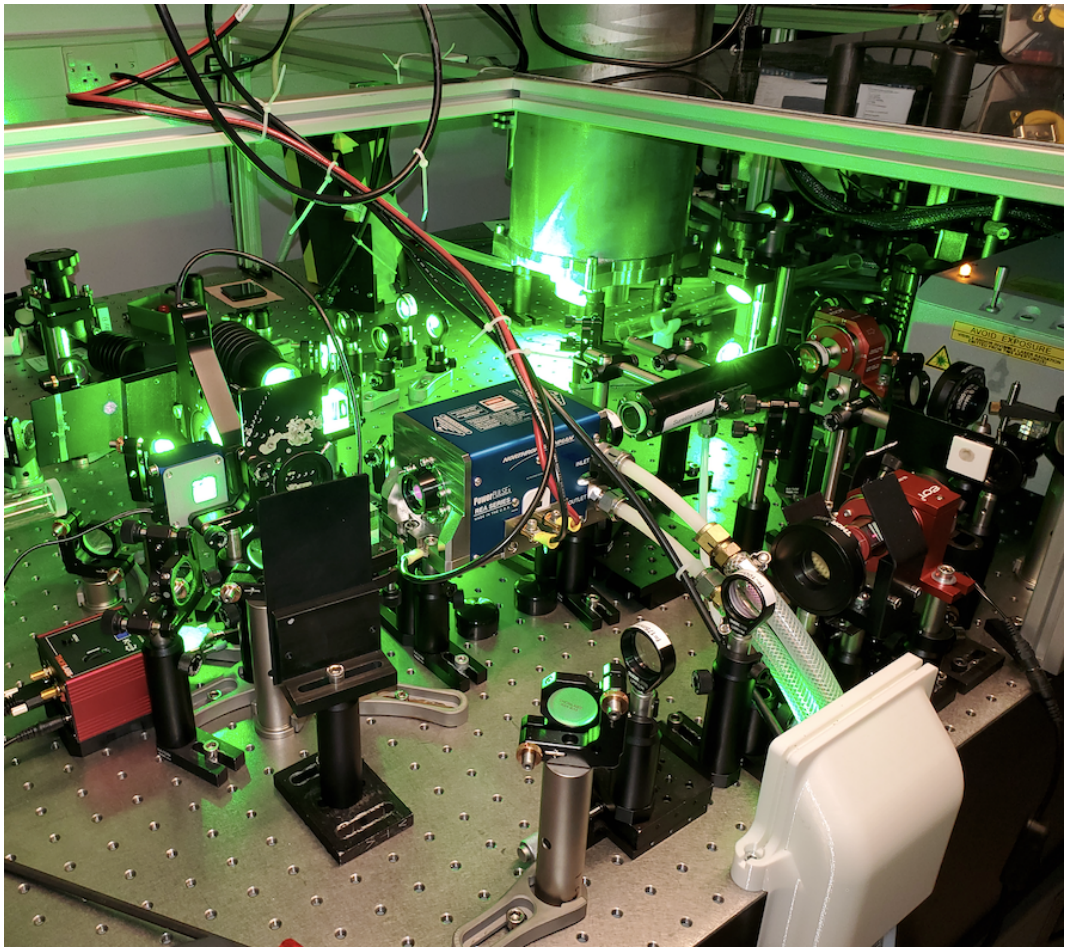


Figure 4.15: DPSS side pumped QCW Gain module setup, with LBO as frequency doubling crystal.

4.2.1 Gain module thermal lensing characterisation and compensation

A side pumped DPSS Nd:YAG gain module with QCW (quasi-continuous wave) diode arrays from a commercial off-the-shelf supplier was chosen (CEO model REA10006-2P200H), to pump a Ti:sapphire amplifier. A nanosecond seed laser (EKSPLA NL230) operating at 150 millijoule was used to extract energy from the module. The chosen module has a laser diode array operating at 24 kilowatts peak electrical power, 12 kilowatts peak pump diode optical output power, providing 1 joule stored energy per pulse within the YAG rod.

The side-pumped DPSS gain-module chosen to amplify the seed 1064 nm laser operates at 100 Hz, 165 A, 145 V, with a 250 µs flat top current pulse shape, generating potentially up to 600 W of thermal load into the package.

In figure 4.16, a strong focusing effect can be seen stepping through different pumping current, along with strong depolarisation effect which will be described in the following sections.

A 633 nm CW laser was used to characterise the gain module's single-path thermal-lensing focal length. This enabled us to estimate the compensation optics required to achieve a collimated output in preparation for high efficiency amplification and frequency doubling. An adjustable telescope beam expander was used to provide slight collimation adjustment. At full operating current, the single-pass focal length of 1.75 m was measured. The results are shown in Figure 4.17. Without compensation, using this in double-pass mode would cause the laser to focus on the optics, most certainly damaging them.

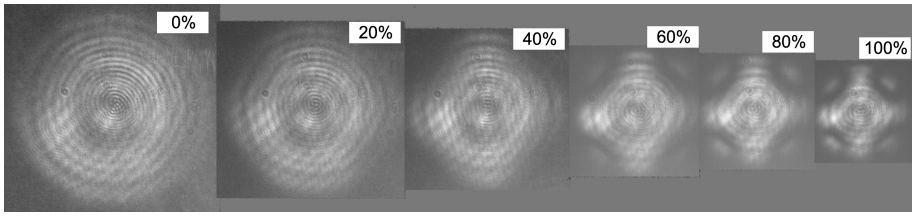


Figure 4.16: Thermal lensing and depolarisation of a YAG laser amplifier for pumping high repetition rate Ti:sapphire amplifier. From left to right shows output beam profile at 0% to 100% thermal loads. Pumping with laser diode array operating at 100 Hz

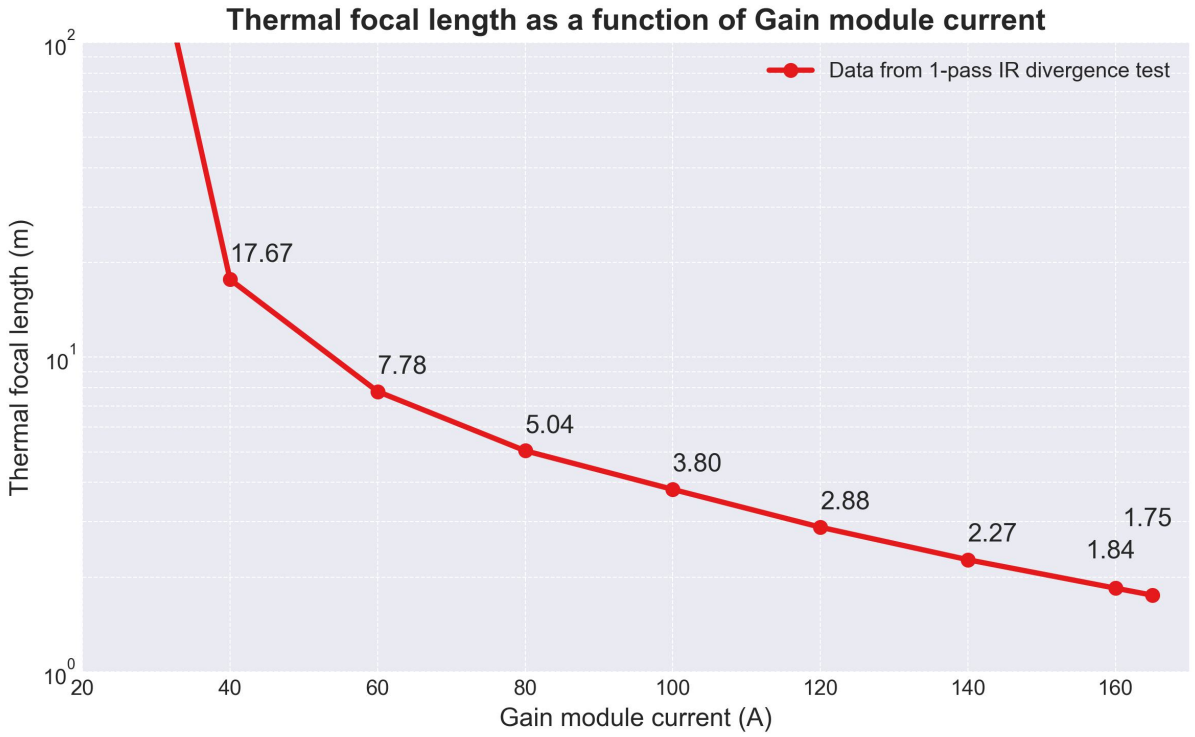


Figure 4.17: Gain module measured thermal lensing focal length

To achieve high conversion efficiency (limited to 70% from IR to green, to comply with damage threshold limitation for large aperture amplifier with near field hot spot), LBO was chosen as a state-of-the-art material frequency doubling crystal [11].

4.2.2 Single and double pass configuration efficiency

System power-added efficiency (PAE) and output energy was characterised with single and double path configurations. A single path design is significantly simpler to compensate for thermal lensing.

Figure 4.18 and Figure 4.19 shows the energy output and efficiency differences of a gain module under single and double pass configurations. When operating in a double pass mode, the module effectively amplifies a seed energy of 120 mJ to achieve an impressive 690 mJ at a 100 Hz frequency, highlighting the efficiency of the two-pass system. To achieve higher energy and higher efficiency, a double pass configuration with polarisation rotation was experimented with and comparably chosen [12]. The polarisation rotation feature of the double pass gain module setup will be discussed in the next section.

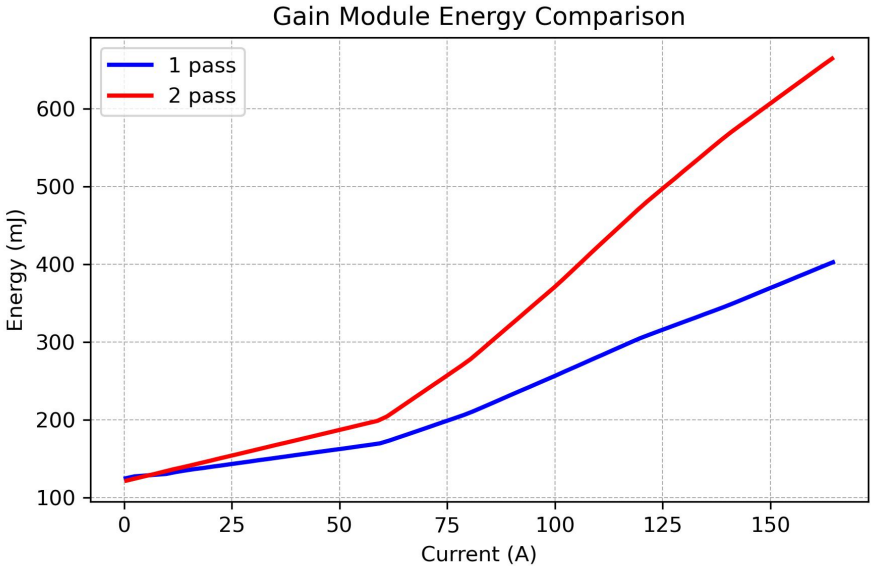


Figure 4.18: Gain module output energy at single pass and double pass configuration, outputing 690 mJ at 100 Hz with 2 passes, seeding with 120 mJ.

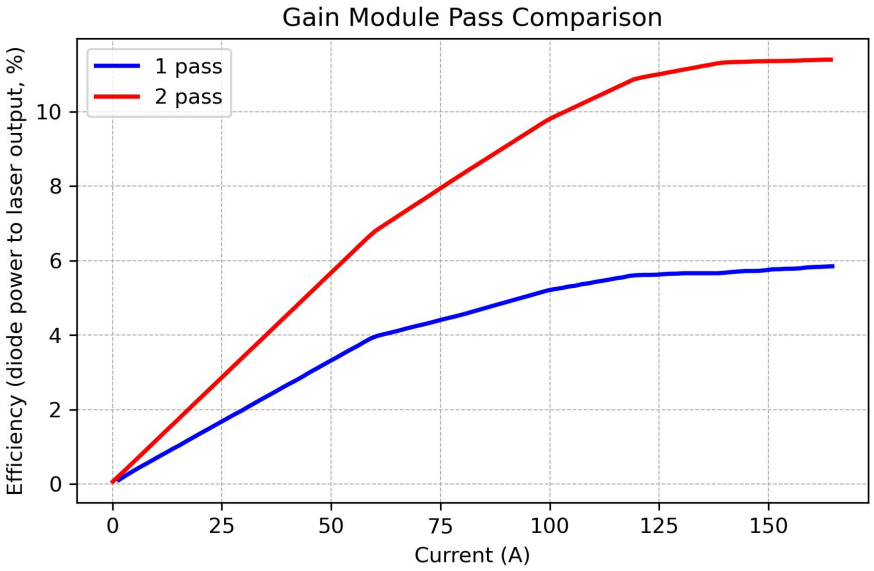


Figure 4.19: Gain module fundamental output power added efficiency at single pass and double pass configuration.

4.2.3 Thermal depolarisation compensation

High repetition rate operation of YAG amplifiers can give rise to significant thermal effects, one of which being thermally induced depolarisation. This phenomenon results from the non-uniform temperature distribution within the amplifier, leading to spatial variations in refractive index.

As the laser beam propagates through this thermally stressed medium, the induced birefringence due to the photoelastic effect can distort both the phase and polarisation of the beam [13].

The primary implication of this effect in YAG amplifiers is the loss of polarisation purity. As some part of the beam becomes spatially depolarised, its interaction with subsequent optical components, especially the Faraday isolator, can become suboptimal, leading to efficiency losses discussed later, or potential damage such as shown in Figure 4.20.



Figure 4.20: Depolarisation return beam damaging polarised beam splitter cube, also ablating Faraday isolator housing.

At the full operating current and 100 Hz, depolarisation is a major issue, causing nearly half of the energy to be at the incorrect polarisation as evidenced in Figure 4.16. This, coupled with thermal lensing, means the reflected depolarised light can damage optics. This effect needs to be lowered for both the system's reliability and efficiency. At a reduced rate of 25 Hz, depolarisation lessens significantly, and at 10 Hz, it is hardly noticeable. By using a Faraday rotator, from which the block diagram is shown in Figure 4.22. Thermally induced depolarisation in YAG can be significantly mitigated by using a double-pass configuration combined with a Faraday rotator. The Faraday rotator compensates for the depolarization introduced in the first pass by

rotating the polarization orientation. On the second pass, the beam retraces its path, effectively nullifying the depolarization effects experienced initially [14]. The Faraday rotator caused the depolarisation to decrease from 43.3% to 3.4%. This works by making the returning light undergo the same depolarisation process, but in the opposite sense, therefore counteracting the depolarisation effect. A depolarisation scan comparing repetition rate at 25 Hz and 100 Hz, and full energy at 100 Hz measurement with additional Faraday rotator added is shown in Figure 4.21.

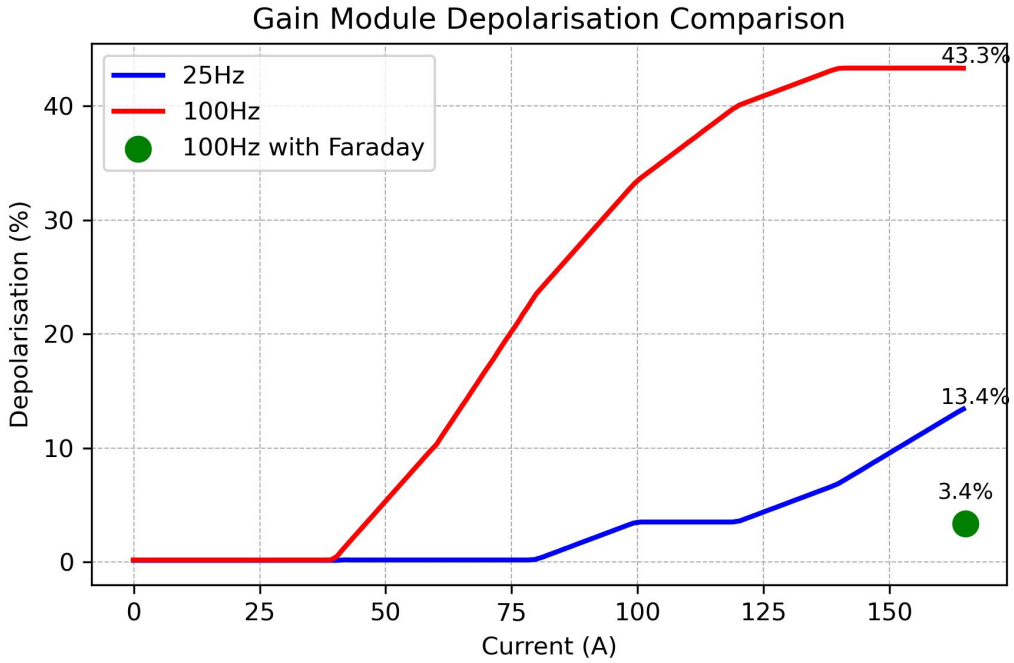


Figure 4.21: Gain module measured depolarisation ratio, with and without Faraday rotator, demonstrating the large depolarisation gain when operating at 100 Hz, compared to 25 Hz.

The system diagram shown in Figure 4.22 includes thermal lensing and thermally induced depolarisation compensation discussed in the following section, and successfully achieved stable long term 100 Hz operation at 690 mJ. Details for the reason for using the gain module in double passes was described previously.

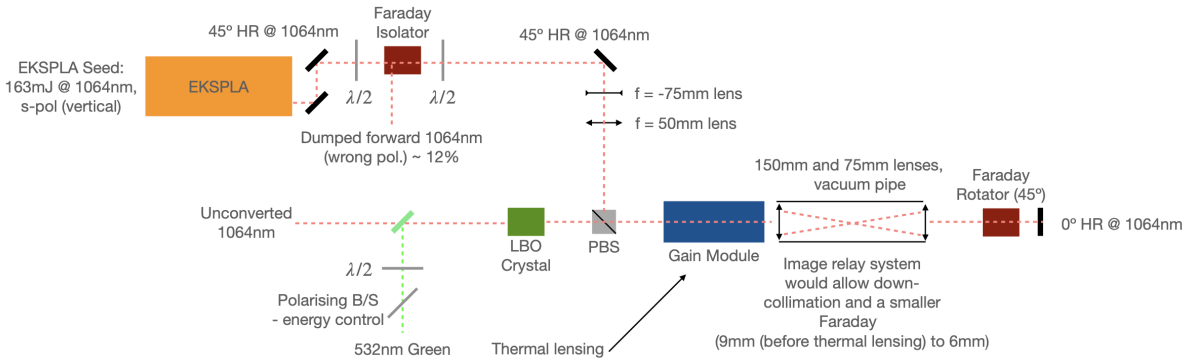


Figure 4.22: Gain module block diagram with depolarisation and thermal lensing compensation

4.2.4 Diffractive diffuser

Diffractive element optics diffusers are commonly used to shape a beam into a flat-top or Gaussian profile in the near field. When used for pumping a Ti:Sapphire amplifier, these types of diffusers ensure that the pump beam's energy is distributed more uniformly across the laser medium. The primary function of the diffractive element is to manipulate the phase of the incoming light in a precise manner, resulting in the desired flat-top intensity distribution in its first order. This even illumination across the Ti:Sapphire crystal promotes consistent amplification, reducing potential hotspots and thermal inconsistencies. Consequently, the laser amplifier operates with a better output near field profile.

Through the use of diffractive diffuser [15] with first order efficiency of about 70% due to losses in other diffraction orders. We achieved relatively even pump profile of 532 nm onto the cryogenically cooled amplifier crystal discussed later, close to a Gaussian beam profile as shown in Figure 4.23. Comparison of a typical near field profile from a top-hat profile seed YAG laser after long distance propagation, and the globally smoothed Gaussian nearfield with local hot spots is shown in Figure 4.24.

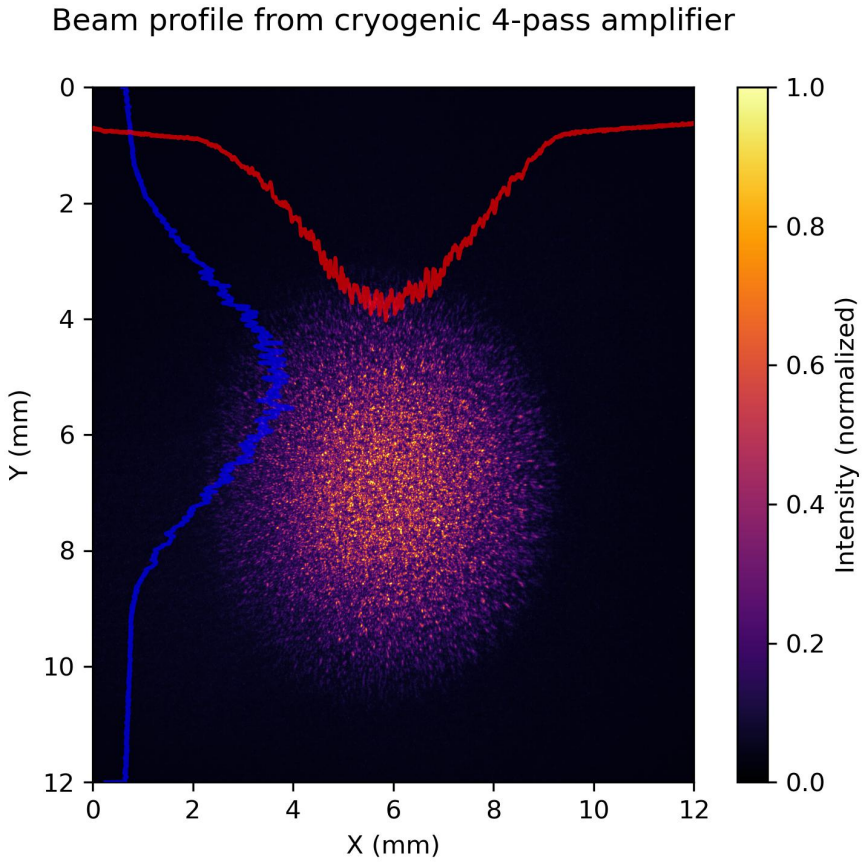


Figure 4.23: Pump profile at crystal plane, hot spots are due to intrinsic property of diffractive diffuser

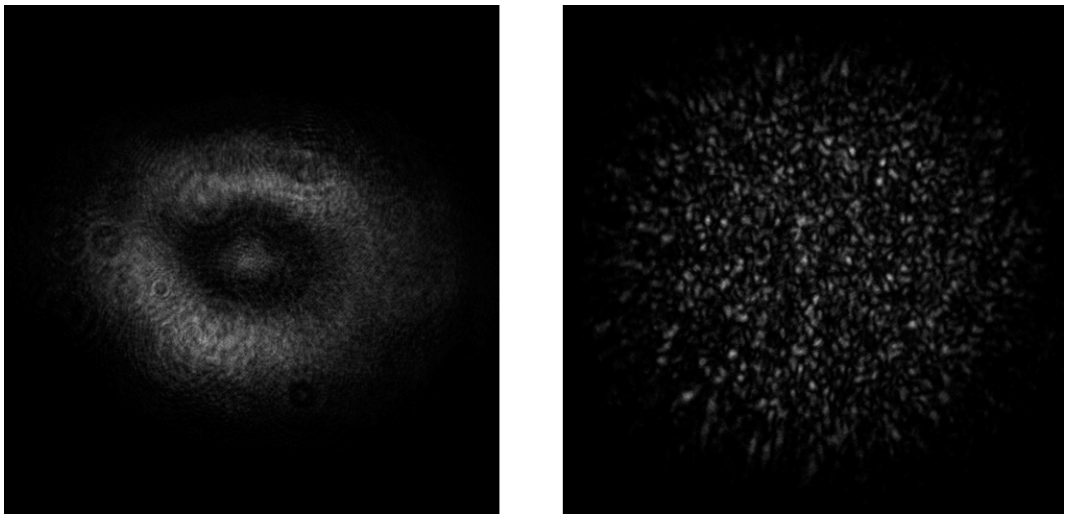


Figure 4.24: Comparison of a poor nearfield profile from a commercial YAG laser, before and after a diffrative element diffuser

4.3 Multi-pass cryogenic Ti:sapphire amplifier

The multipass amplifier further amplifies output from the regenerative amplifier, resulting in slightly better energy stability with significantly higher energy, due to its saturated output design. It has the potential to achieve 150 mJ output. However, due to the time restriction of this work, it was only characterised before a functioning high energy regenerative amplifier was available. This amplifier in a 4 - pass configuration achieved 20 times energy gain from a 3 mJ seed delivered from a previous generation of room temperature regenerative amplifier. Assuming similar gain, if seeded with a 8 mJ regenerative amplifier, it will be reasonable to expect a 150 mJ output from a 460 mJ pump, resulting in 32% efficiency. This expectation is in reasonably agreeing with previous work by various groups [16][17].

4.3.1 Thermal lensing characterisation and design

Single path thermal lensing focal length was simulated and verified similarly to the process described previously. A 460 mJ 532nm 100Hz pump source was used. After 3 passes if not compensated, the beam will be focusing on optics therefore damaging them, as shown in Figure 4.25.

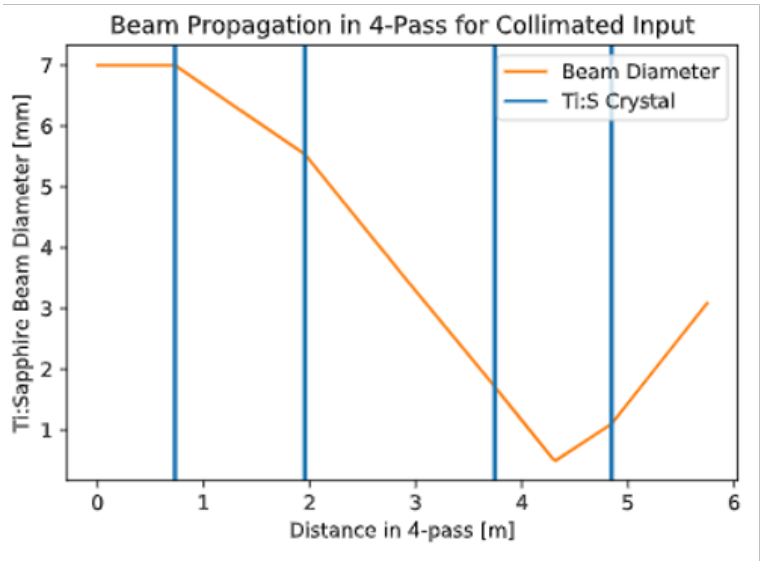


Figure 4.25: Simulated beam size at different point of the 4-pass amplifier with 100Hz 460 mJ pumping

It is worth noting that compensating with fixed curvature mirrors can achieve stable operation.

However this comes at the cost of sophisticated start-up routine and thermally interlocked protection systems to avoid cold starting. Therefore a cryogenic amplifier was again chosen to simplify operation despite the slightly narrower gain profile which can be mostly compensated with either custom coating, Rugate filter [18], or an acousto-optic programmable dispersive filter (AOPDF) [19].

4.3.2 High load cryogenic amplifier

A cryogenic amplifier for high head load and good thermal contact between liquid nitrogen and the Ti:sapphire crystal was designed and manufactured as shown in Figure 4.26, achieving adequate vacuum (9×10^{-10} mbar) even before cooling, ensuring operational longevity and stability.

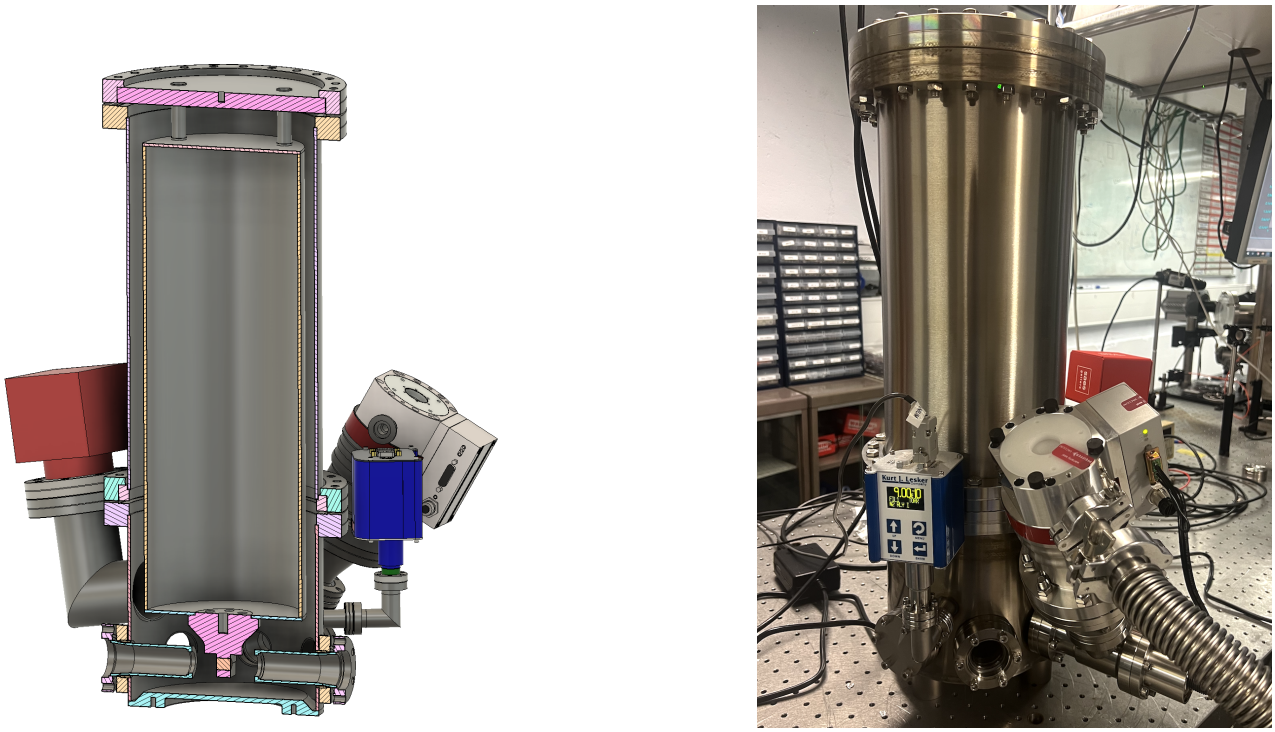


Figure 4.26: 4-pass amplifier CAD design and assembled during initial pumping

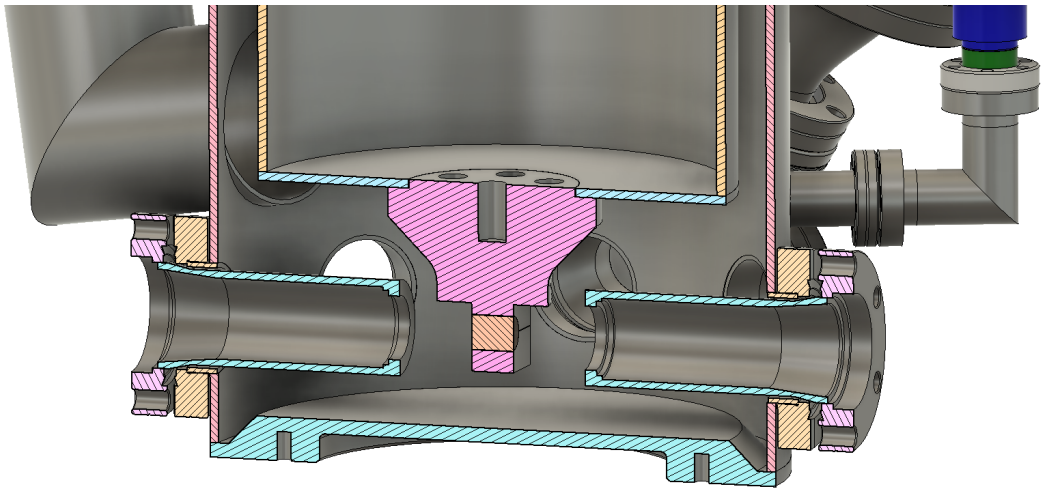


Figure 4.27: Recessed window to maximise acceptance angle for optimum pumping geometry

This type of cryogenic amplifier was characterised with 3 mJ input energy, 310 mJ pump energy (including diffractive diffuser loss), and achieved 60 mJ output with a beam profile shown in Figure 4.28, operating at a large signal gain of 20. At the time of testing this amplifier, the previous stage of cryogenic regenerative amplifier described in the previous section was not implemented nor designed, limiting the full potential of this 4-pass amplifier. With future work, combining both cryogenic stages operating at the same time, it is expected to higher output energy, with expectation of 30% pump conversion ratio in saturation reported widely in previous studies [20][21].

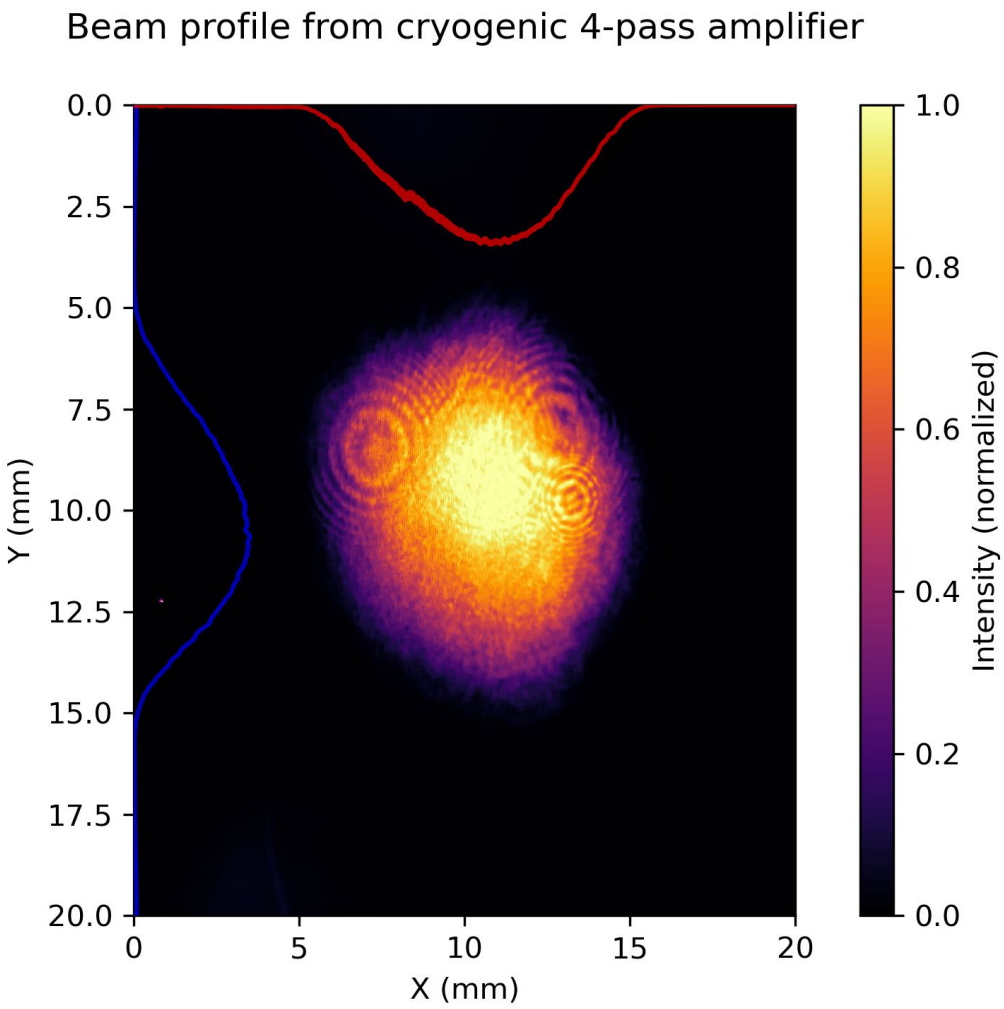


Figure 4.28: 4 pass amplifier output beam profile, 60 mJ

The integrated cryostat container can be filled with up to 5.88 kg of LN2. Given the latent heat of vaporisation for liquid nitrogen at 199,200 J/kg, the total energy required to vaporise this quantity of LN2 is 1.1 megajoules. Considering a 20 W heat load emanating from the crystal and an additional 5 W of heat loss from radiative and conductive loss, the container would require a refill approximately every 12.2 hours of laser operation.

4.4 Vacuum compressor with hybrid grating

In Chirped Pulse Amplification (CPA) lasers, compressor gratings can be the bottleneck for high power operation due to their damage threshold limitations. High-intensity light can cause material degradation or even destroy the grating, limiting the maximum power output.

Additionally, the efficiency of the grating can reduce at high average powers, affecting beam quality due to thermal expansion from light absorption [22]. Gold gratings have significantly higher absorption compared to hybrid dielectric gratings, and are therefore susceptible to higher thermal deformation [23][24]. Previous testing with gold grating shows low overall throughput (50%).

To achieve better spectral and temporal phase, avoiding self-phase modulation in air, as well as with the aim of prolonging the lifetime of these hybrid gratings, a vacuum compressor was constructed, featuring hybrid dielectric - gold gratings. System throughput of 80% was observed with 35 nm FWHM beam after amplifiers.

4.4.1 High rigidity grating mount

A highly rigid grating mount was designed with the kinematic principle in mind, utilising medium preload angular contact bearings. These grating mounts shown in Figure 4.31 have proven to be repeatable and presents no noticeable drift with daily operation.

The principle of elastic averaging was used to achieve high degree of stiffness with low friction, while not requiring unreasonable precision in its components [25]. Matched pairs of hybrid Si3N4 ceramic ball bearings were used. Applying light preload can achieve smooth rotation with no lost motion, while making sure all balls are in contact, therefore providing long moment arm and large stiffness against vibration. No lubrication was used for vacuum cleanliness. However, due to the material choice and the amount of preload, no galling effect was noticed, similar to reports on space applications [26]. This design is shown in Figure 4.29. The highlighting in blue is the discussed hybrid ceramic bearings.

Special notice has been taken to avoid trapped volume, in order to achieve good vacuum quality immediately next to grating optical surface. In addition, the normally used phenolic resin ball retainers were replaced with PEEK plastic retainers, which would not emit the absorbed rust preventative oil as organic vapour from stock retainers. This in principle should prolong the lifetime of hybrid dielectric gratings. Sapphire pads were implemented to be in contact with rotating adjuster screws, this ensure small motions are not randomly lost to friction, as well as the longevity against repeated adjustments.

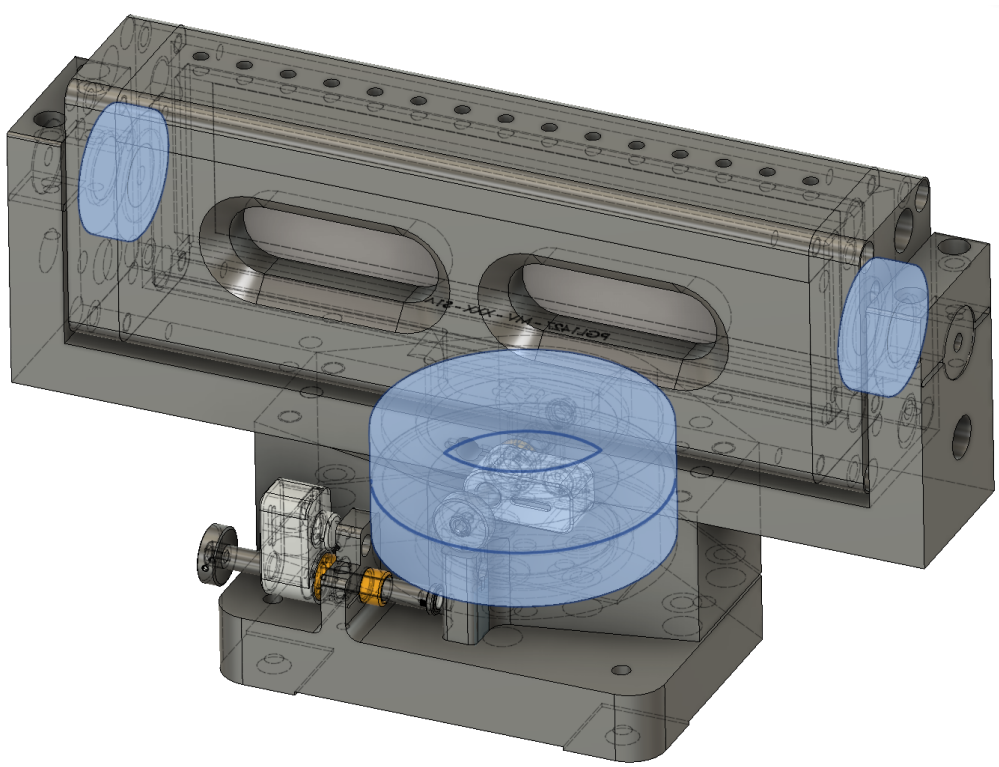


Figure 4.29: Drawing for vacuum compatible grating mount, consisting of rotational joints from elastically averaged balls with high stiffness highlighted in blue.

A model of the compressor chamber along with the double balanced bellow [27] with constant displacement was created to analyse its modal response, avoiding commonly used pump frequencies. This model was also used to perform the optical path planning, including the design of stage travel to provide long pulse capabilities. This model is shown in Figure 4.30, including provisioned stiffness enhancement cross frames shown underneath the chamber, which have not yet been implemented.

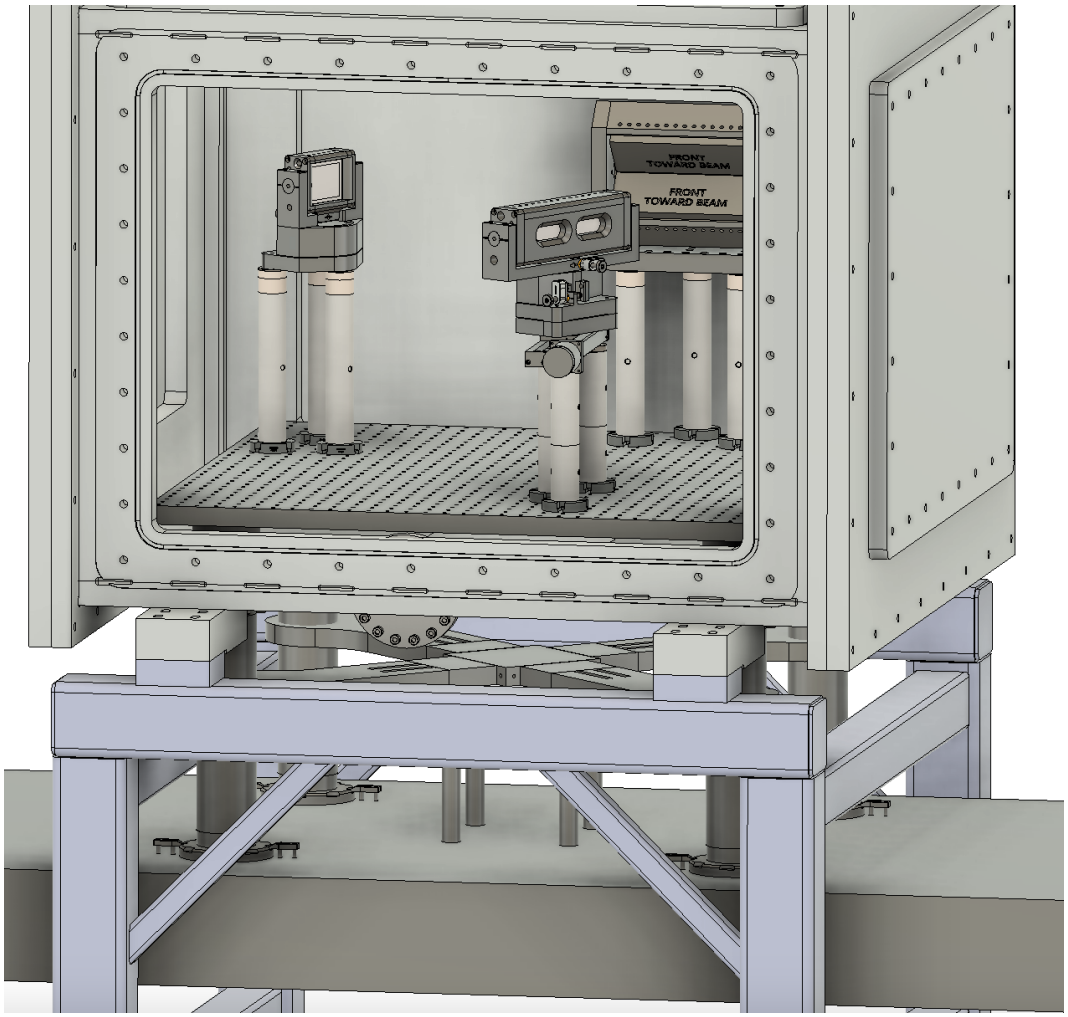


Figure 4.30: Setup drawing for vacuum compressor with rigid grating mounts and roof mirror mount

Figure 4.31 shows the vacuum compressor chamber internals. A turbo pump with active 5-axis magnetic levitation (Pfeiffer model ATP 2300 M) was installed on top of the chamber, to provide high pumping speed in order to account for experimental contaminant drifting into the compressor chamber. The grating and dielectric roof mirror were installed under general vacuum practice. High vacuum compatible terminal blocks with PTFE were manufactured without coolant to meet the cleanliness requirements. They are shown in the figure as white blocks connecting Kapton insulator wire and picomotors. Additional access ports were added in order to creat access for illumination light sources, damage monitoring cameras, and various diagnostics.

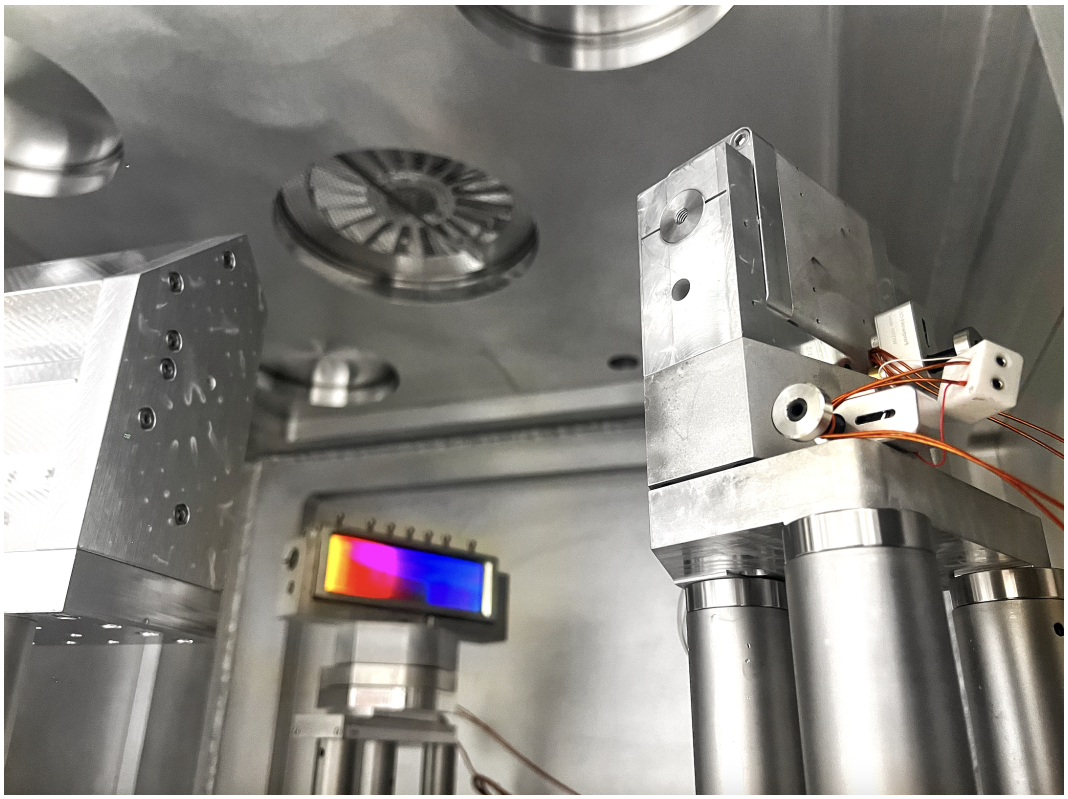


Figure 4.31: Rigid grating mount with preloaded angular contact bearing pairs, providing elastic averaging of motions and high stiffness under small signal vibration conditions. The mounts are loaded with hybrid dialectric gratings, and vacuum compatible picomotors.

4.4.2 Damage threshold testing

A LIDT (Laser induced damage threshold) test with the stretched (around 100 picosecond) and compressed (30 femtoseconds) 800 nm beam was performed on these gratings. Damage under the microscope shows clearly dielectric layer delamination at intensities above the LIDT as shown in Figure 4.32. It was determined that the LIDT is close to $0.05\,\mathrm{J/cm^2}$ with short pulse. Therefore, with a margin of 2 to take account of the hot spots in the laser near-field, a beam diameter of 20 mm was chosen to accommodate a 100 mJ beam.

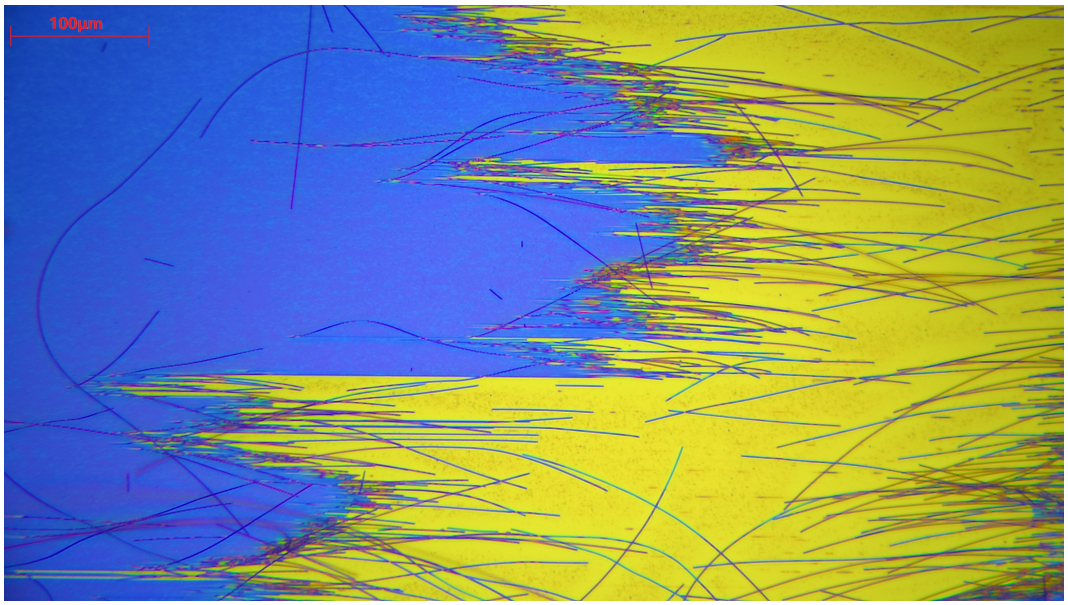


Figure 4.32: Hybrid dielectric grating laser induced damage

4.5 Wavefront sensing

Wavefront sensing is a method used to measure the shape and distortion of incoming light waves. By comparing the incoming wavefront to a reference plane or spherical wave, distortions or aberrations can be determined. These measurements can then be used to correct optical systems or analyze the quality of a light source. Common techniques include the Shack-Hartmann sensor, which divides the incoming light into multiple segments and measures the tilt in each segment to reconstruct the overall wavefront shape.

High-power lasers require wavefront sensing to ensure accurate focusing and high-quality focal spots. As mentioned in chapter 2, wavefront aberrations can degrade focal spot quality, reduce system efficiency, and risk damaging optical components. Accurate wavefront data also allows for corrections that optimise energy concentration in the focal spot.

4.5.1 Shack Hartmann

In wavefront sensors that utilise a mask, an array of spots or diffraction rings is projected onto the focal plane, as depicted in Figure 4.33. Each of these elements can either be a pinhole or, when dealing with limited photon flux, a zone plate, or a small lens from a lenslet array [28].

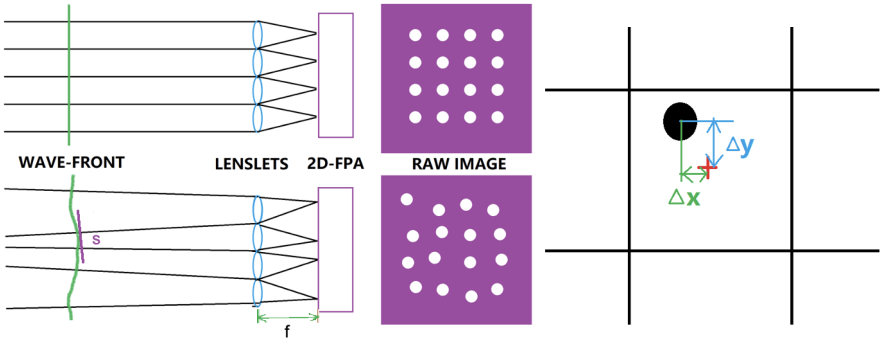


Figure 4.33: Illustration of wavefront detection

The wavefront $W(x, y)$ can be digitised using a commercial focal plane array and centre extracting algorithm, a wavefront distortion can be calculated with $\frac{\partial W(x,y)}{\partial x} = \frac{\Delta x}{f}$ and $\frac{\partial W(x,y)}{\partial y} = \frac{\Delta y}{f}$. Calibration with a precision turntable in conjunction with an autocollimator can be used to further remove non-linearity induced in mask manufacturing, as well as due to the sensor coverglass thickness.

The local wavefront gradient can be calculated with geometric optics methods illustrated in Figure 4.34 [29]. The local gradient is given by: $\frac{\partial(\Delta W)}{\partial h} = \frac{\Delta y}{L} = \frac{y_0(\Delta z)}{(z_0-\Delta z)(z_0+L)} = \frac{\Delta z h}{(z_0-\Delta z)z_0}$.

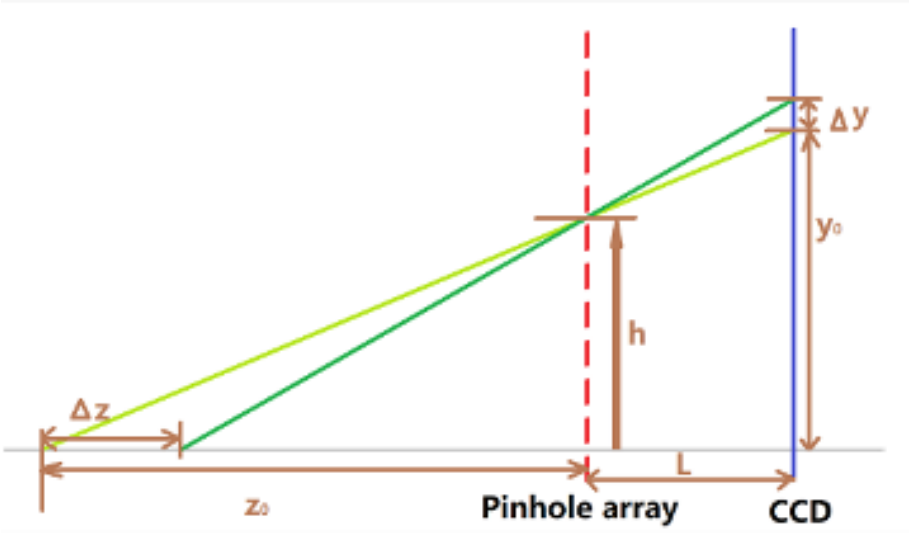


Figure 4.34: Pinhole image of a localised wave direction

4.5.2 Diffractive elements

Zone plates and pinholes are commonly used as diffractive optics.

Utilising a pinhole array for wavefront sensing works by observing the angular deflection

of light beams as they pass through each pinhole. When a distorted wavefront encounters the pinhole array, the light beams' exit angles vary based on the local wavefront slope at each pinhole. By measuring the position of each beam after it passes through its respective pinhole, the angular deviations can be quantified. These angular measurements across the entire array can then be used to reconstruct the overall shape and distortion of the incoming wavefront. Essentially, each pinhole acts as a localised wavefront tilt sampler, and collectively, they provide a detailed representation of the entire wavefront's deformations.

For a circular aperture (pinhole), its far-field image is composed of a series of concentric rings surrounding a solid spot known as Airy's disc (figure 4.35). The size of the inner spot is given by $\rho_{spot} \propto \frac{1}{D}$, where D is the diameter of the pinhole. In certain applications, a pinhole-based mask can provide adequate performance without the need for any transmission elements, provided there's a sufficiently large area and high resolution on the image plane [30]. A detailed wavefront measurement can be conducted using multiple pinholes, often involving thousands of pinholes arranged in an array [31].

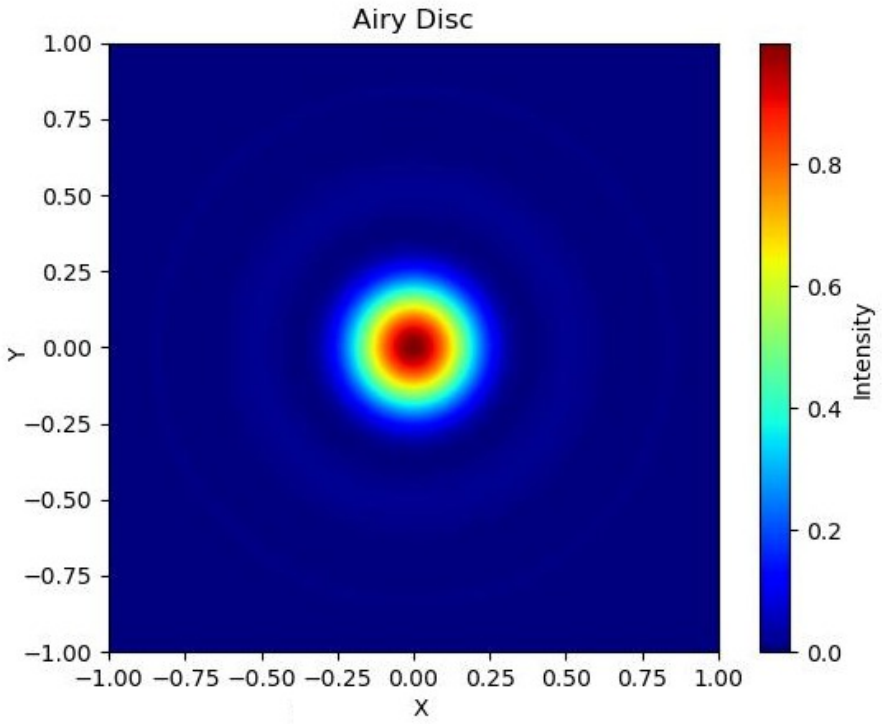


Figure 4.35: Airy's disk

In the case of a pinhole array, the spatial resolution which represents angular resolution

post-mask is primarily governed by the Rayleigh criterion [32]. For a circular aperture, this resolution limit can be expressed as

$$\theta_R = 1.22\frac{\lambda}{d}$$

.

A zone plate serves as an advanced version of a pinhole, designed to cause light to interfere constructively onto a specified image plane [33]. The radius for the rings is dictated by the relation

$$r_t = \sqrt{n\lambda f + \frac{1}{4}n^2\lambda^2}$$

. Given this, the first order focal length is described as $f = \frac{2r_n\Delta r_n}{\lambda}$, where r_n represents the diameter of the outer ring and Δr_n denotes its width. The utmost resolution achievable by a zone plate is expressed as $l_R = \frac{l}{1.22}$, with l being the smallest feature size utilised in the construction of the zone plate.

Due to the focused, smaller spots created by the zone plates, more measurement points can be achieved over the same area without overlapping, leading to a higher spatial resolution of the wavefront measurement. This allows for denser sampling of the wavefront without increasing the size of the sensor.

4.5.3 Diffractive element array based wavefront sensor design

The benefit of using a pinhole array as wavefront mask is, if done correctly, a pinhole array provides much higher sensitivity, about 100 times according to a temperature stabilised study [34], compared to a similar focal length lenslet array, at the cost of low transmission. But this is not generally an issue for laser plasma diagnosis due to the high probe energy available.

Very accessible manufacturing techniques, such as laser drilling, as compared to the lithography gratings used to make QWLS (Quadriwave lateral shearing) masks and custom glass mold casted lenslet array, can be used for the manufacturing of such masks. The material choice can be metal, which is significantly better for thermal management as compared to glass, which is the main source of error in high sensitivity measurements.

Application specific mask design can be adopted for specific needs but it is prudent to share

the same sensor which is the main cost for such a system. A balance between effective focal length, distance from pinhole to focal plane array, and pinhole diameter should be considered to achieve both desired sensitivity and dynamic range. Large, or very large image area can be selected for direct detection of beams and plasma fields without the need for complicated resizing lenses. This method eliminates aberrations and drift generated by glass lenses.

We manufactured a pinhole array from laser micro machined tunsten sheet, and achieved a 14 times larger area compared to the biggest commercial wavefront sensor. See comparison in table 4.2. High pixel count ensures better wavefront sensitivity. Higher pinhole density (spatial resolution), and 37 times the pixel count as compared to the highest resolution commercial wavefront sensor is readily available. Therefore a range of spatial resolution and wavefront sensitivity can be selected exceeding commercially available wavefront sensors.

The figure 4.36 showcases the use of commercial ray-tracing application of Ansys Zemax for the purpose of designing the most suitable pinhole size and spacing. Zemax's commercially supported optical simulation capabilities have been leveraged to account for real-world wavefront conditions, explicitly considering factors such as spherical aberration and near-field distribution. The visual representation illustrates the arrangement of pinholes, indicating the ideal size and distance between them to achieve optimal wavefront sensing, all while factoring in the mentioned aberrations and near-field distributions.

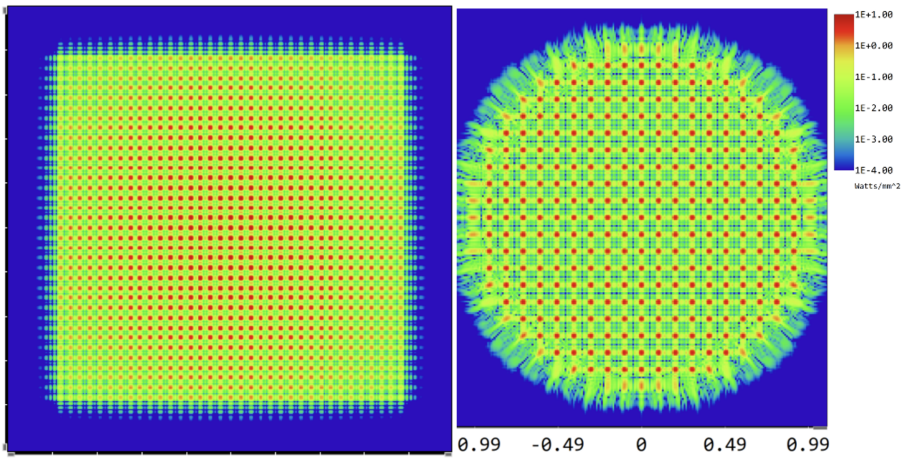


Figure 4.36: Ansys Zemax was utilised to design the optimal pinhole size and pinhole spacing, with realistic wavefront including spherical aberration and near-field distribution.

Table 4.2: Comparison of different sensors.

	HASO3 GE2	**Phasics or Thorlabs S-H**	**Phaseone IQ4 150 Achromatic**	**Dalsa leaf aptus 80MP Color**
Dynamic range	FSI,	FSI, 60dB	BSI, 94dB	FSI, 72dB
Pixel count	4 MP	4 MP	151 MP	80 MP
Size in mm	14 by 14	11 by 11	54 by 40	54 by 40
Description	Largest commercial wavefront sensor	Typical sensor used in many scientific camera / wavefront sensors	No Bayer colour filter, highest spatial resolution, good IR sensitive	"Relatively" cheap but color filtered, reduced IR sensitivity

4.5.4 Image sensor

The pinhole mask idealy should be coupled to a high pixel count focal plane 2-D image sensor. A major advantage of making a custom detector, besides being significantly lower cost, is the incorporation of numerous advancements in the field of CCD and CMOS 2-D focal plane arrays that have been primarily driven by consumer electronics. Except for a few specialised low-noise applications, there is generally little to no performance advantage in choosing specialised sensors, like those used in Phasics and HASO wavefront sensors, over those found in consumer-grade detectors of a similar generation. High-end scientific cameras typically lag one to two generations behind consumer cameras in terms of sensor size and total pixel count. Table 4.2 provides a comparison between the sensors used by the two most accurate wavefront sensor manufacturers and those used in two consumer cameras, also shown in Figure 4.37.

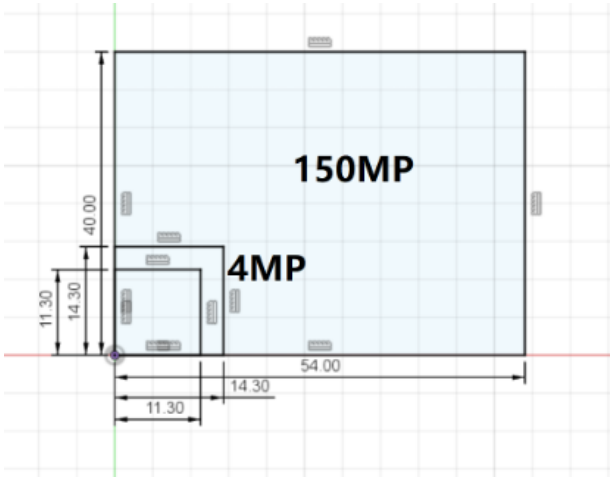


Figure 4.37: Size comparison of different commercially available silicon based focal plane arrays

4.5.5 Thermal design

Thermal drift and material annealing is the primary sources of imperfections when characterising performance. The added holes in the pinhole mask can distort the internal stress distribution in the metal substrate. Therefore slow release of stress changes the shape of the pinhole array irregularly when temperature changes. This will introduce unwanted high-order error in the wavefront measurement. The mount geometry will also affect alignment which introduces tilt error, and also impacts on the accuracy of the calibration.

The target distribution for a 1/100 pixel pitch is expected to vary within a 100 nm range due to the intrinsic sensor noise. As a result, thermally induced drift must be rigorously controlled. While Invar alloy would be the material of choice for creating the mounting structure of the pinhole plates, resource limitations led us to use cast aluminum tooling plate in the prototype instead. The short-term stability, measured over 100 seconds, exceeds the limitations of our current measurement capabilities.

Figure 4.38 shows the heat sinking capability of a metal pinhole array with support frame. Thermal equilibrium time should be considered if used at high repetition rate. A typically seen probe energy of 20 mJ at 100 Hz was modeled, completely absorbed into the thin mask. A rise in temperature of 50 K can be expected, which will require materials with low thermal expansion coefficient to minimise drift.

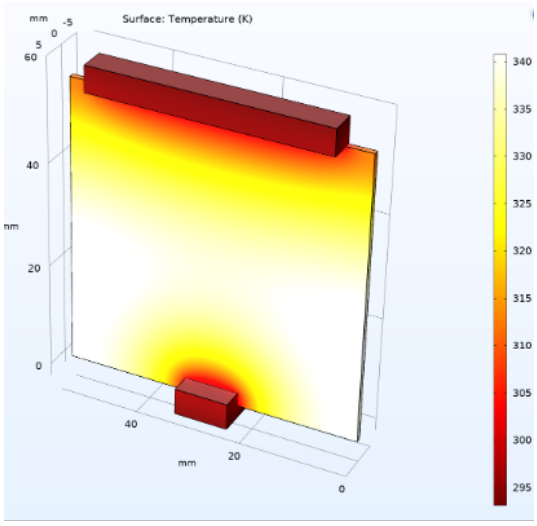


Figure 4.38: Comsol was used to simulate 2 W absorbed optical power on a 50 micron pinhole array with adjustable mount

4.5.6 Wavefront sensor characterisation

The roundness of the pinhole and the quality of its wall finish are crucial for forming an even Gaussian spot on the focal plane. High precision in locating the center of light spots is crucial for accurate wavefront reconstruction. Small inaccuracies in centroid determination can introduce errors in measuring the local slope of the wavefront. The interpolation resolution is often required to be at 1/100 of a pixel pitch, necessitating a robust Gaussian fitting algorithm that can accommodate minimal asymmetries and irregularities in the pinhole finish. To meet these specifications, a laser-drilled mask was fabricated and its roundness was verified using an optical Coordinate Measuring Machine (CMM) [35]. Tungsten was selected as the material of choice to ensure maximum rigidity at elevated temperatures during thin-sheet manufacturing. Attempts to make the mask with stainless steel were made, but the material experienced significant deformation during the laser-drilling process.

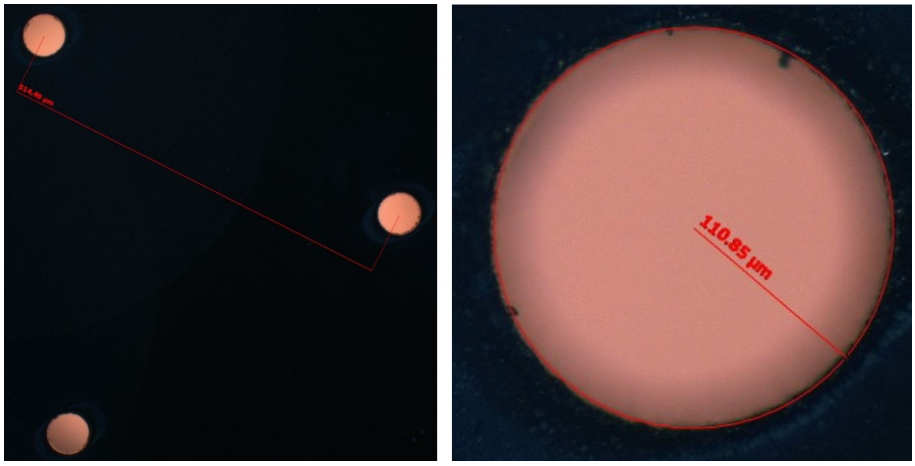


Figure 4.39: Optical CMM measurement of laser drilled hole sample

Due to the natural taper wall from laser drilled holes, one side of the mask accumulated more internal stress during drilling. This resulted in a bent mask in its rest state. A tensioning arm was added to stretch the mask flat. Stability was compromised this way. Therefore further work needs to be performed to ensure minimal geometric drift. Similar work has being proven to be possible by Brooks and Aidan in 2007 [34], however on a much smaller scale. Micro-machining can provide the solution to taper-less wall finish of each holes.

Calibration needs to be conducted in-situ once the device is installed in its actual diagnostic

probe position, to compensate for any imperfections from environmental influence. To assess the intrinsic uncertainty within the optical train, a standard off-the-shelf beam expander was employed. Figure 4.40 illustrates the calibration setup.

A commonly employed computer vision algorithm (erosion and dilation techniques [36]), was used to roughly identify the location of each spot. Subsequent Gaussian fitting was performed to extract sub-pixel location details. The search area can be manually configured to align with the pinhole spacing, resulting in software behaviour that offers robust performance over a large dynamic range. Figure 4.41 displays the central position and search boundaries. Some holes aligned precisely with the dark portions of the beam expander's speckle pattern, resulting in insufficient Signal-to-Noise Ratio (SNR). These instances were automatically disregarded by the algorithm to maintain process robustness.

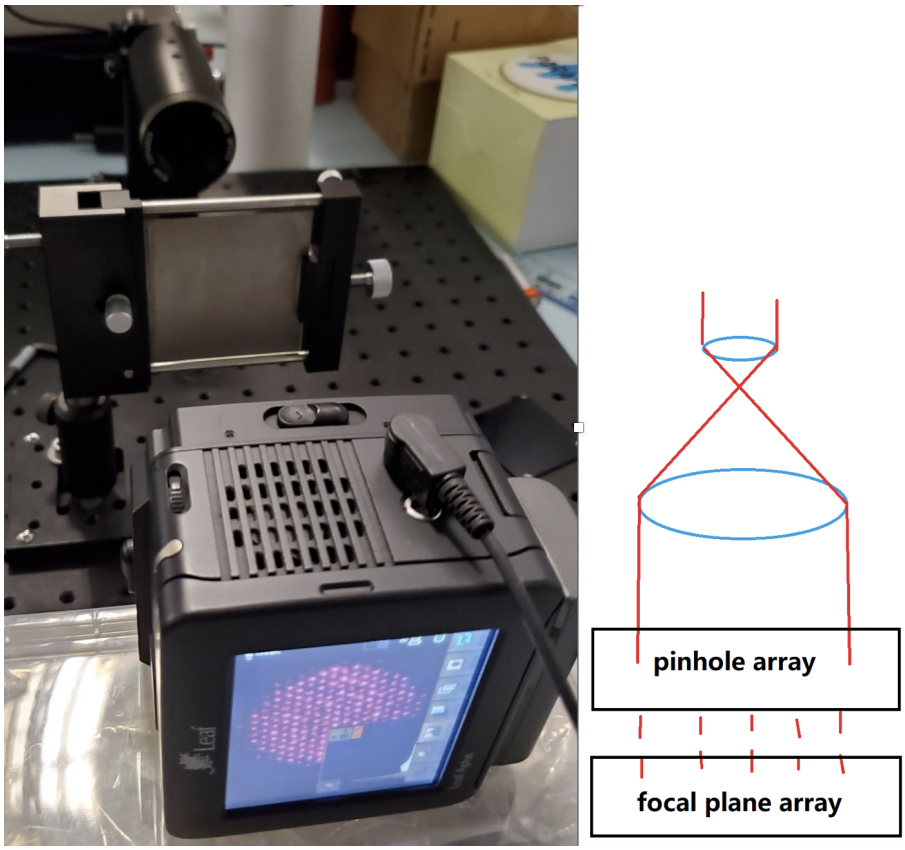


Figure 4.40: Calibration of wavefront sensor with beam expander and diode laser

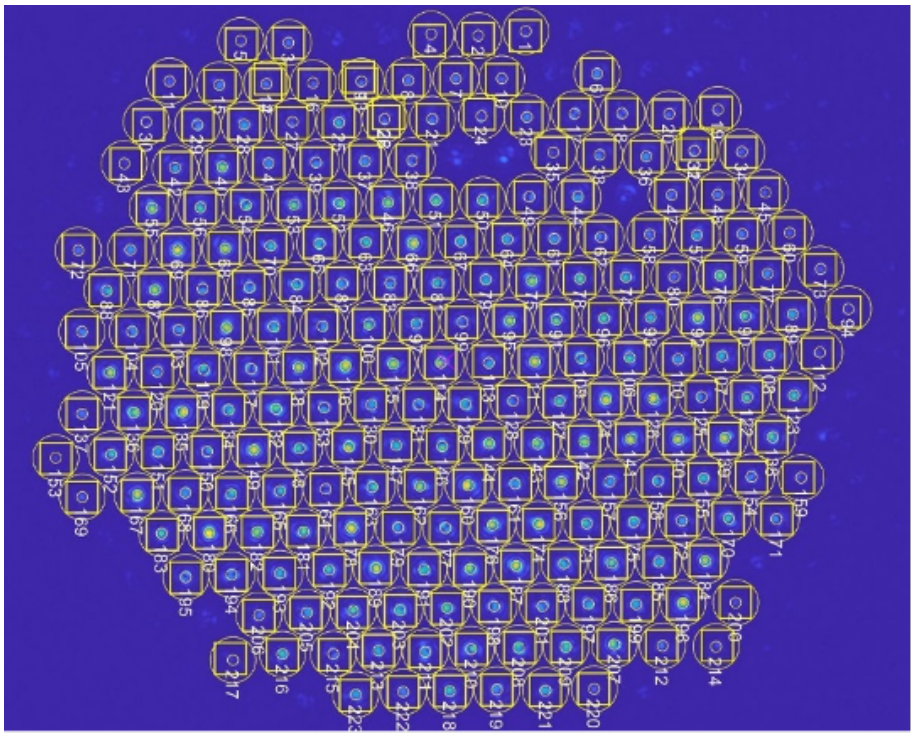


Figure 4.41: Calibration of pinhole array geometry, some distortion and pinhole irregularity can be noticed

4.5.7 Sensitivity evaluation

Immediately after calibration, a series of measurement was performed in a sequence with 100 seconds sampling spacing. Analysis of calibration data determines the typical noise level shown in figure 4.42. An rms level of 0.4 µrad can be achieved before any optimisation to the mounting solution. From the observation of mostly low frequency perturbance, it is likely that the source of noise is introduced from air current and thermal drift of the mask itself.

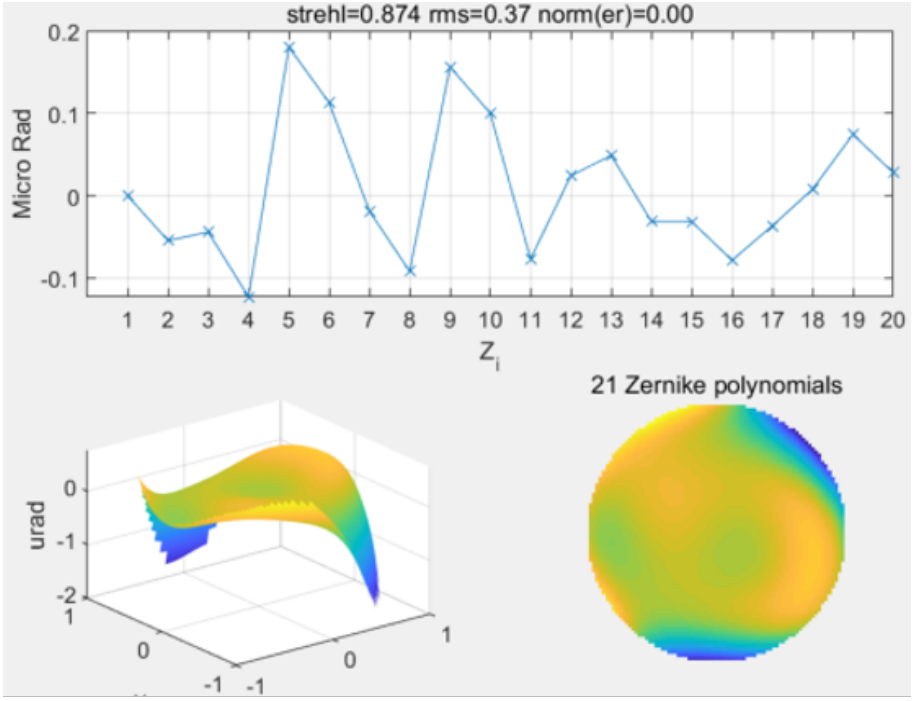


Figure 4.42: Sensitivity evaluation in air, mostly due to air turbulence

4.5.8 Performance conclusion

The sensitivity performance was not as good as expected, mainly due to the lack of thermally stabilised structure. However compared to commercial wavefront sensors, the author already observed at least 10 times better sensitivity (0.1 vs 1 µrad) even under our imperfect set-up as compared to other studies such as one performed with 1 megapixel sensor [34]. Improvement in sensitivity of 1,000 to 10,000 times could be expected if the measuring apparatus is thermally stabilised and placed in vacuum.

The chosen configuration of pinhole spacing and distance to focal plane results with a tilt range of 1.15 degree, compared to the usually 3 degree tile range in commercial wavefront sensors. The pinhole array characterised here was designed for high sensitivity to meet the requirement in diagnosing laser plasma accelerators. Usually there is only small amount of wavefront disturbance in a transversely probed plasma due to the small distance of optical path length. However, the deflection dynamic range can be changed easily by reducing the distance to the sensor if desired.

4.5.9 Future directions for pinhole array based wavefront sensor

Sensitivity is limited by the diffraction from the pinhole, resulting in inaccuracy of centroid finding due to sensor pixel spacing and fill factor imperfections. The use of a zoneplate could further reduce the image spot size. This would increase the density of spatially sampled points by at least 10 times, enabling higher spatial resolution while maintaining similar angular tilt sensitivity. Photolithography and plasma sputter coating processed could be used to produce the fine structure needed for individual zone plates. A wafer stepper stage could be used to cover the large surface area of a zone plate mask. This process would enable better thermal stability. As there is no physical hole drilled into the substrate, its structural integrity and annealed stressless state can be maintained. Combined with a low thermal expansion material such as Zerodur, a higher stability is expected as compared to a laser drilled tungsten mask.

One could also imagine that a higher spatial resolution detector could be used. The focal plane array used in our setup was a 15 years old consumer medium format digital camera, which contains a Bayer colour filter array, effectively reducing the spatial resolution by 4. Combined with its lower total pixel count as compared to modern detectors, this results in a relatively high sampling noise after position extraction. Modern consumer camera with a back-side illuminated monochromatic sensor would be more suitable for this application.

Finally, better thermal stability can be achieved. The mounting structure and sensor spacing breadboard experience thermal drift (aluminium baseplate). Invar alloy and technical ceramics such as silicon nitride [37] can be used to further improve long term stability.

4.5.10 Wavefront measurement on short pulse laser

The pinhole array wavefront sensor has also been explored as a versatile tool for alignment and collimation, as depicted in Figure 4.43. By amalgamating a stainless steel pinhole array with a portable still-image camera, we are able to capture instantaneous snapshots of laser wavefronts for subsequent analysis. Nevertheless, additional work is required to guarantee the portability of not only the hardware but also the wavefront retrieval software, thereby facilitating expedient on-site workflows.

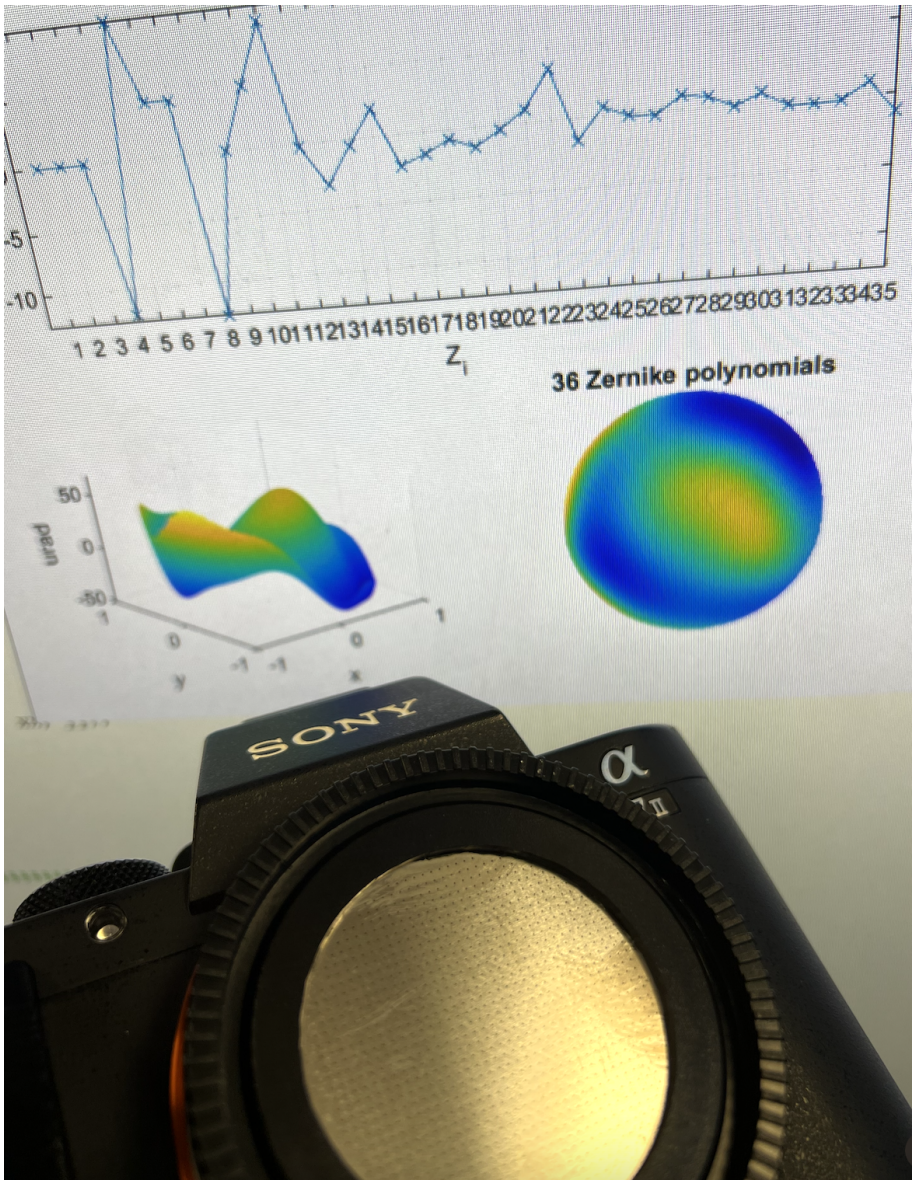


Figure 4.43: Measuring femtosecond laser with 4mJ of energy, using commercially available portable mirror-less camera and permanently mounted pinhole array mask

References

[1] G Cheriaux, P Rousseau, F Salin, JP Chambaret, Barry Walker, and LF Dimauro. Aberration-free stretcher design for ultrashort-pulse amplification. *Optics Letters*, 21(6), 1996.

[2] Gerard Mourou, Corinne Félix, and V. Yanovsky. Why ring regenerative amplification (regen)? *Applied Physics B*, 74, 2002.

[3] Vladimir V Ivanov, Anatoly Maksimchuk, and Gerard Mourou. Amplified spontaneous emission in a ti:sapphire regenerative amplifier. *Applied Optics*, 42(36):7231–7234, 2003.

[4] Isao Matsushima, Hidehiko Yashiro, and Toshihisa Tomie. A 37% efficiency, kilohertz repetition rate cryogenically cooled Ti:sapphire regenerative amplifier. *Japanese journal of applied physics*, 44(6L):L823, 2005.

[5] ZY Wei, ZH Wang, P Wang, WJ Ling, JF Zhu, HN Han, and J Zhang. A compact 355tw femtosecond ti:sapphire laser facility and trend to high contrast ratio. In *Journal of Physics: Conference Series*, volume 112, page 032003. IOP Publishing, 2008.

[6] H. Eilers, U. Hömmerich, and W. M. Yen. Temperature-dependent beam-deflection spectroscopy of Ti3+ -doped sapphire. *J. Opt. Soc. Am. B*, 10(4), 1993.

[7] B Schulz et al. Thermophysical properties of sapphire, AlN and MgAl2O4 down to 70 k. *Journal of Nuclear Materials*, 212:1065–1068, 1994.

[8] A. C. DeFranzo and B. G. Pazol. Index of refraction measurement on sapphire at low temperatures and visible wavelengths. *Appl. Opt.*, 32(13), 1993.

[9] C. Byvik and A. Buoncristiani. Analysis of vibronic transitions in titanium doped sapphire using the temperature of the fluorescence spectra. *IEEE Journal of Quantum Electronics*, 21(10):1619–1624, 1985.

[10] P. Albers, E. Stark, and G. Huber. Continuous-wave laser operation and quantum efficiency of titanium-doped sapphire. *J. Opt. Soc. Am. B*, 3(1):134–139, 1986.

[11] Jonathan P. Phillips, Saumyabrata Banerjee, Klaus Ertel, Paul Mason, Jodie Smith, Thomas Butcher, Mariastefania De Vido, Chris Edwards, Cristina Hernandez-Gomez, and John Collier. Stable high-energy, high-repetition-rate, frequency doubling in a large aperture temperature-controlled LBO at 515nm. *Opt. Lett.*, 45(10):2946–2949, 2020.

[12] Laurynas Veselis, Raimundas Burokas, Orestas Ulčinas, Titas Gertus, Kirilas Michailovas, and Andrejus Michailovas. Depolarization compensation with a spatially variable wave plate in a 116W, 441fs, 1MHz Yb:YAG double-pass laser amplifier. *Appl. Opt.*, 60(24):7164–7171, 2021.

[13] Hans J Eichler, A Haase, Ralf Menzel, and A Siemoneit. Thermal lensing and depolarization in a highly pumped Nd: YAG laser amplifier. *Journal of Physics D: Applied Physics*, 26(11):1884, 1993.

[14] Efim Khazanov, Nikolay Andreev, Alexey Babin, Alexander Kiselev, Oleg Palashov, and David H. Reitze. Suppression of self-induced depolarization of high-power laser radiation in glass-based faraday isolators. *J. Opt. Soc. Am. B*, 17, 2000.

[15] M Currie, P Blair, T Murphy, and R McBride. Customised low-angle refractive diffusers for high power laser applications. In *Proc. SPIE*, volume 9727, page 97270S, 2016.

[16] Inhyuk Nam, Minseok Kim, Tae Hee Lee, Seung Woo Lee, and Hyyong Suk. Highly-efficient 20 tw Ti:sapphire laser system using optimized diverging beams for laser wakefield acceleration experiments. *Current Applied Physics*, 15(4):468–472, 2015.

[17] Shigeki Tokita, Masaki Hashida, Shinichiro Masuno, Shin Namba, and Shuji Sakabe. 0.3% energy stability, 100-millijoule-class, Ti:sapphire chirped-pulse eight-pass amplification system. *Optics Express*, 16(19):14875–14881, 2008.

[18] Zhao Lei, Sui Zhan, Zhu Qi-Hua, Zhang Ying, and Zuo Yan-Lei. Design of rugate filter for gain narrowing compensation. *Acta Physica Sinica -Chinese Edition-*, 58:3977–3982, 2009.

[19] LQ Liu, HS Peng, XF Wei, QH Zhu, XJ Huang, XD Wang, KN Zhou, XM Zeng, X.-D Wang, Yiga Guo, Xiaodong Yuan, Zhi-Tian Peng, and XD Tang. Compensation of gain

narrowing by using aopdf in high-power ultra-short pulse laser systems. *Acta Physica Sinica -Chinese Edition-*, 54:2764–2768, 2005.

[20] Jihoon Jeong, Seryeyohan Cho, Seungjin Hwang, Bongju Lee, and Tae Jun Yu. Modeling and analysis of high-power ti:sapphire laser amplifiers–a review. *Applied Sciences*, 9(12), 2019.

[21] Joe ZH Yang and Barry C Walker. 0.09-terawatt pulses with a 31% efficient, kilohertz repetition-rate ti: sapphire regenerative amplifier. *Optics Letters*, 26(7):453–455, 2001.

[22] Vincent Leroux. *On the wavefront of ultrahigh intensity lasers: spatial contrast and gratings deformation.* PhD thesis, Staats-und Universitätsbibliothek Hamburg Carl von Ossietzky, 2018.

[23] Yuxing Han, Yunxia Jin, Fanyu Kong, Yonglu Wang, Yibin Zhang, Hongchao Cao, Yun Cui, and Jianda Shao. High-repetition-rate and multi-pulse ultrashort laser damage of gold-coated photoresist grating. *Applied Surface Science*, 576:151819, 2022.

[24] Ji Ping Zou, Hervé Coïc, and Dimitris Papadopoulos. Spatiotemporal coupling investigations for ti:sapphire-based multi-pw lasers. *High Power Laser Science and Engineering*, 10:e5, 2022.

[25] Tat Joo Teo and Alexander H Slocum. Principle of elastic averaging for rapid precision design. *Precision Engineering*, 49:146–159, 2017.

[26] KD Jamison and FB Dunning. Simple uhv offset manipulator with independent θ and φ rotations. *Review of scientific instruments*, 55(9):1509–1510, 1984.

[27] Christopher Arrell. Generation of few-cycle and attosecond pulses and their use in probing ultrafast dynamics in gases and surfaces. 2010.

[28] Ben C Platt and Roland Shack. History and principles of Shack-Hartmann wavefront sensing. *Journal of Refractive Surgery*, 17(5), 2001.

[29] R. G. Lane and M. Tallon. Wave-front reconstruction using a Shack–Hartmann sensor. *Appl. Opt.*, 31(32):6902–6908, 1992.

[30] Chih-Chieh Chen, Yi-Chang Lu, and Ming-Shing Su. Light field based digital refocusing using a DSLR camera with a pinhole array mask. 2010.

[31] Barbara Keitel, Elke Plönjes, Svea Kreis, Marion Kuhlmann, Kai Tiedtke, Tobias Mey, Bernd Schäfer, and Klaus Mann. Hartmann wavefront sensors and their application at flash. *Journal of Synchrotron Radiation*, 23(1):43–49, 2016.

[32] Sisi Zhou and Liang Jiang. Modern description of Rayleigh's criterion. *Phys. Rev. A*, 99:013808, 2019.

[33] Ethan Schonbrun, Adam R. Abate, Paul E. Steinvurzel, David. A. Weitz, and Kenneth B. Crozier. High-throughput fluorescence detection using an integrated zone-plate array. *Lab on a Chip*, 10(7):852, 2010.

[34] Aidan F. Brooks, Thu-Lan Kelly, Peter J. Veitch, and Jesper Munch. Ultra-sensitive wavefront measurement using a Hartmann sensor. *Opt. Express*, 15(16):10370–10375, 2007.

[35] Chen-Chun Kao and Albert J Shih. Form measurements of micro-holes. *Measurement Science and Technology*, 18(11):3603, 2007.

[36] Bing Li, Xiao Hong Liu, and Wen Jing Wu. Research of centroid extraction for feature point based on fpga. *Applied Mechanics and Materials*, 50:799–805, 2011.

[37] Zoran Krstic and Vladimir D Krstic. Silicon nitride: the engineering material of the future. *Journal of Materials Science*, 47:535–552, 2012.

Chapter 5

High repetition rate targetry

5.1 High repetition rate target diagnostics

High repetition rate target such as the tapedrive demonstrated by the author can be difficult to characterise and diagnose, in particular due to the high frequency content of power spectral density within the target positional jitter. Traditional methods such as using imaging camera running at high frame rate becomes prohibitively expensive when sampling rate required exceed 10 kHz [1].

5.1.1 White light confocal - CHROCODILE

White light confocal microscopy, such as the CHROCODILE system (Figure 5.1) from Precitec, takes advantage of chromatic aberration in its imaging probe. By dispersing light into different wavelengths, each wavelength focuses at a different depth. The system uses a fast read-out rate spectrometer to analyse the reflected light; reflection satisfying the confocal condition returns through the same beam pass with low loss, whereas reflections outside confocal depth region quickly diverges and become highly lossy. Determining the depth is based on the wavelength of maximum intensity, and therefore can be operated at very high frame-rate sustained by modern linear CCD. This method produces depth-resolved measurements of high-resolution 1D displacement without the necessity for mechanical scanning [2][3].

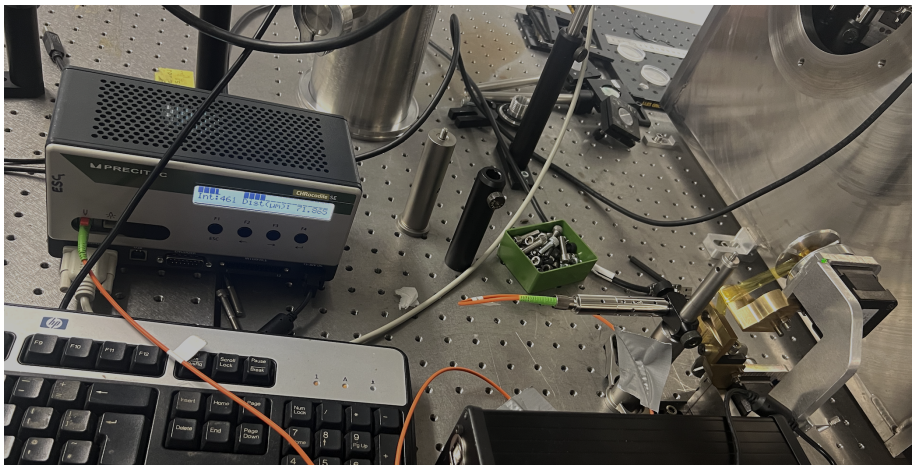


Figure 5.1: CHROCODILE white light confocal measurement setup

5.1.2 Heterodyne interferometry

Heterodyne interferometry is a distance metrology technique where two laser beams with slightly different frequencies interfere generated by a Zeeman-split dual line He-Ne laser cavity, or with an acousto-optical modulator, producing a beat frequency or heterodyne signal. The interference allows for determination of phase changes, translating into accurate measurements of displacement. The beat frequency, in the radio-frequency (RF) range, can be easily digitised and analysed with modern electronic instruments, enabling high-resolution and high-speed measurements. The method's strength lies in its capacity to offer very high resolution, long range linearity better than 10 picometer, at high refresh rate. However the system cost is higher than for a white light confocal probe [4][5][6].

5.2 Tapedrive

The author recently presented a comprehensive analysis and development of a tape-drive target system that produces regularly sub-micron positional stability, tailored for operations at 100 Hz [7]. This advanced tape-drive system was implemented in a high-intensity laser-plasma experimental setup (details in chapter 6). Within this context, it effectively accelerated proton beams to several MeV at frequencies reaching 5 Hz, a rate solely constrained by the operational capabilities of the accompanying laser.

5.2.1 Introduction to tape target

High-irradiance lasers with intensities greater than 10^{18} Wcm^{-2}, when interfaced with micron-scale target foils, are well-known to generate robust and directional proton beams, with energies reaching up to tens of MeV [8]. The acceleration of these protons is predominantly driven by the well-documented sheath acceleration mechanism [9] [10]. Such beams are particularly valuable for several uses. For instance, they are utilised in time-resolved deflectometry measurements to analyse electric and magnetic fields in dense plasmas [11]. Moreover, they can be used in the creation of medical isotopes [12], the exploration of radiobiology under high-dose rates pertinent to FLASH radiotherapy [13], and materials examination through proton-induced x-ray emission [14]. Notwithstanding their advantages, their wider implementation has been curtailed due to the low average flux, primarily stemming from laser shot rates that are often under 1 Hz.

Recent advancements in the realm of laser technology have brought forth joule-class lasers that operate at high repetition rates of at least 0.1 Hz [15, 16, 17, 18, 19, 20]. With these laser systems, it is now feasible to produce MeV proton beams at frequencies as high as 10 Hz. It is anticipated that imminent laser systems could possibly push this rate to 100 Hz [21] and even higher. A pressing concern now lies in the realm of target adaptation. Due to the destruction of target foils during the acceleration, there's an increasing demand to develop technology that can rapidly replenish these targets. Some contemporary solutions that have been tested in high-intensity laser plasma experiments encompass rastering foils [22], an assortment of cryogenic jets, planar ribbons [23][24], high-density gas jets [25], liquid micro-droplets, sheets [26], and liquid crystal film targets [27]. Among these, tape targets [28][29][30] stand out due to their cost-effectiveness and reduced intricacy when compared with liquid jet or foil targets. Additionally, they can readily supply targets with the necessary density to remain opaque during interaction, which is important for ion acceleration. The transparency of targets can influence the interaction and acceleration dynamics. Achieving vacuum compatibility both for the tape target drive system and the tape can be realised through material selection. Contrarily, maintaining optimal interaction chamber pressure with room temperature or cryogenic liquid jets typically demands specialised techniques like differential pumping or high-speed cryo-pumping [31].

Progressing towards the development of multi-Hz targetry for laser-driven proton acceleration introduces its own set of challenges. For instance, high repetition rate facilities are envisioned to operate continuously over extended duration, administering millions of shots, leading to a considerable consumption of target material. Given an average spacing of 2 mm between shots, a 10 Hz laser would exhaust a foil area surpassing 0.1 m^2/hr. This consumption rate restricts the use of raster targets, which rely on foils attached to grids or rotating disk turrets [32]. As an alternative, tape-drives can compactly supply fresh tape for thousands of shots, with one spool supplying and another removing the used tape. Achieving rapid target refresh rates, especially within a 10-millisecond cycle, remains a notable challenge, mainly attributed to the imperatives of stability and reproducibility in target positioning.

It is also worth noting that the peak particle energies derived from laser-solid interactions tend to scale with the laser intensity I_0 within a specific range ($I_0^{0.25} - I_0^{0.6}$ for sheath acceleration [33]). Therefore, achieving precise focusing is usually preferred. Given that this often results in a truncated Rayleigh length, usually under 10 μm, there is an inherent stringent tolerance for target positioning accuracy. Such intricacies mandate that the target delivery system possesses minimal intrinsic positioning jitter, even at high operational speeds. Furthermore, both the body of the tape drive and its link to mounting structures must exhibit steadfast stability, marked by minimal thermal drift and geometric deviations. Moreover, considering the prolonged operational durations, it is imperative to ensure rapid reloading of target materials with consistent repeatability. Utilising a typical 30m Kapton®tape roll, for example, could provide around 15,000 shots between reloads at a 2 mm spacing. Employing mechanisms like kinematic coupling for various target components or precision alignment dowels could help mitigate additional alignment challenges post target reloading or operations involving tape-drive repositioning within the interaction vacuum chamber.

5.2.2 Tape target design background

With the advent of advanced laser systems operating at high repetition rates between 100 Hz and 1 kHz, the generated pulses typically encompass energies less than 1 J. Consequently, the associated final laser focusing optic mandates an f-number of ≤ 3 to reach relativistic intensities.

This requirement equates to a diffraction-limited focal spot radius (at $1/e^2$) of approximately 1.5 µm and a Rayleigh range not exceeding 18 µm for a predominant wavelength of 800 nm. Consequently, a tape-drive target must ensure an RMS positional jitter below 5 µm. Additionally, to ensure consistent beam production over extended durations, a long-term structural thermal growth lesser than 2 µm relative to its mounting point is essential. Elevated thermal expansion, affecting the shape and position of the tape target surfaces, introduces complications in tape material selection and the structural design of the tape drive. Considerations must also account for stress release, blending specific machining techniques with heat treatments to guarantee geometric precision under thermal cycling and vibrations. Subsequent challenges including electromagnetic pulse resistance and radiation hardening of both the drive electronics and power source. These become important as the laser energy escalates. Typically, these constraints narrow down hardware options to those with space-rating, which can be often outdated. Yet, mitigation strategies for these challenges include specific circuit board layouts, feed-through electrical filtering, and supplementary shielding for the enclosure.

Other researchers have presented various tape-drive design strategies, such as incorporating plastic guide rollers coupled with spring tensioners that navigate tape around a structured aluminium plate, ensuring commendable short-term (10 s) positional stability of about 1 µm RMS when working alongside joule-class multi-Hz laser systems [34]. Nevertheless, this method might be ill-suited for elevated repetition rates due to the lag in feedback loop responses and superfluous complexity relative to open-loop schemes. More prevalent designs for high-repetition-rate tape-drives, operating around 10 Hz, deploy stationary guide pins primarily crafted from tungsten carbide with a polished surface finish or occasionally a cylindrical steel or stainless pin [35]. Such configurations frequently exhibit substantial surface positional errors and jitter, often surpassing 10 µm RMS. To our knowledge, no extensive thermal and structural drift evaluations of these high repetition rate tape-drives have been disseminated for durations exceeding 100 s.

The following sections will demonstrate the selection and integration of motors responsible for tape transfer between spools, in conjunction with the target frame, which emerges as a pivotal factor for sustaining long-term target stability.

5.2.3 Thermal considerations

5.2.4 Modal analysis and motor tuning

Through modal analysis, it becomes feasible to acquire domain-specific frequency information in response to varies excitations and compute resonance conditions. This approach also provide resonance frequencies with their associated quality factors, similar to the gain bandwidth in a laser cavity. Using Fusion 360's robust parametric modelling and its finite-element analysis toolkit, a series of modal analysis with finite element method were attempted. This was done on a simplified representation of the actual mass distribution to expedite computational turnaround. The resulting displacement of tape drive components for a example distinct resonance mode is shown in figure 5.2.

One should take precautionary measures to overcome the predominant 50 Hz excitation, typically associated with devices powered by the mains (and on rare instances, 60 Hz), and the 90 Hz frequency when incorporating contemporary dry roots pumps with an integrated variable frequency drive. The strategy was to bypass the vibrations originating from pumps and their harmonics, notably the second harmonic (100 Hz / 120 Hz / 180 Hz), achieved through a systematic design iteration complemented by finite element analysis. Additionally, it is crucial to avoid motor driver current modulation carrier frequencies, which are conventionally high enough not to produce problematic vibration modes but should still be avoided when feasible.

Vibrations induced by motor spooling, typically oscillating between 0.1 Hz and 10 Hz, and attributed to imbalances in the motor rotor and tape reel assembly, pose additional concerns. Such vibrations warrant rectification via dynamic balancing. In scenarios where disassembling commercial stepper motors for mechanical balancing is not feasible, one might use tape speed dithering techniques to introduce phase noise outside the resonance bandwidth. This refers to the deliberate introduction of noise with a specific power spectral density to counteract resonance.

Attention to these resonances during the design phase is essential in addressing target instabilities. Improving structural rigidity reduces the amplitude for given excitation, while also leveraging the material's inherent damping properties. The tape-drive mount design incorporated

a weight-reducing grid pattern, fine-tuning the structural response without significantly compromising its stiffness. Fabricating such an isogrid-pattern, characterised by intricate features and a high height to width aspect ratio, mandates advanced manufacturing techniques. This is to reduce unwanted machining-induced stress, potentially leading to micron-scale structural deformations over repetitive thermal and vibration cycles. While advanced solutions, like active dampening through an inertia reference unit equipped with a low angular random walk gyroscope and a dynamic range accelerometer, present potential benefits, their costs alone often exceed typical experimental budgets, thus rendering them beyond the scope of this discussion.

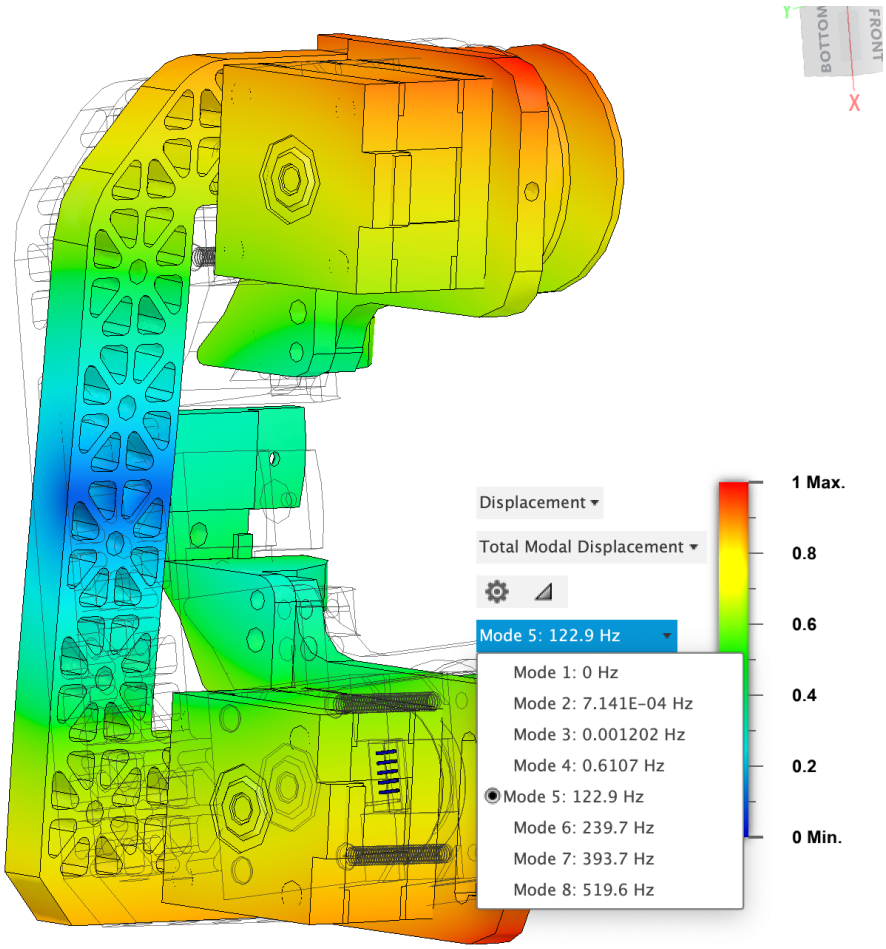


Figure 5.2: Modal Response of the Tape Drive at 122.9 Hz: A finite element analysis highlighting the displacement of tape drive components under resonant oscillations, fixed to a rigid breadboard. The associated structural resonant frequency modes are enumerated. A relative displacement amplitude is used as colour bar, normalised peak amplitude to 1.

Achieving complete vibrational isolation of the tape-drive remains difficult. Enhancing tape stability requires exploring mechanisms that strengthen the damping quality across the

entire target apparatus. This includes particularly the translation stages for adjusting target position within the chamber and the integrated tape-drive. Mechanisms ensuring fast vibration dissipation are crucial. Translation stages built on precision-ground or scraped hydrostatic guide-ways [36] offer a faster vibration dissipation rate than conventional ball or cross roller bearing linear rails. If budget constraints are not stringent, they should be used in conjunction with vacuum-compatible oil. Future enhancements in damping efficiency could potentially be realised with the integration of vacuum-compatible mixtures of epoxy and sand or alternative epoxy granite compositions [37].

5.2.5 Electronics for high repetition rate targetry

Commonly found in vacuum compatible precision motion systems, stepper motors stand distinct from brushed DC motors in their fundamental requirement for multi-phase driving. This necessitates the integration of at least one H-bridge, typically pulsed directly by a micro-controller I/O bank, though in many modern instances, the preference tilts towards a dedicated stepper driver chipset. Our selection of stepper drivers was informed by the burgeoning consumer indoor 3D-printing market. This expansive arena has catalysed the evolution and introduction of a myriad of low audible noise stepper drivers. Such advanced drivers enable a far superior approximation of sine wave phase current by employing a more precise sine-wave subdivision technique at a higher sample rate, in contrast to traditional stepper driver chipsets. Traditional stepper drivers, such as those based on the A4988 chipset, are known to generate and drive harmonic distortion along with modulation frequency-induced vibrations. This behaviour makes them less than ideal for applications requiring minimal jitter, particularly when one considers the rigid mounting of the motor to the tape-drive frame [38], without interfaces with point contact in low preload condition such as magnetically preloaded kinematic base.

Upon evaluation of various commercial off-the-shelf stepper motor micro-stepping application-specific integrated circuits (ASICs), choice was made to use the TMC2208 chipset. Several features drove this decision, notably its exceptional minimisation of drive waveform total harmonic distortion, its high sinusoidal pulse width modulation (SPWM) carrier frequency, and the commendable reduction in timing jitter-induced motor vibrations it provided. A careful

calibration with the stepper motor driver was optimised to function with the least drive current while preserving requisite torque, was adopted to mitigate overheating during spooling processes. A strategic choice was made to disable the DC holding mode; a mode which conventionally furnishes locking torque to prevent tape un-spooling when under tension. This further reduces motor heating. A conceivable trade-off here could be compromised stability during initial startup in scenarios of rapid torque changes. Nonetheless, the design of the iron core, exhibiting a pronounced cogging effect, delivers enough holding torque even in the absence of power. This ensures that the drive structure transitions seamlessly from a cold startup (retaining the previously established tape tension state) to its optimal operating condition within 0.1 s. Any abrupt impulse from start-up torque disparities are effectively minimised, ensuring that the tape-drive structure remains free from sudden strain, as illustrated in figure 5.3.

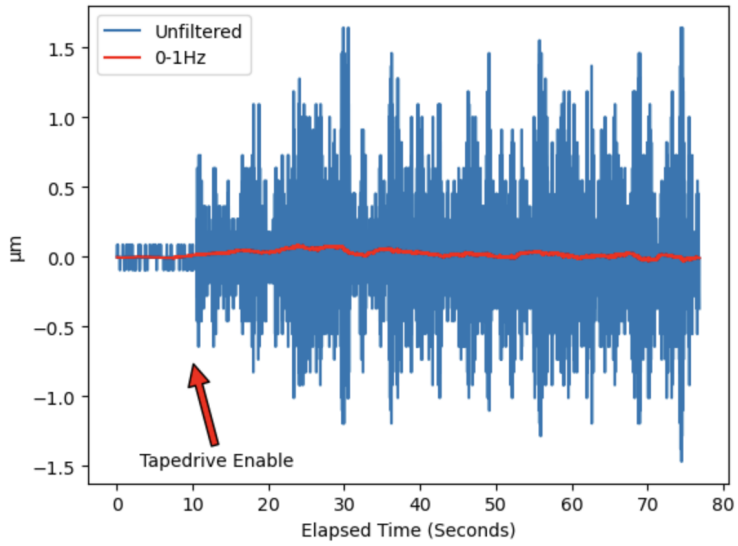


Figure 5.3: CHRocodile measured target tape vibrations during tape drive start-up, indicated by the red arrow. Background noise and intrinsic breadboard vibrations are evident before 10 seconds. After start-up, tape surface position is tracked for slightly over 1 minute. The entire measurement, sampled every 15 microseconds, is shown in blue, while a low-pass filtered signal with a 1 Hz cut-off illustrates long-term drift behavior.

5.2.6 Motor selection

In the field of precision motion control, the utilisation of closed-loop encoder feedback servo-motors has become ubiquitous. Modern servo-motors typically incorporate a brushless DC motor, integrated with a field-oriented control motor driver. Additionally, they utilise a

separate feedback loop facilitated by a realtime Digital Signal Processor (DSP) to enact encoder position feedback, ensuring consistent rotation speeds independent of load variations or external disturbances. A significant advantage of this system is its ability to operate in a constant torque feedback mode. This ensures consistent tape tension, even in the presence of variations in tape surface linear speed or tape material inconsistencies.

However, these systems are not without their limitations. Notably, the availability of ultra-high vacuum (UHV) compatible servo-motors forces many to use conventional motors. These standard motors often overheat, release vacuum contaminants contingent on material and lubricant choice, and undergo outgassing due to the trapped volumes within the sealed shaft optical encoder, which is challenging to adapt for vacuum compatibility. Furthermore, these commercial servo-motors are vulnerable to the levels of EMP and radiation typical near high-intensity laser-solid interactions. Such conditions can impair the encoder readout units due to EMP damage or compromise the motor winding insulation material through radiation damage, leading to electrical failures. The requirement for multiple differential signaling twisted pairs for effective electromagnetic interference rejection complicates their integration outside vacuum chambers. Some servo-motors, however, feature an in-built servo driver, simplifying electrical feedthrough, but often at the expense of overheating due to proximity to heat-generating motor winding in vacuum.

Parallelly, the motion control industry frequently employs hybrid stepper motors. Their ubiquity in semiconductor and aerospace industries has made them widely available, often boasting radiation hardening and UHV compatibility at economical prices. The intrinsic design of stepper motors, with their finer pole spacing relative to servo motors, allows for usable angular resolution in synchronous operation without encoder feedback (typically 0.9° or 1.8° based on the stepper type). For high-repetition-rate tape-drives, the requisite angular positioning resolution, approximately equivalent to 1 mm with standard drive spool diameters, is often influenced by factors like tape material inconsistency. Stepper motor drivers capable of microstepping can deliver the necessary angular resolution for seamless operation. However, due to these inherent material limitations, additional strategies, such as registration sprocket and fiducial markers, become imperative for repeatable absolute positioning across extensive tape lengths.

In contexts like commercial audio reproduction and data recording, brushed DC motors have traditionally served as pseudo-constant torque devices within tape-drive assemblies, both for driving and maintaining spool tension. At lower speeds, these motors, when driven by regulated DC sources, can adapt to fluctuating loads sans encoder feedback. Their robustness in torque control, even in EMP-rich environments, coupled with their lack of reliance on digital closed-loop feedback, makes them compelling. Yet, factors like graphite brush dust and other non-vacuum compatible attributes render them unsuitable for high-intensity laser-plasma experimental tape-drives.

After thorough examination of the commercial tape-drives discussed, the stepper motor emerged as the optimal choice, balancing affordability, simplicity in both implementation and interfacing, and adaptability for high-intensity laser-solid experiments operating up to 100 Hz in a vacuum setting.

5.2.7 Mechanical design and manufacturing

The connection between the manufacturing process and the stability of the tape-drive system is recognised. Delving into the nuances of manufacturing decisions, the heat treatment and handling of materials can lead to stress reactions. Over time, these can result in the tape drive's deformation. Given this, planning in manufacturing techniques are essential.

Specifically, low stress machining strategies with a lapped flute end-mill was chosen. This selection is driven by the need to minimise surface stress. Rubbing during machining processes can introduce substantial stress, potentially impacting the tape-drive's geometric stability as time progresses. Therefore, such strategies are vital to maintain the system's structural stability.

Vacuum-based applications bring additional complexities in material handling and processing. For applications that prioritise vacuum cleanliness, it is recommended to perform machining in a dry setting, without the use of cutting oils or water-soluble coolants. Yet, during particular machining processes, like deep pocket with high aspect ratio, this standard might be adjusted slightly. In these cases, a minimal quantity lubrication mist (MQL) of ethanol can be applied, effectively preventing chip welding while upholding vacuum requirements.

Furthermore, material considerations, such as the use of brass alloys containing zinc, come

with challenges. These alloys can have high vapour pressures at elevated temperatures, posing challenges for vacuum applications. However, it is essential to match material choices with specific application needs. For example, while laser-plasma particle accelerators operate around 1×10^{-6} mbar, this standard is less stringent than the ultra-high vacuum levels required by radio-frequency accelerators. Matching materials to the specific demands of each application is crucial for optimal performance and system longevity.

5.2.8 Review of characterising methods for tape-drive performance

Contact metrology methods, like dial test indicators, LVDT, and scanning CMM probes, are not ideal for thin, unsupported tape measurements. These tools can distort the tape's surface, hindering precise measurement, especially during dynamic tape spooling. Their bandwidth is further limited by the inertia of the probes.

Heterodyne interferometers, discussed previously, exemplified by the Renishaw XL-80, theoretically measure surface stability using direct surface reflection at 50 kHz without a retro-reflector cube. Their advantage lies in the potential long working distances (several metres) between the probe and the tape surface, allowing in-situ tape position diagnostics. This distance minimises interference with other diagnostics and ensures the durability of the optics under possible debris. Yet, the Renishaw XL-80, when tested from approximately 2 m away from the tape, faced signal-to-noise challenges due to tape properties such as transparency and poor surface quality. To address this, a high-power narrow line width fibre laser might serve as a better reference, though it has not been employed yet.

The Precitec CHRocodile, a confocal white light probe, offers high resolution, but its short working distance is unsuitable for most on-shot diagnostics. Despite its proximity risk to debris, for off-line stability checks, it performs well. Its quick update rate reaches 50 kHz, allowing comprehensive frequency domain analysis which assists in structural design feedback.

Direct off-axis imaging with long working-distance objectives offers flexibility, but standard scientific cameras fall short in frame rates, causing vibration diagnoses challenges. Comparatively, the imaging method underestimates vibrations compared to white light confocal probes. Advanced cameras with strobed illumination might mitigate these issues, but still, they may

provide inaccurate data due to sub-Nyquist sampling frequencies.

Optical CMM and MEMS atomic force microscope are precise but come with significant cost barriers. They're unsuitable for vacuum environments, with MEMS probes needing pressures near 1 bar. While they're not fit for in-situ tape stability measurements, they can evaluate surface roughness. As an example, the tape used in our demonstration was examined using microscopy and white light interferometry.

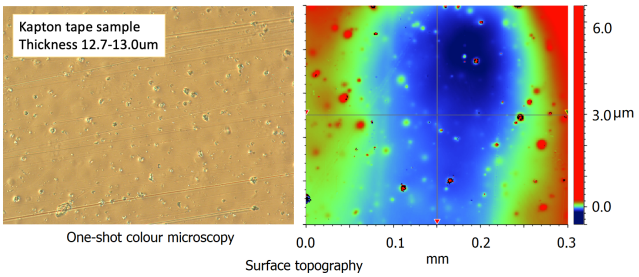


Figure 5.4: Optical profiling of the 12.7 μm Kapton tape through high magnification microscopy (left) and white light interferometry (right) reveals bubble defects visible as dark spots on the left. The right image's unevenness results from the tape being measured without tension. Figure previously published by author in 2023 [7].

In summary, in-situ tape measurements in high-intensity experiments are challenging due to spatial constraints. Nevertheless, accurate target positioning feedback is still important even with a highly stable tape drive. Without interferometer, an efficient solution might be using a high numerical aperture image relay to capture non-specularly scattered light. This method, while less accurate than CHRocodile measurements, was employed in our laser-plasma interaction studies, illustrating the need for continuous innovation in this domain.

5.2.9 Tape-drive performance in a real world laser–plasma interaction setup

A tape-drive system was engineered prioritising compactness, performance, and affordability. This initiative followed the insights derived from the preceding discussions. Notably, the choice of construction material prioritised longevity in a high vacuum environment, disregarding aspects like out-gassing or activation, owing to budgetary limits. The integration of stepper motors enabled the capability of remote-controlled spooling and rewinding. Moreover, programmable

tensioning was achieved using servo-operated brake shoe. To accommodate both prevalent tape widths of 12.7 mm and 25.4 mm, the drive's spool components were designed for fast interchangeability. Key to the tape's stability were two hand-crafted brass guide structures, supplemented by a central stabilising support plate. This plate not only augmented the tension on the tape but also offset the minor thickness inconsistencies often seen in lesser-quality tapes. With a modular design, these plates could be removed, granting enhanced access for diagnostic evaluations. Emphasis was also placed on ensuring that the tape supply and take-up wheel assembly's eccentricity aligned with the motor shaft, minimising stepper motor shaft runout. Such an alignment effectively mitigates structural deflections induced by torque ripple and rotation eccentricities.

For a comprehensive assessment of the tape drive's stability during its operation, the Precitec CHRocodile, a well-known white light system, was employed. Its impressive specifications include a noise threshold and a combined non-linearity less than 0.1 μm and an update rate of 66 kHz. The CHRocodile's probe, with a measurement span of 300 microns, averaged over a 2.5 μm diameter, furnishing detailed insights into the tape's rapid movements, inclusive of its surface intricacies.

The study assessed multiple materials like steel, copper, and Kapton across a range of thicknesses, from 12.7 μm to 50 μm. Notably, the steel tape's inherent elasticity meant it lacked a consistent flat profile, contrasting with the copper tape, whose surface anomalies affected data accuracy. However, Kapton tape emerged as the predominant choice for the demonstration trials, primarily due to the flexibility in thickness options and its compatibility with the driving laser pulses' low energies. While ultra-thin films like 10 μm Kapton or PET presented challenges in terms of target preparation and reliability, the 5 μm metal tape, comparable in strength to 12.7 μm Kapton tape, will be a good candidate for further experimentation. Detailed imaging techniques highlighted imperfections on these tapes' surfaces, such as bubbles and dents. These anomalies contributed to slight, rapid tape-drive position variations as they crossed the CHRocodile's observation zone. Detailed visual representations of these findings are accessible in figures 5.6 and 5.5. A preliminary analysis suggests the tape's movement remains under $< 2\,\mu$m, showing minimal thermal drift across extended operational periods. This pattern was

consistent even when the tape drive operated at variable linear spooling velocities, ranging between 2 - 256 mm/s. Comprehensive data on tape materials' performance under maximum noise conditions, specifically at 2 mm/s, can be found in Table 5.1 and Figure 5.5. It should be highlighted that at higher speeds, the tape drive showcases superior results.

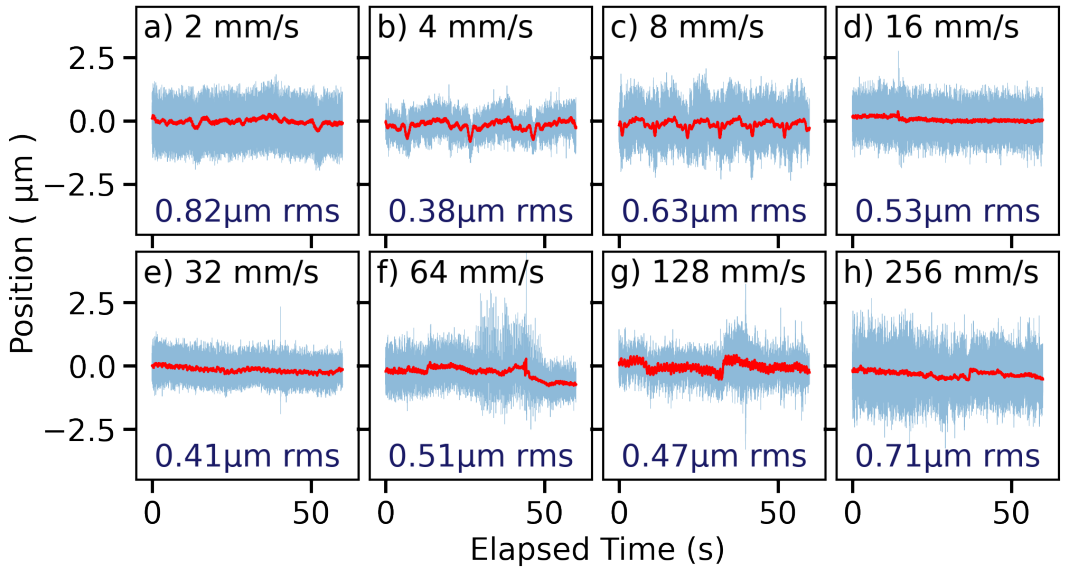


Figure 5.5: Using the Precitec CHRocodile, tape jitter was assessed over 1 minute at varying speeds. The red line depicts the tape's low-frequency (< 1 Hz) motion. RMS positional variation is specified in each subplot. In c), oscillations arise from the tape drive's resonance. Speeds exceeding 8 mm/s yield lower jitters because of diminished stepper motor resonances [39]. Stated tape speeds relate to the smallest motor setting and spool diameter (16 mm). As the spool's radius grows, speed can triple [7].

	Kapton 50 µm	Kapton 12 µm	Steel 20 µm	Copper 25 µm
RMS jitter (µm)	0.28	1.11	0.49	0.92
Pk-pk jitter (µm)	3.48	7.05	3.39	6.13

Table 5.1: Positional jitter for various tape materials. The 50 µm Kapton tape exhibited the best RMS performance at 0.28 µm. Limitations in surface quality samples restricted optimal tape-drive performance assessment. Previously published by author in 2023 [7].

Figure 5.6 shows the multi-material capability of the tapedrive. Material surface roughness can be seen in addition to the tape-drive jitter. Figure 5.7 demonstrated long term stability on the time scale of few hours.

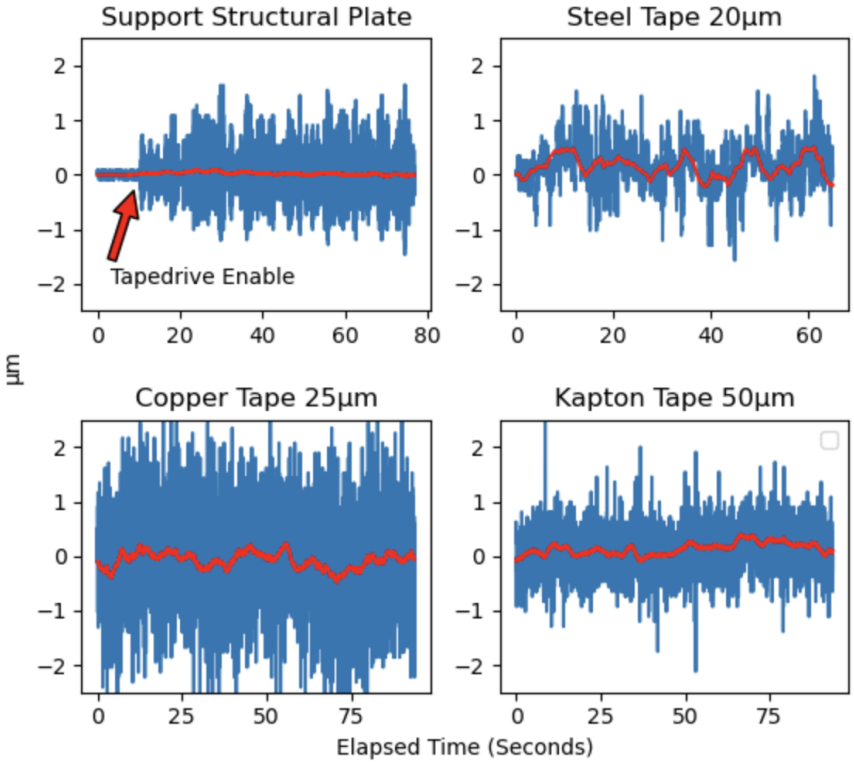


Figure 5.6: Tape jitter was measured with the Precitec CHRocodile over 1 minute at 2 mm/s. Except the top-left, all measurements targeted the laser interaction point. The top-left gauged the brass plate's stability. The red arrow marks the drive's activation. The blue line, sampled every 15 microseconds, shows surface roughness effects. The red line displays the tape's low-frequency (< 1 Hz) motion [7].

5.2.10 Experimental use of the developed tape target

The tape-drive was assessed at the Astra Gemini TA2 facility within the Rutherford Appleton Laboratory's Central Laser Facility [7]. A laser driver with intensities reaching 4×10^{19}W/cm^2 and an output of up to 400 mJ, operating at $1-5$ Hz repetition rate, was employed. This driver utilised a short focal length off-axis parabolic mirror ($f/2.5$) to focus on the target, generating MeV electron and proton beams, thereby testing the tape-drive in an intense EMP and radiation setting.

Electron beam energy spectra from the laser-tape interaction were determined using a

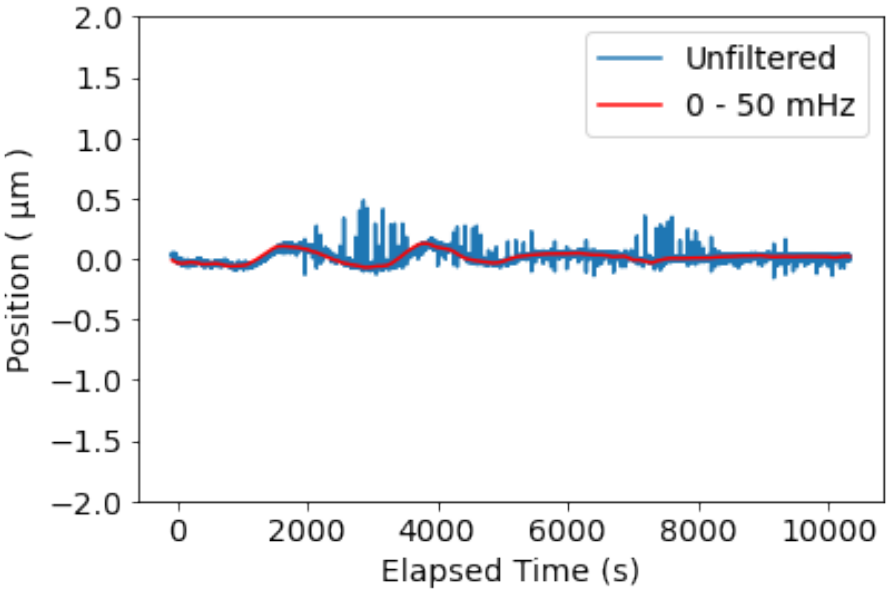


Figure 5.7: Using the Precitec CHRocodile, tape guide surface stability was evaluated at 125 mm/s, maximising potential thermal drift effects. The blue line shows measurements with a 0.2 s sampling period, capturing room vibrations. The red line reflects the tape-drive support's low-frequency (< 50 mHz) thermal drift, influenced by laboratory temperature fluctuations from the air conditioning loop [7].

150 mT permanent magnet spectrometer, paired with a Lanex screen detector placed 24 cm from the interaction site along the laser drive axis (as shown in figure 5.8). Proton profiles were analysed via a scintillator attuned to proton energies exceeding 1 MeV, while their spectrum was gauged using a time-of-flight diode near the target's rear surface-normal. The tape-drive was operated continuously, moving the tape roughly 2 mm between shots. Figure 5.8 shows the simplified experimental setup.

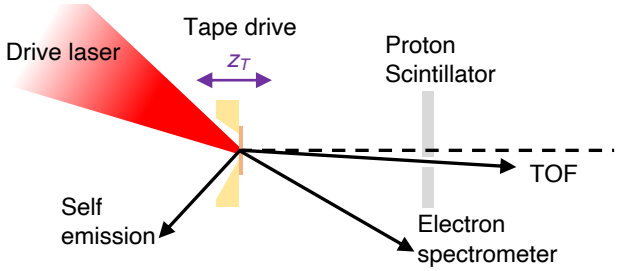


Figure 5.8: Experimental setup illustrates the target and diagnostics. The laser hit at 30° to the target normal, with the electron spectrometer capturing forward-accelerated electrons. The proton scintillator, aligned with the rear target-normal, had a centre hole for the TOF diode. The tape drive was movable along the target normal, employing an off-axis diagnostic for on-shot target plane positioning [7].

The tape-drive's position relative to the static laser focus was controlled using a motorised

XYZ stage. For these evaluations, 10 shots were recorded consecutively at a 1 Hz rate for each target position, after which the target was shifted to a different z position, aligned with the target surface normal. Given the laser's 30° angle of incidence, the mentioned z-distances are relative to 0.87 times the distance on the laser propagation axis.

Figure 5.10 illustrates the electron spectrum during a target position scan where the 50 μm thick Kapton tape target was moved in 10 μm increments along its surface normal. As the target neared optimal focus, both electron flux and peak energy grew rapidly due to increased laser intensities. This complete 140-shot scan was accomplished in about 5 minutes.

At the $z_T = 0$ target position, we observed a peak in both electron and proton flux and energy. The proton beam's spatial profile, accumulated over 10 shots, is depicted in Figure 5.9a. Figure 5.9b presents the distinct proton spectra from these shots, measured with a diamond detector in a Time-Of-Flight mode [40], alongside the burst's average spectrum. For individual shots, the diagnostic identified proton beam energies around a few MeV.

Given the short focal length of our OAP, target positional accuracy becomes sensitive. With a Rayleigh range of only 15 μm, precision is key. We gauged the z-position of the interaction plane during trials by imaging the 800 nm laser scatter from a 60° angle to the target normal, as shown in figure 5.8. By analysing the signal's centroid, we could determine the target plane z_T. Calibration of this diagnostic involved a non-damaging 800 nm continuous wave laser. Results showed a RMS jitter of 3.5 μm in the tape's target plane, against a 1.5 μm diagnostic resolution. However, this method, constrained by diagnostic resolution and plasma spatial distribution, is not as precise as the white light confocal approach. Still, it proved valuable for tracking tape position and spotting unforeseen shifts.

During our trials, the tape target withstood nearly 70,000 laser shots without noticeable differences in performance. This resilience suggests consistent tape-drive operation throughout. But, as days turned to weeks, debris accumulation became apparent. It did not affect the tape-drive during tests, but periodic beam-line optics cleaning and protective pellicle replacements became necessary, typically after 5,000-10,000 shots. The combination of debris and tight focusing presents challenges, especially with the tape target and optics near the debris source.

In conclusion, as reported in authors 2023 publication [7], a tape-drive target was devised

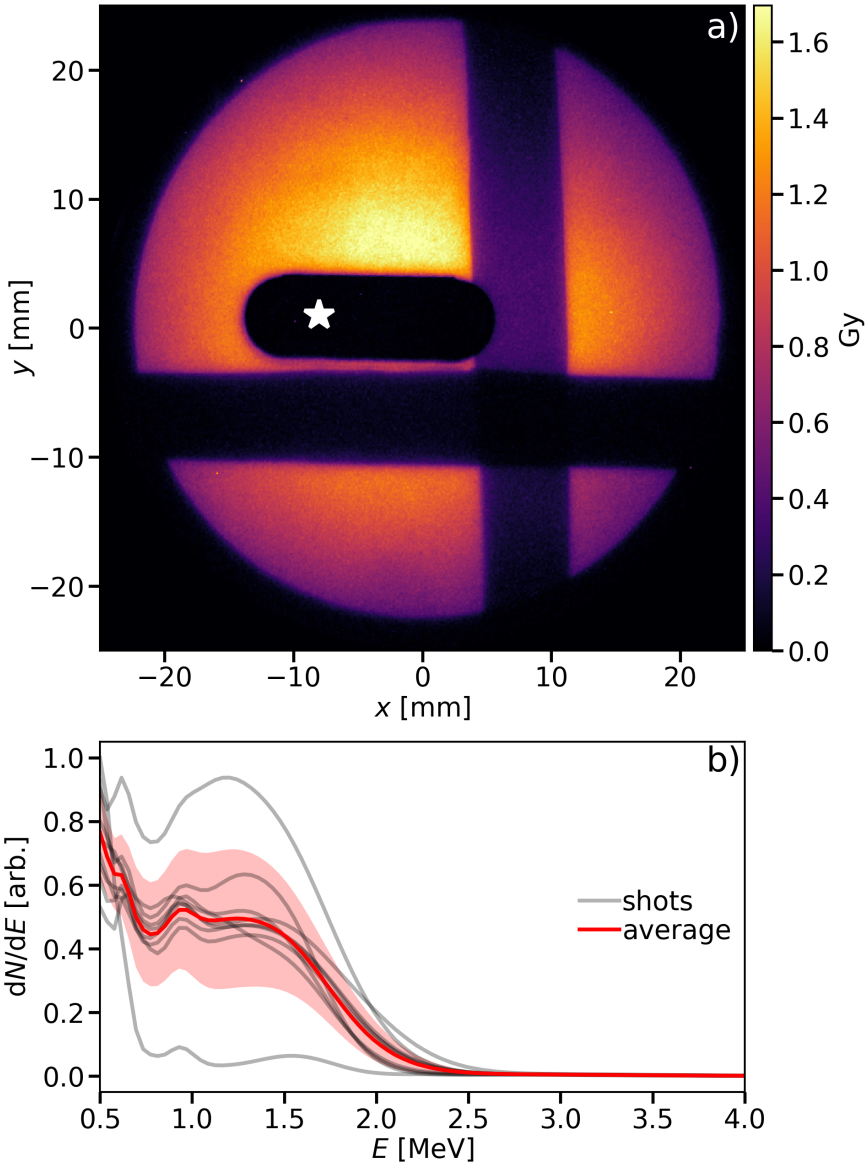


Figure 5.9: a) Proton average profile from ten shots on 50 μm Kapton tape at $z_T = 0$, captured using an EJ-440 scintillator 16 cm away. It was filtered with 6 μm aluminised Mylar. Dark stripes have additional aluminium filters, with a horizontal hole for rear diagnostics. The time-of-flight spectrometer's axis is marked by a white star. b) Proton spectra for each shot (grey), their mean (red line), and RMS (red shade) from a diamond-diode 36 cm away at 3°. Laser intensity fluctuated by 5%, but the laser-plasma interaction led to proton flux variations [7].

offering sub-micron RMS jitter, multi-material, multi-thickness, and variable speeds up to 100 Hz, based on in-depth stability analysis. This stability, under 100 Hz refresh for 1.5 minutes, was proven to be < 1 μm, limited only by the Kapton tape length. The system's efficacy was affirmed in a high-intensity laser-solid experiment, enduring over 70,000 shots with minor maintenance. Future enhancements envision miniaturisation, extended tape capacity, heightened vacuum

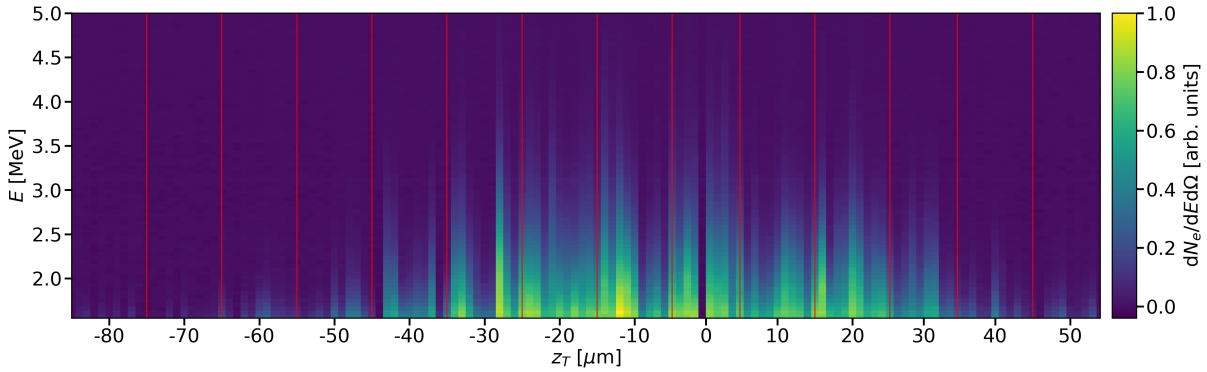


Figure 5.10: Waterfall plot displays the normalized forward electron spectrum from 50 μm Kapton tape, integrated over 35 μSr. Negative z values indicate laser pulse arrivals before its best focus on the tape. Each strip represents a single-shot spectrum at its z position, incremented by 10 μm across 10-shot bursts. Red lines delineate burst boundaries; shots at $z_T = 0$ align with those in Figure 5.9. Published previously by author [7].

adaptability, and EMP resilience. Testing with a 100 Hz laser will ensue upon accessibility.

More in-depth study of proton acceleration with this tape-drive target will be presented in chapter 6.

References

[1] I Prencipe, J Fuchs, S Pascarelli, DW Schumacher, RB Stephens, NB Alexander, R Briggs, M Büscher, MO Cernaianu, A Choukourov, et al. Targets for high repetition rate laser facilities: needs, challenges and perspectives. *High Power Laser Science and Engineering*, 2017.

[2] Aiko K Ruprecht, Klaus Koerner, Tobias F Wiesendanger, Hans J Tiziani, and Wolfgang Osten. Chromatic confocal detection for high-speed microtopography measurements. 5302:53–60, 2004.

[3] Peter Lucke, Arndt Last, Jurgen Mohr, Aiko K Ruprecht, Christof Pruss, Hans J Tiziani, Wolfgang Osten, Peter Lehmann, and Sven Schonfelder. Confocal micro-optical distance sensor: realization and results. 5856:136–142, 2005.

[4] NA Massie, RD Nelson, and S Holly. High-performance real-time heterodyne interferometry. *Applied Optics*, 18(11):1797–1803, 1979.

[5] Wenmei Hou and Günter Wilkening. Investigation and compensation of the nonlinearity of heterodyne interferometers. *Precision engineering*, 14(2):91–98, 1992.

[6] Christoph Weichert, Paul Köchert, Rainer Köning, J Flügge, B Andreas, U Kuetgens, and A Yacoot. A heterodyne interferometer with periodic nonlinearities smaller than±10 pm. *Measurement Science and Technology*, 23(9):094005, 2012.

[7] N Xu, MJV Streeter, OC Ettlinger, H Ahmed, S Astbury, M Borghesi, N Bourgeois, CB Curry, SJD Dann, NP Dover, et al. Versatile tape-drive target for high-repetition-rate laser-driven proton acceleration. *High Power Laser Science and Engineering*, 11:e23, 2023.

[8] Hiroyuki Daido, Mamiko Nishiuchi, and Alexander S Pirozhkov. Review of laser-driven ion sources and their applications. *Reports on Progress in Physics*, 75(5), 2012.

[9] E. L. Clark, K. Krushelnick, M. Zepf, F. N. Beg, M. Tatarakis, A. Machacek, M. I. K. Santala, I. Watts, P. A. Norreys, and A. E. Dangor. Energetic heavy-ion and proton

generation from ultraintense laser-plasma interactions with solids. *Phys. Rev. Lett.*, 85:1654–1657, 2000.

[10] S. C. Wilks, a. B. Langdon, T. E. Cowan, M. Roth, M. Singh, S. Hatchett, M. H. Key, D. Pennington, A. J. Mackinnon, and R. A. Snavely. Energetic proton generation in ultra-intense laser–solid interactions. *Physics of Plasmas*, 8(2):542, 2001.

[11] M. Borghesi, S. V. Bulanov, T. Zh. Esirkepov, S. Fritzler, S. Kar, T. V. Liseikina, V. Malka, F. Pegoraro, L. Romagnani, J. P. Rousseau, A. Schiavi, O. Willi, and A. V. Zayats. Plasma ion evolution in the wake of a high-intensity ultrashort laser pulse. *Phys. Rev. Lett.*, 94:195003, 2005.

[12] S. Fritzler, V. Malka, G. Grillon, J. P. Rousseau, F. Burgy, E. Lefebvre, E. d'Humières, P. McKenna, and K. W. D. Ledingham. Proton beams generated with high-intensity lasers: Applications to medical isotope production. *Applied Physics Letters*, 83(15):3039–3041, 2003.

[13] Marie-Catherine Vozenin, Jean Bourhis, and Marco Durante. Towards clinical translation of flash radiotherapy. *Nature reviews. Clinical oncology*, 2022.

[14] Pilar Puyuelo-Valdes, Simon Vallières, Martina Salvadori, Sylvain Fourmaux, Stephane Payeur, Jean-Claude Kieffer, Fazia Hannachi, and Patrizio Antici. Combined laser-based x-ray fluorescence and particle-induced x-ray emission for versatile multi-element analysis. *Scientific Reports*, 11(1), 2021.

[15] Jae Hee Sung, Jin Woo Yoon, Il Woo Choi, Seong Ku Lee, Hwang Woon Lee, Jeong Moon Yang, Yeong Gyu Kim, and Chang Hee Nam. 5-hz, 150-tw ti:sapphire laser with high spatiotemporal quality. *Journal of the Korean Physical Society*, 77(3):223–228, 2020.

[16] A. X. Li, C. Y. Qin, H. Zhang, S. Li, L. L. Fan, Q. S. Wang, T. J. Xu, N. W. Wang, L. H. Yu, and Y. Xu. Acceleration of 60 mev proton beams in the commissioning experiment of the sulf-10 pw laser. *High Power Laser Science and Engineering*, 10:e26, 2022.

[17] K Zeil, S D Kraft, S Bock, M Bussmann, T E Cowan, T Kluge, J Metzkes, T Richter, R Sauerbrey, and U Schramm. The scaling of proton energies in ultrashort pulse laser plasma acceleration. *New Journal of Physics*, 12(4):045015, 2010.

[18] K. Nakamura, H.-S. Mao, A. J. Gonsalves, H. Vincenti, D. E. Mittelberger, J. Daniels, A. Magana, C. Toth, and W. P. Leemans. Diagnostics, control and performance parameters for the bella high repetition rate petawatt class laser. *IEEE Journal of Quantum Electronics*, 53(4):1–21, 2017.

[19] S. Borneis, T. Laštovička, M. Sokol, T.-M. Jeong, F. Condamine, O. Renner, V. Tikhonchuk, H. Bohlin, A. Fajstavr, J.-C. Hernandez, and et al. Design, installation and commissioning of the eli-beamlines high-power, high-repetition rate hapls laser beam transport system to p3. *High Power Laser Science and Engineering*, 9:e30, 2021.

[20] L. Volpe, R. Fedosejevs, G. Gatti, J. A. Pérez-Hernández, C. Méndez, J. Apiñaniz, X. Vaisseau, C. Salgado, M. Huault, and S. Malko. Generation of high energy laser-driven electron and proton sources with the 200 tw system vega 2 at the centro de laseres pulsados. *High Power Laser Science and Engineering*, 7:e25, 2019.

[21] Roberto Lera, Pablo Bellido, Isabel Sanchez, Paula Mur, Michael Seimetz, Jose Maria Benlloch, Luis Roso, and Alexandro Ruiz-de-la Cruz. Development of a few tw ti:sa laser system at 100 hz for proton acceleration. *Applied Physics B*, 125(1), 2018.

[22] C Spindloe, G Arthur, F Hall, S Tomlinson, R Potter, S Kar, J Green, A Higginbotham, N. Booth, and M K Tolley. High volume fabrication of laser targets using MEMS techniques. *Journal of Physics: Conference Series*, 713:012002, 2016.

[23] Lieselotte Obst, Sebastian Göde, Martin Rehwald, Florian-Emanuel Brack, João Branco, Stefan Bock, Michael Bussmann, Thomas E. Cowan, Chandra B. Curry, Frederico Fiuza, Maxence Gauthier, René Gebhardt, Uwe Helbig, Axel Huebl, Uwe Hübner, Arie Irman, Lev Kazak, Jongjin B. Kim, Thomas Kluge, Stephan Kraft, Markus Loeser, Josefine Metzkes, Rohini Mishra, Christian Rödel, Hans-Peter Schlenvoigt, Mathias Siebold, Josef Tiggesbäumker, Steffen Wolter, Tim Ziegler, Ulrich Schramm, Siegfried H. Glenzer, and

Karl Zeil. Efficient laser-driven proton acceleration from cylindrical and planar cryogenic hydrogen jets. *Scientific Reports*, 7(1):10248, 2017.

[24] Chandra B. Curry, Christopher Schoenwaelder, Sebastian Goede, Jongjin B. Kim, Martin Rehwald, Franziska Treffert, Karl Zeil, Siegfried H. Glenzer, and Maxence Gauthier. Cryogenic liquid jets for high repetition rate discovery science. *Journal of Visualized Experiments*, (159), 2020.

[25] P. Puyuelo-Valdes, J-L. Henares, F. Hannachi, T. Ceccotti, J. Domange, M. Ehret, E. D'Humieres, L. Lancia, J-R. Marquès, J. Santos, and M. Tarisien. Laser driven ion acceleration in high-density gas jets. In Eric Esarey, Carl B. Schroeder, and Jörg Schreiber, editors, *Laser Acceleration of Electrons, Protons, and Ions V*, volume 11037, page 110370B. International Society for Optics and Photonics, SPIE, 2019.

[26] K. M. George, J. T. Morrison, S. Feister, G. K. Ngirmang, J. R. Smith, A. J. Klim, J. Snyder, D. Austin, W. Erbsen, K. D. Frische, J. Nees, C. Orban, E. A. Chowdhury, and W. M. Roquemore. High-repetition-rate (kHz) targets and optics from liquid microjets for high-intensity laser-plasma interactions. *High Power Laser Science and Engineering*, 7:e50, 2019.

[27] P L Poole, L Obst, G E Cochran, J Metzkes, H-P Schlenvoigt, I Prencipe, T Kluge, T Cowan, U Schramm, D W Schumacher, and et al. Laser-driven ion acceleration via target normal sheath acceleration in the relativistic transparency regime. *New Journal of Physics*, 20(1):013019, 2018.

[28] Steven J. Haney, Kurt W. Berger, Glenn D. Kubiak, Paul D. Rockett, and John Hunter. Prototype high-speed tape target transport for a laser plasma soft-x-ray projection lithography source. *Appl. Opt.*, 32(34):6934–6937, 1993.

[29] E. Fill, J. Bayerl, and R. Tommasini. A novel tape target for use with repetitively pulsed lasers. *Review of Scientific Instruments*, 73(5):2190–2192, 2002.

[30] Takuya Nayuki, Yuji Oishi, Takashi Fujii, Koshichi Nemoto, Tsutomu Kayoiji, Yasuaki Okano, Yoichiro Hironaka, Kazutaka G. Nakamura, Ken-ichi Kondo, Ken-ichi Ueda, and

et al. Thin tape target driver for laser ion accelerator. *Review of Scientific Instruments*, 74(7):3293–3296, 2003.

[31] Joseph Snyder, John Morrison, Scott Feister, Kyle Frische, Kevin George, Manh Le, Christopher Orban, Gregory Ngirmang, Enam Chowdhury, and William Roquemore. Background pressure effects on MeV protons accelerated via relativistically intense laser-plasma interactions. *Scientific Reports*, 10(1):18245, 2020.

[32] Ying Gao, Jianhui Bin, Daniel Haffa, Christian Kreuzer, Jens Hartmann, Martin Speicher, Florian H. Lindner, Tobias M. Ostermayr, Peter Hilz, and Thomas F. et al. Rösch. An automated, 0.5 hz nano-foil target positioning system for intense laser plasma experiments. *High Power Laser Science and Engineering*, 5, 2017.

[33] N. P. Dover, M. Nishiuchi, H. Sakaki, Ko. Kondo, M. A. Alkhimova, A. Ya. Faenov, M. Hata, N. Iwata, H. Kiriyama, and J. K. et al. Koga. Effect of small focus on electron heating and proton acceleration in ultrarelativistic laser-solid interactions. *Physical Review Letters*, 124(8), 2020.

[34] *Progression of a tape-drive targetry solution for high rep-rate HPL experiments within the CLF.* 2022.

[35] Muhammad Noaman-ul Haq, Hamad Ahmed, Thomas Sokollik, Lule Yu, Zezhou Liu, Xiaohui Yuan, Fang Yuan, Mohammad Mirzaie, Xulei Ge, and Liming et al. Chen. Statistical analysis of laser driven protons using a high-repetition-rate tape drive target system. *Physical Review Accelerators and Beams*, 20(4), 2017.

[36] M. Fritz and M. Groeb. Increasing performance and energy efficency of a machine tool through hydrostatic linear guideways with single digit micrometre fluid film thickness. *MM Science Journal*, 2021(5):5241–5246, 2021.

[37] Benjamin B Lazan. *Damping of materials and members in structural mechanics.* Pergamon Press, 1968.

[38] M. A. Vernezi, D. V. Nazarenko, and E. H. Abderrazzak. Vibration suppression of stepper motors by the electric method. In *2021 International Conference on Industrial Engineering, Applications and Manufacturing (ICIEAM)*, pages 566–570, 2021.

[39] Kenneth Wang-Hay Tsui, Norbert Chow Cheung, and Kadett Chi-Wah Yuen. Novel modeling and damping technique for hybrid stepper motor. *IEEE Transactions on Industrial Electronics*, 56(1):202–211, 2009.

[40] D. Margarone, J. Krása, L. Giuffrida, A. Picciotto, L. Torrisi, T. Nowak, P. Musumeci, A. Velyhan, J. Prokůpek, L. Láska, and et al. Full characterization of laser-accelerated ion beams using faraday cup, silicon carbide, and single-crystal diamond detectors. *Journal of Applied Physics*, 109(10), 2011.

Chapter 6

High repetition rate ion sources and diagnostics

6.1 Brief review of experimental results at high repetition rate

High-intensity lasers have the capability to produce energetic ions with very high particle numbers [1]. However, a prevalent challenge is their low repetition rate. For many applications, consistent and repeatable results are required, making this limitation a significant concern. To optimise ion generation, short pulse lasers when focused tightly, can interact with targets, achieving the right normalised vector potential conditions for ion acceleration.

There are a few reports of proton acceleration using millijoule-class short-pulse laser system of repetition rate higher than 10 Hz. In an experiment by Morrison et al. [2], a 5 mJ laser was used to produce intensity close to $5 \times 10^{18}\,\mathrm{W\,cm^{-2}}$ onto liquid ethylene glycol liquid sheet target, generating proton energies up to 2 MeV, at kHz repetition rate. A 3 mJ laser operating at 500 Hz was used by Hou et al. [3] in generating 265 keV well collimated protons at an intensity of $3 \times 10^{19}\,\mathrm{W/cm^2}$ onto bulk glass target. A statistical analysis of a high repetition rate laser driven ion source was performed at 6 MeV and showed the variation to be less than 5% [4]. Higher energy results from relatively higher laser energy but a lower repetition rate of 0.5 Hz was published recently [5].

6.2 Experimental setup

As discussed previously in Chapter 5, a tapedrive has been developed to enable ion acceleration at repetition rates above 100 Hz. An experiment utilising the tapedrive was conducted, in part to provide guidance for high repetition rate operation with the laser detailed in chapter 4. The Astra Gemini TA2 facility within the Rutherford Appleton Laboratory's Central Laser Facility provided a laser driver with an output of up to 400 mJ at 40 fs, operating at $1-5$ Hz repetition rate. This driver uses an off-axis parabolic mirror ($f/2.5$) to focus on the target, generating MeV electron and proton beams.

Figure 6.1 shows the interaction critical optics and diagnostics layout. The laser hit at 30° to the target normal, with the electron spectrometer capturing forward-accelerated electrons. The proton scintillator, aligned with the rear target-normal, had a centre hole for the ToF diode. The tape drive was movable along the target normal, employing an off-axis diagnostic for on-shot target plane positioning.

To the right of Figure 6.1, adjacent to the gate valve from the adaptive optic chamber, a set of motorised retarders is depicted. These were employed to manipulate the polarisation of the drive laser. Figure 6.2 presents a diagnostic diagram used for calibrating the drive beam's polarisation, in conjunction with the motorised quarter-wave and half-wave thin mica retarders, positioned beside a differential pumping window. The differential pumping window safeguard both the vacuum compressor and adaptive optic from organic vapours emitted from the interaction area.

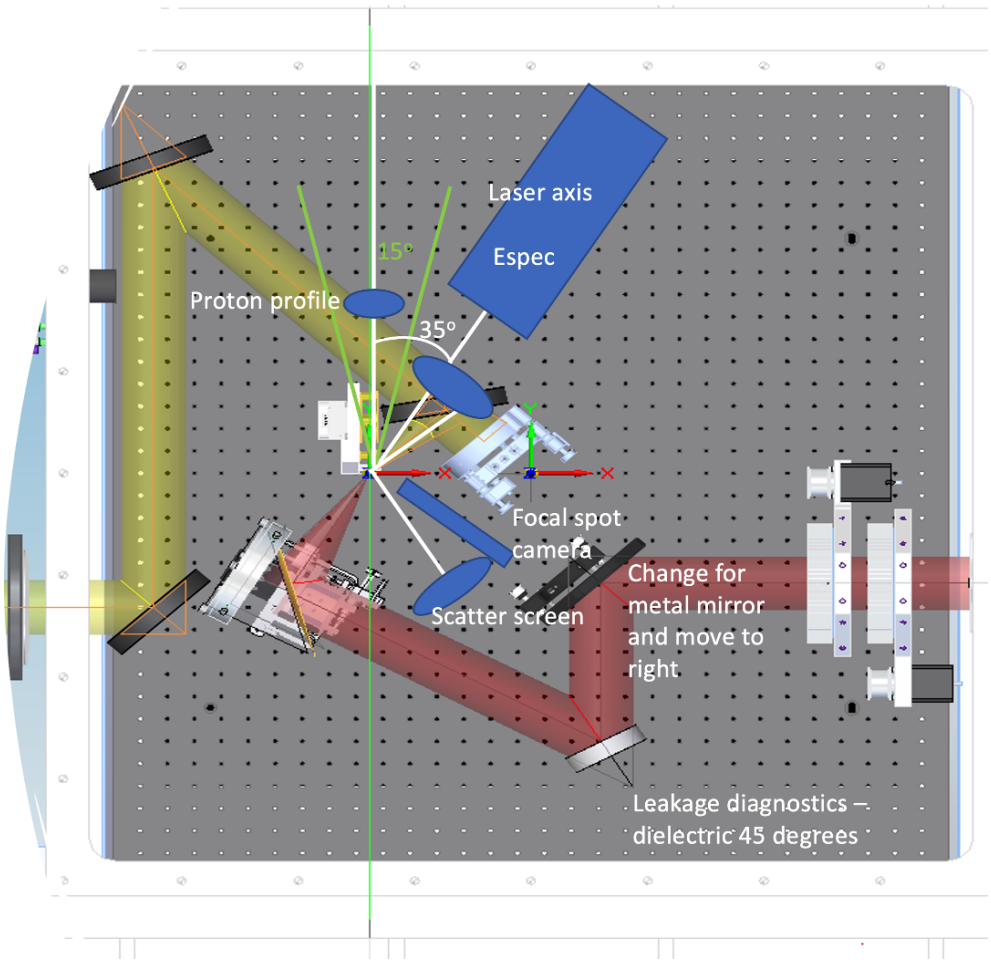


Figure 6.1: Experimental setup in 3D drawing [6].

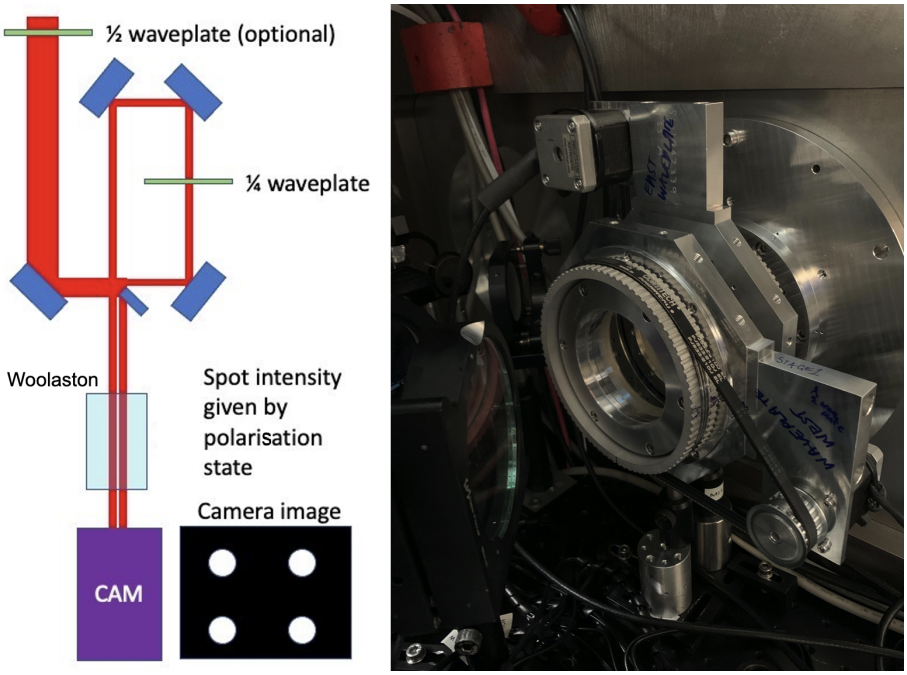


Figure 6.2: Experimental setup for manipulating polarisation [6].

Figure 6.3 shows the tape target and focal spot alignment objective. A long working distance infinity corrected objective was used in conjunction with a 45 degree steering mirror to have diagnostic access without physically interfering with other optics. This objective was also used for OAP optimisation, laser focusing, as well as target positioning offline. The objective was not corrected for chromatic aberration apart from visible wavelengths, therefore a focus shift with white light illumination of target surface was anticipated compared to 800 nm laser focal spot. This was minimised by using a diode laser illumination source close to 800 nm wavelength.

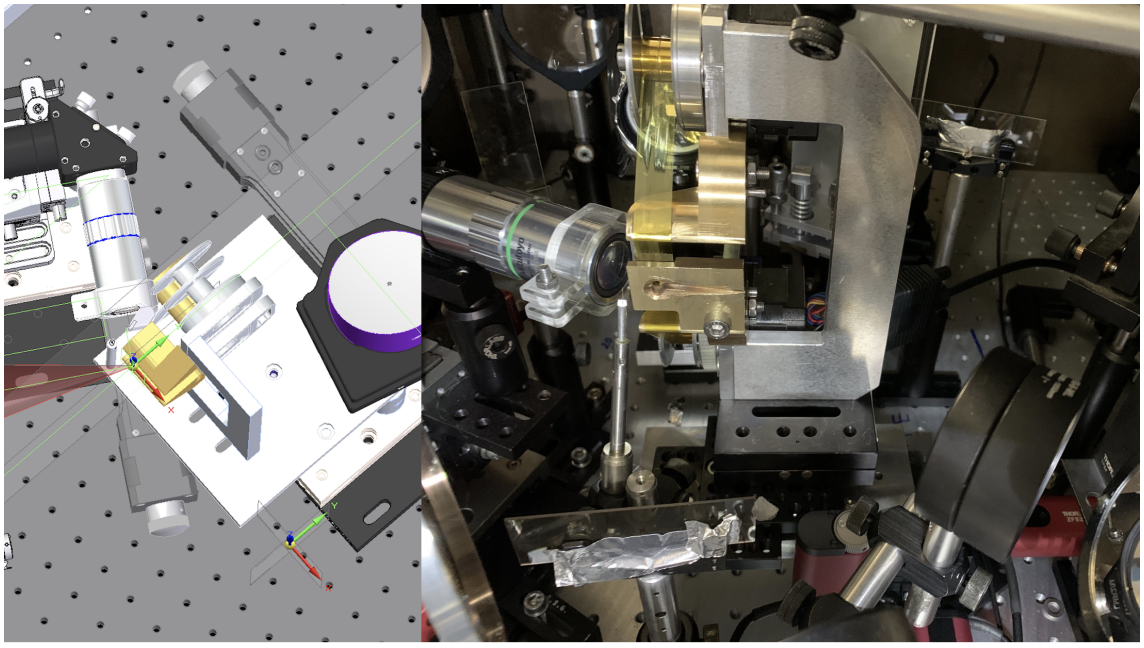


Figure 6.3: Experimental setup in 3D drawing and still image captured during experiment [6].

Figure 6.4 shows the measured focal spot at best focus, $\frac{1}{e^2}$ size of 1.56 by 1.75 micron, with normalised vector potential $a_0 = 3.73 \pm 0.28$ assuming a 250 mJ laser pulse at 40 fs. Focal spot image was captured at low laser energy with a calibrated microscope objective and ND filters (layers of scattering lens tissues).

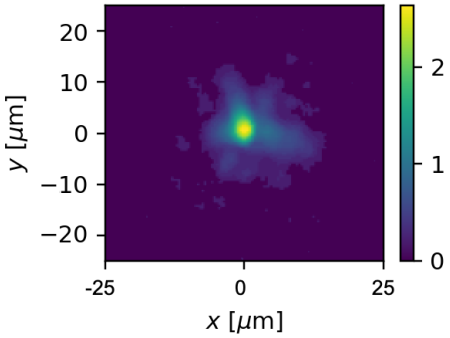


Figure 6.4: Focal spot intensity distribution.

6.3 High repetition rate ion diagnostic methods

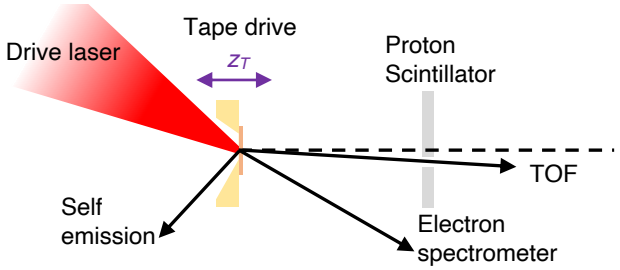


Figure 6.5: Experimental setup illustrates the diagnostic layout [6].

Electron beam energy spectra from the laser-tape interaction were determined using a 150 mT permanent magnet spectrometer, paired with a Lanex screen detector placed 24 cm from the interaction site along the laser drive axis (as shown in figure 6.5). Proton spectrum was mainly measured using a time-of-flight diode near the target's rear surface-normal.

The Thomson Parabola [7] is an ion spectrometer used for analysing the energy and charge states of ions generated in laser-plasma interactions. It employs simultaneous magnetic and electric fields to separate ions in a two-dimensional screen based on their charge-to-mass ratio and energy. In this setup, ions of the same charge-to-mass ratio but different energies follow parabolic trajectories, creating distinct parabolic traces for each ion species on a detector screen. The layout provides a compact way to perform simultaneous multi-species ion spectroscopy. Combined with the use of a fast recovery scintillation screen and a high frame rate camera, or sometimes with the addition of a multichannel plate [8], these detectors can be digitally read in near real time at high repetition rate.

A Time-of-Flight (ToF) spectrometer with a Faraday cup [9] [10] or diamond detector [11]

can be used to measure ion energy by capturing ions and measuring the time they take to travel a known distance. Ions are generated by the laser-plasma interactions and travel down a drift tube toward the detector. The Faraday cup collects ions and measures current to determine particle count, while the diamond detector can provide additional data such as energy resolution given low enough ion counts and a statistical capability with a high repetition rate laser. By knowing the drift distance and measuring the arrival time, the energy of the ions can be calculated. This setup is simpler than a Thomson Parabola but often offers no charge-to-mass information due to lack of repetition rate to acquire meaningful statistical data from single event detection. These detectors can be read out by custom ADC and FPGA capturing electronics, to achieve high repetition rate. While commonly used in conjunction with ToF spectrometers, oscilloscopes are limited by their architecture in providing continuous high repetition rate sampling.

6.4 Time-of-flight data and artifact mitigation

The time-of-flight detector was a Cividec high-radiation beam-loss diamond detector placed 35 cm from the interaction point. The detector is a customised model sCVD with 140 µm thickness, 4.5×4.5 mm with 100% charge efficiency, and a 1 mm diameter alpha calibration window with an internal attenuator. Data capturing was performed with a commercial oscilloscope (LeCroy 813Zi-B, 40 Gsps, 13 GHz 3dB bandwidth). However the detector was connected through BNC to SMA adaptor, as well as using an external 50 ohm BNC terminator and attenuator to protect the analogue front-end of the oscilloscope from EMP damage. This has a significant impact on signal integrity. A non-precision BNC connector or adaptor can have significant impedance mismatch during its transition between different diameters. A propagating electrical impulse can bounce back and forth between different impedance mismatch points, creating messy time-domain results without de-embedding.

As a result, the initial x-ray flash, an impulse before any proton signal is seen which is as short as the time constant of the RC condition for the detector, can create lots of ripples at seemingly random delays and random amplitudes. These ripples can overlap the real proton signals, providing or hiding features of the proton spectra. In principle this train of ripples can be

fully characterised with a vector network analyser (VNA). Time Domain Reflectometry (TDR) data is derived from the inverse Fourier transform of the frequency domain's S11 parameter from the VNA. This principle is rooted in the relationship between a system's impulse and frequency responses [12]. However, this assumes the complete setup of cables and adaptors remains unchanged, while also using phase stabilised coaxial cables, which is typically not the case due to budget. In practice, the phase delay versus frequency is always changing with commonly available BNC cables. Therefore a pre-calibrated reflection map will change through the experimental period. In Figure 6.6, the ripples can be seen overlapping the actual weak proton data from a typical shot.

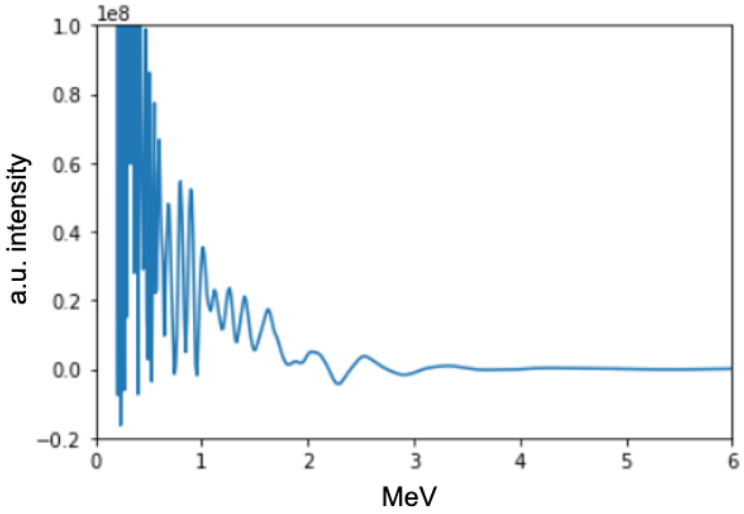


Figure 6.6: Proton energy data captured with cable and connector induced reflections. Ripples can be observed resulting from the non-flat frequency response of the system with some contribution from the EMP.

In order to filter out the majority of the high frequency fundamentals, a sacrifice in temporal resolution was made, Figure 6.7 shows comparison between commonly used moving average filtering, and a finite impulse response (FTR) low-pass filter. This can be easily implemented in FPGA with a real-time pipeline.

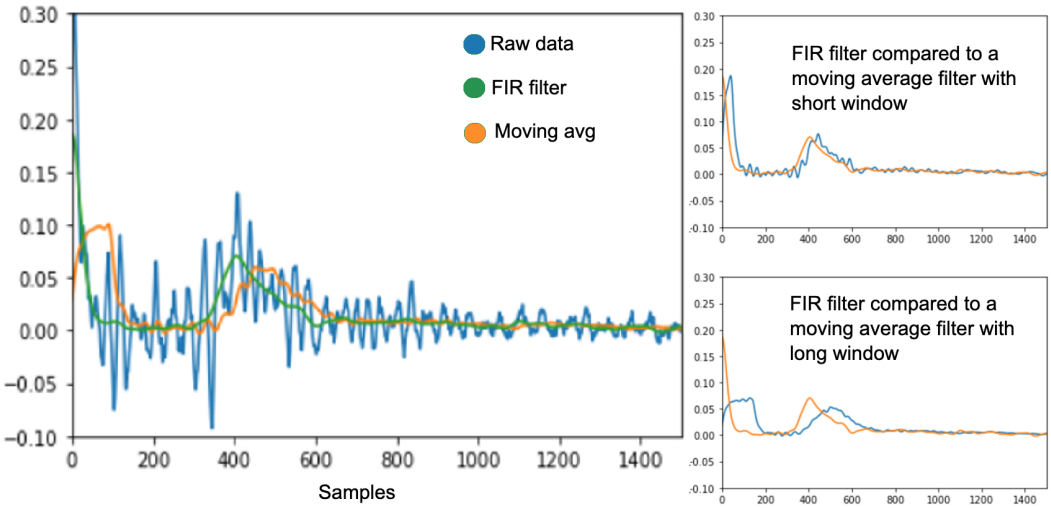


Figure 6.7: Comparison on loss of temporal details and efficiency on removing broadband interference with no spectral features for rolling average filter and FIR low-pass filter with different chosen parameter. The FIR filter maintains more high frequency information and higher signal fidelity while removing more ripples.

With the EMP filtered, as shown in Figure 6.8 and Figure 6.9, there are a train of ripples from the x-ray flash. This can be seen sometimes overlapping the proton data. As the x-ray is more stable, relatively unaffected by the target and laser conditions, the resulting artefacts present themselves as stable bands at fixed delays, in contrast to the unstable proton spectrum. Due to the non-linear relationship between proton energy, the ToF delay, and the quantum efficiency calibration, this was exaggerated further when converted to a proton energy axis.

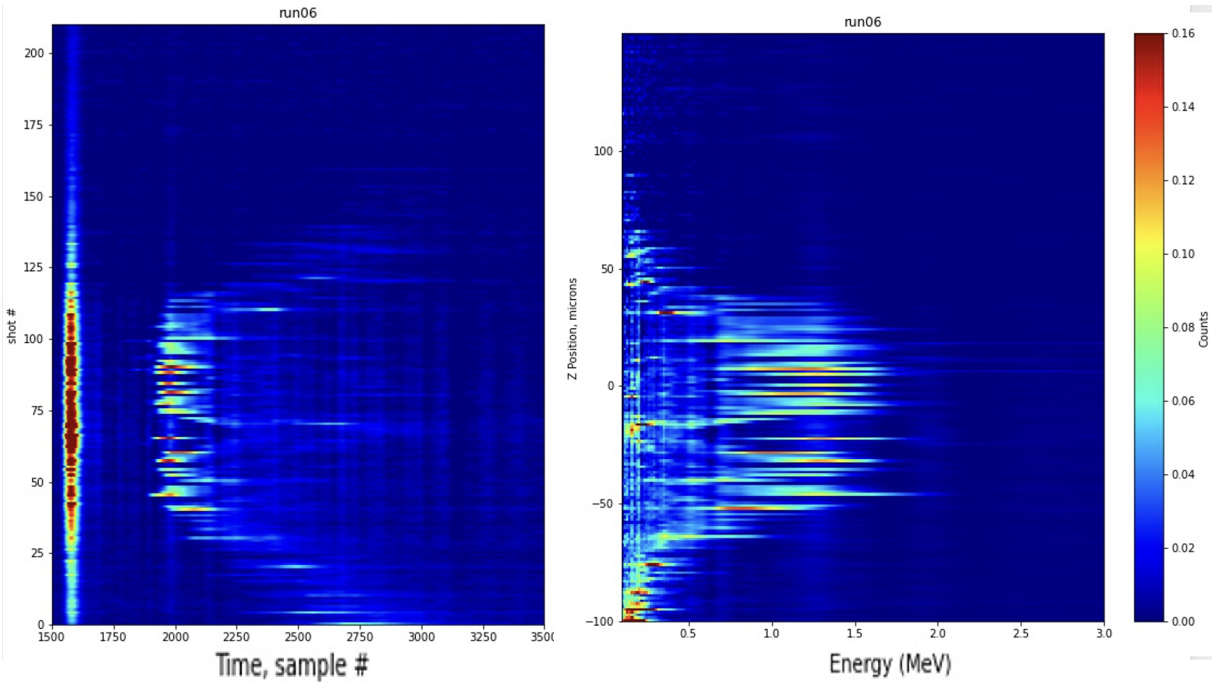


Figure 6.8: (left) X-ray flash can be seen on temporal domain data. (right) It's ripple is exaggerated when converted to the proton energy axis.

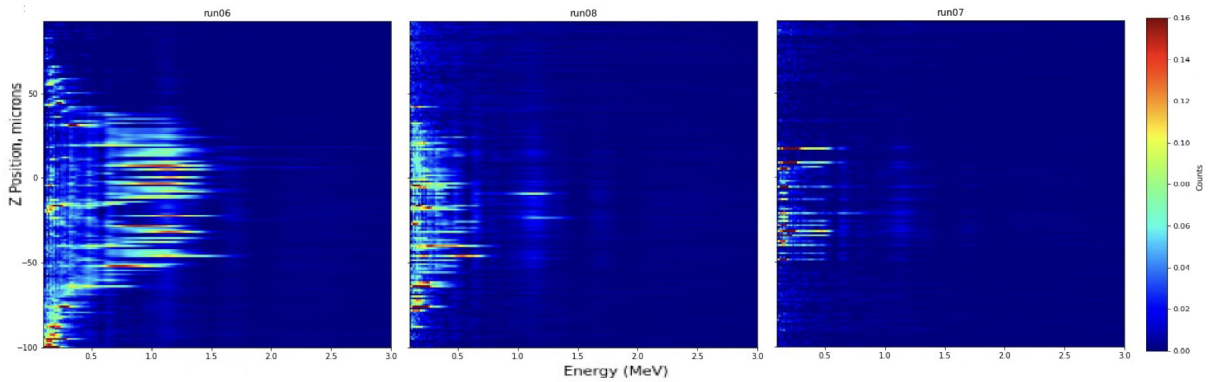


Figure 6.9: With filtering for EMP, the ripples due to cable and connectors can be seen affecting the proton data on all 3 different runs from the experiment. (left) P-polarisation (centre) circular polarisation (right) s-polarisation.

Normalised to the intensity of the x-ray flashes, the train of reflection ripples from the transmission line impedance discontinuities can be more obviously and confidently identified, as shown in Figure 6.10. On some runs, outside of optimum focus, the signal was weak and noisy. However there exist enough information to identify the relationship between the position and intensity of reflection pulses, compared to the x-ray flash intensity.

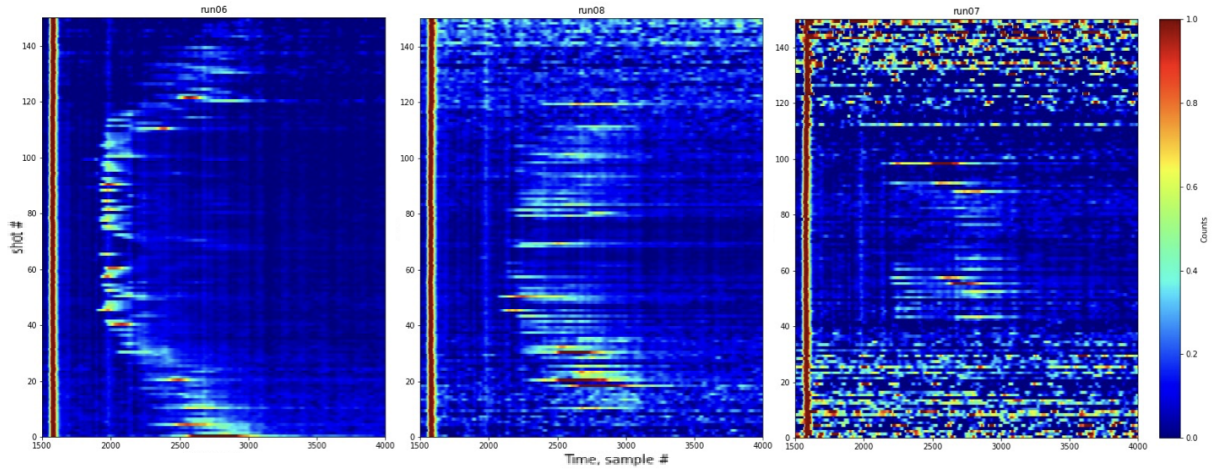


Figure 6.10: Spectral intensity normalised to x-ray flash amplitude. The striations from the x-ray can be identified. (left) P-polarisation (centre) circular polarisation (right) s-polarisation.

A manually selected background mask was applied from some shots with low proton signal but where the x-ray flash remains bright. This needs to be segmented to cover multiple bands, due to the lack of data of a pure x-ray flash without any protons. The result and comparison is shown in Figure 6.11 and Figure 6.12. In Figure 6.11, the temporal domain stripes was visibly removed below noise. The noise comes from the quantisation process of the 8 bit oscilloscope which features less than 5 bits of spurious-free dynamic range. This could be improved with oscilloscopes with low noise analogue front-end and 12 bit ADC. In Figure 6.12, the reflected signals shown clearly on the left, exaggerated by the non-linear temporal-spectral relationship, was removed without significant artifact or spectral resolution loss on the right.

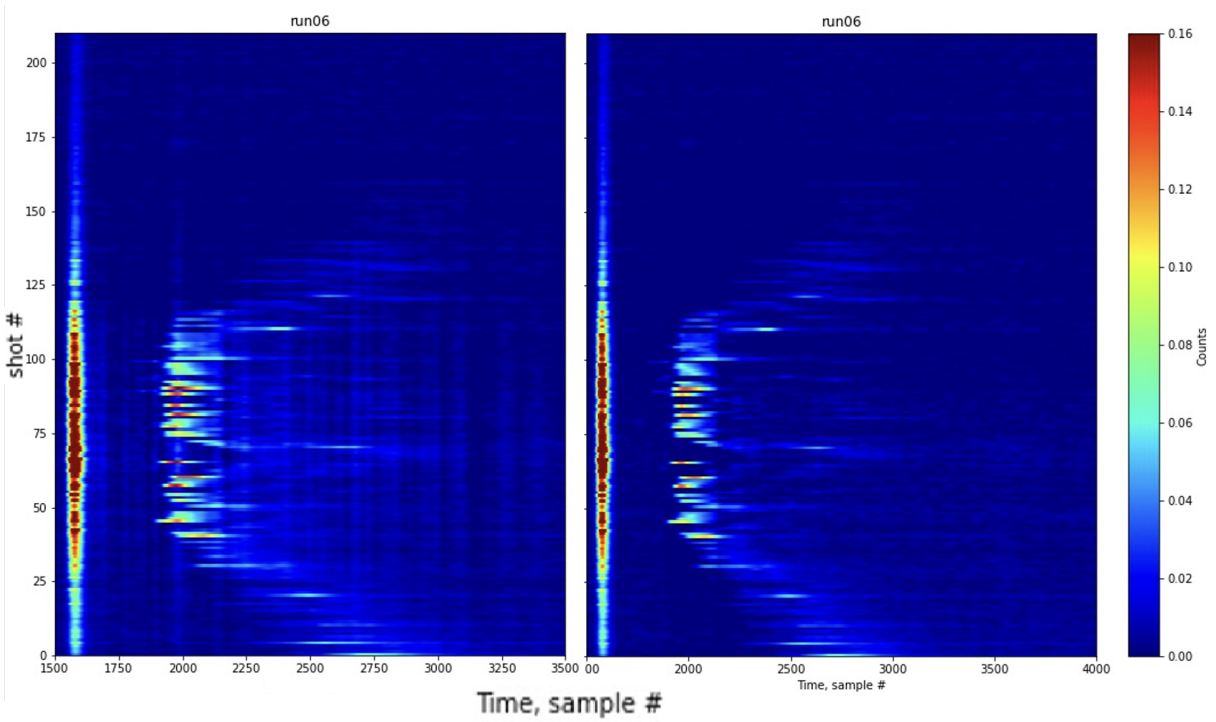


Figure 6.11: Comparison of background removal efficacy on temporal domain samples. Reflections from x-ray flash pulses were removed without introducing significant artifacts or resolution loss. (left) original temporal data (right) after the ripple removal process.

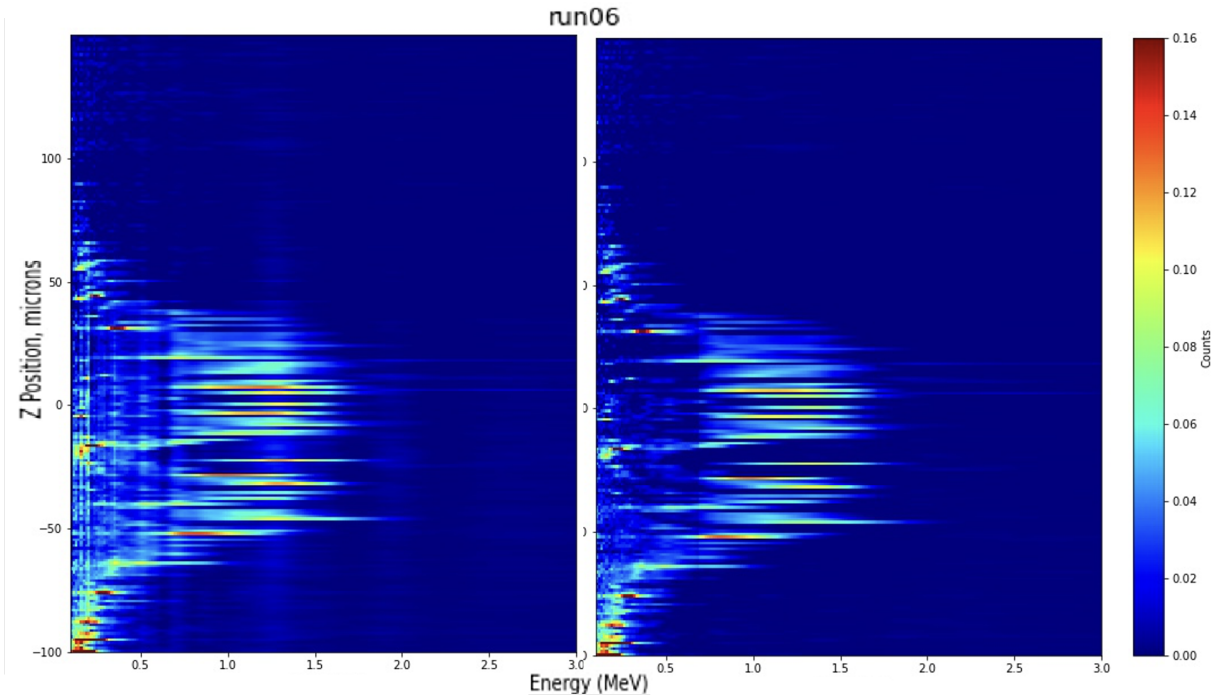


Figure 6.12: Comparison of background removal efficacy on proton spectra. (left) Original spectral data (right) data after the ripple removal process.

6.5 Ion energy comparing 3 different polarisations

A series of focus scans of target position with 3 different polarisation were performed. Raw data before reflection removal is shown in Figure 6.10, which from left to right shows the results with p polarisation, s polarisation, and circular polarisation. This was aimed to provide significantly more robust data compared to previous studies without access to the highly repeatable target delivery system described in Chapter 5 [13].

Shown in Figure 6.13, the best focus proton spectrum, without reflection subtraction, a trend of higher proton energy with higher particle counts can be seen with P polarisation.

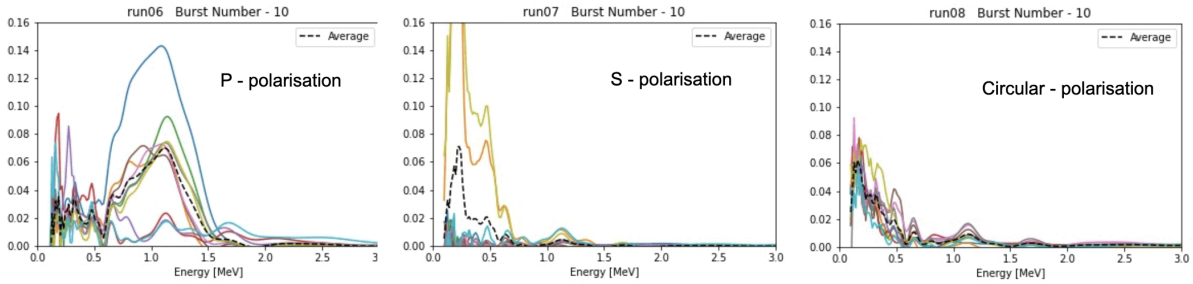


Figure 6.13: Comparison of P, S, and circular polarisation on proton spectra at best focus.

Figure 6.14 illustrates the enhanced reliability of data obtained using a high-repetition laser combined with a target delivery system whose repeatability is significantly below the Rayleigh range. Among the polarisations examined, p-polarisation delivers the highest acceleration performance. Conversely, circular polarisation results in limited acceleration. s-polarisation, on the other hand, yields the lowest proton energy and the poorest stability. This result was inline with literature. However most previous studies have only a few data-points [13].

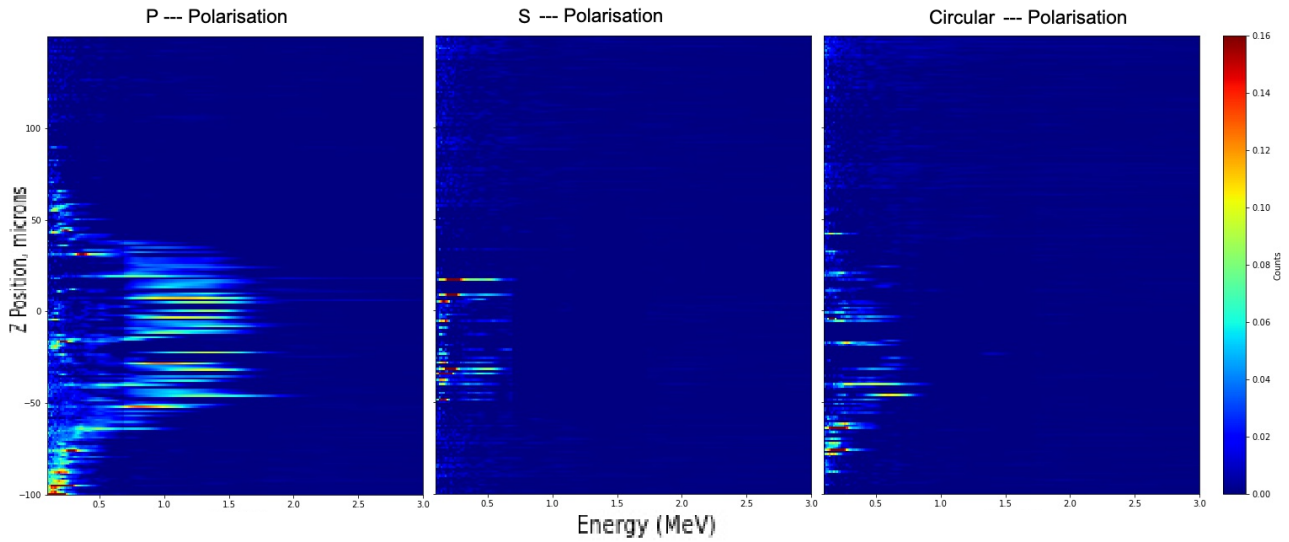


Figure 6.14: Comparison of p, s, and circular polarisation on proton spectra with focus scan waterfall plot.

Figure 6.15 further demonstrates the difference between p, s, and circular polarisation. The maximum energy was taken with the best performing shot envelope, therefore neglecting stability issues and localised poor performance.

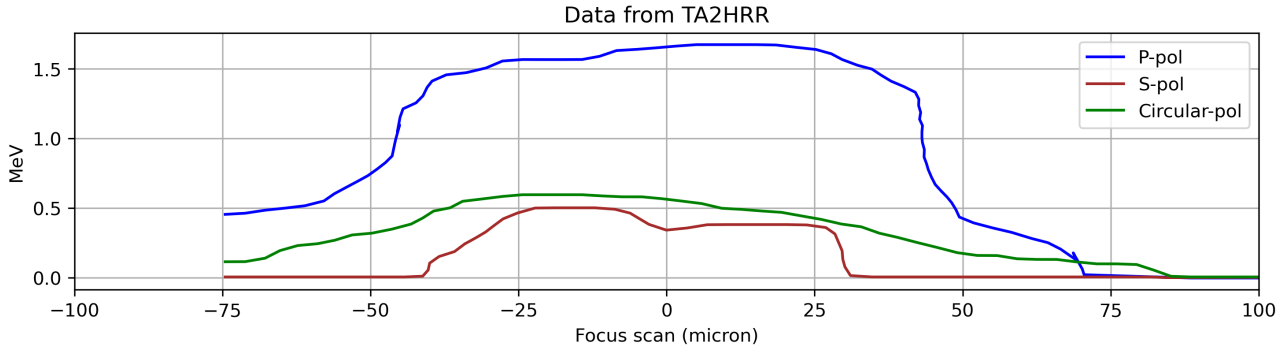


Figure 6.15: Maximum energy envelope for p, s, and circular polarisation.

However if we observe the raw data in Figure 6.16, which is typical among other scans, there is a loss of stability and energy around best focus.

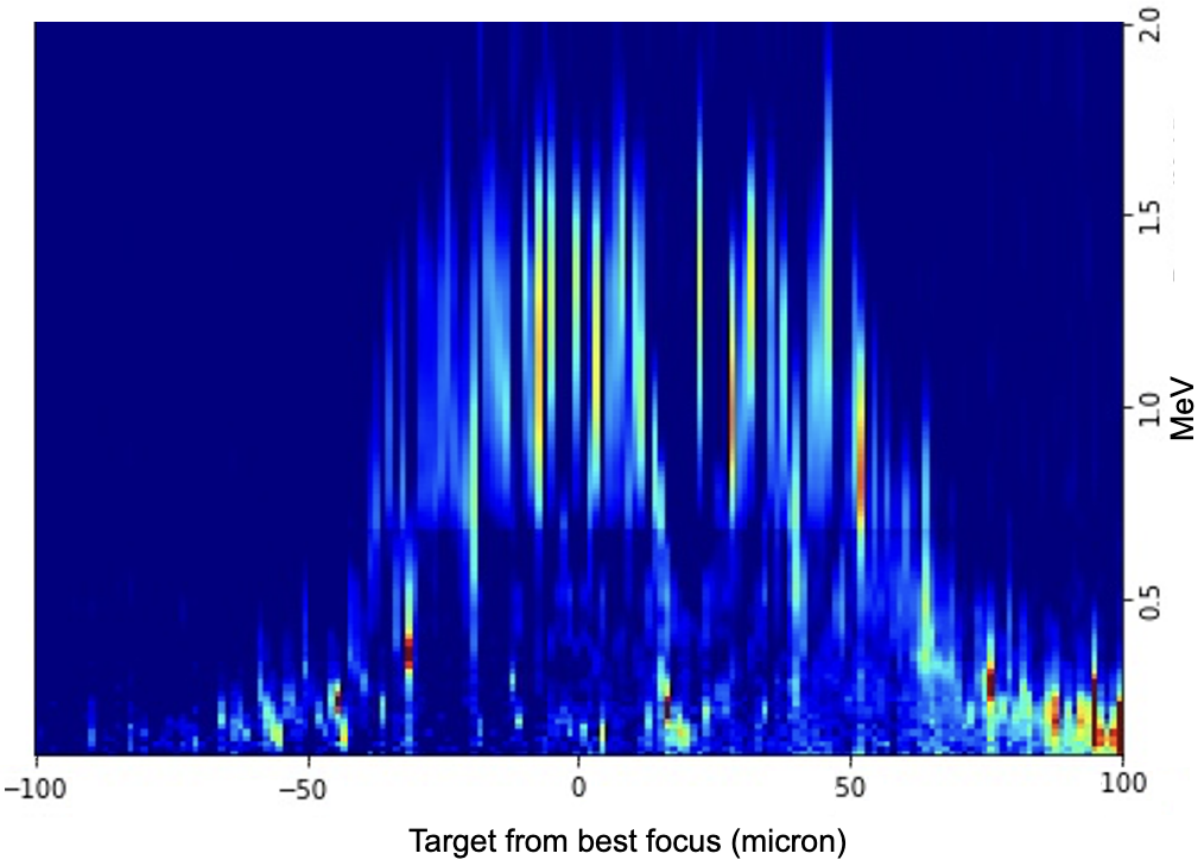


Figure 6.16: Loss of stability and peak energy around best focus, p-polarisation.

The maximum energy does not scale at all with the ponderomotive potential which could be expected to give the plasma temperature (Wilks scaling [14]). However, according to Mora [15], the strength of the generated field also depends on the number of electrons reaching this temperature. Thus the field strength scales to total absorbed energy ($E_{abs} \propto N_{hot} * U_{pond}$).

Assuming the number of electrons heated scales with the area of the target illuminated, then to find E_{abs} we should multiply U_{pond} by the area. This is what is seen in the middle part of the Figure 6.17.

With the relativistically corrected ponderomotive energy scaling times the interaction area [15] at different focal position, given different laser M squared performance, a loss of peak energy can also be seen in Figure 6.17, which is consistent with what is seen in Figure 6.16. This is because for large a_0, relativistic ponderomotive energy only scale with a_0 and therefore $1/\omega_0$ but interaction area scales with ω_0^2. Hence the dip in ion energies close to best focus could be an indication of a loss in performance due to geometric effects, similar to the loss of heating in tightly focused laser spots seen recently [16].

Outside of the main focal spot, $U_{pond} \propto a_0^2 \propto 1/w_0^2$, but $N \propto w_0^2$ and so these two effects cancel, leading to the almost constant spectra over a large range of z. This is maintained up until the field falls below a_0 of around 1 at which point the absorption efficiency falls dramatically and stops the ion acceleration mechanism. The asymmetry around focus could be due to a combination of drift and calibration error.

This is also consistent with Figure 6.17. When the intensity drops too much, outside the highlighted section, the interaction and ionisation process is significantly different and no longer follows the same scaling discussed above. In particular it is likely that the absorption efficiency drops rapidly, which will affect the absorbed energy and thus the proton energy gain. These effects can be further explored by utilising PIC simulations.

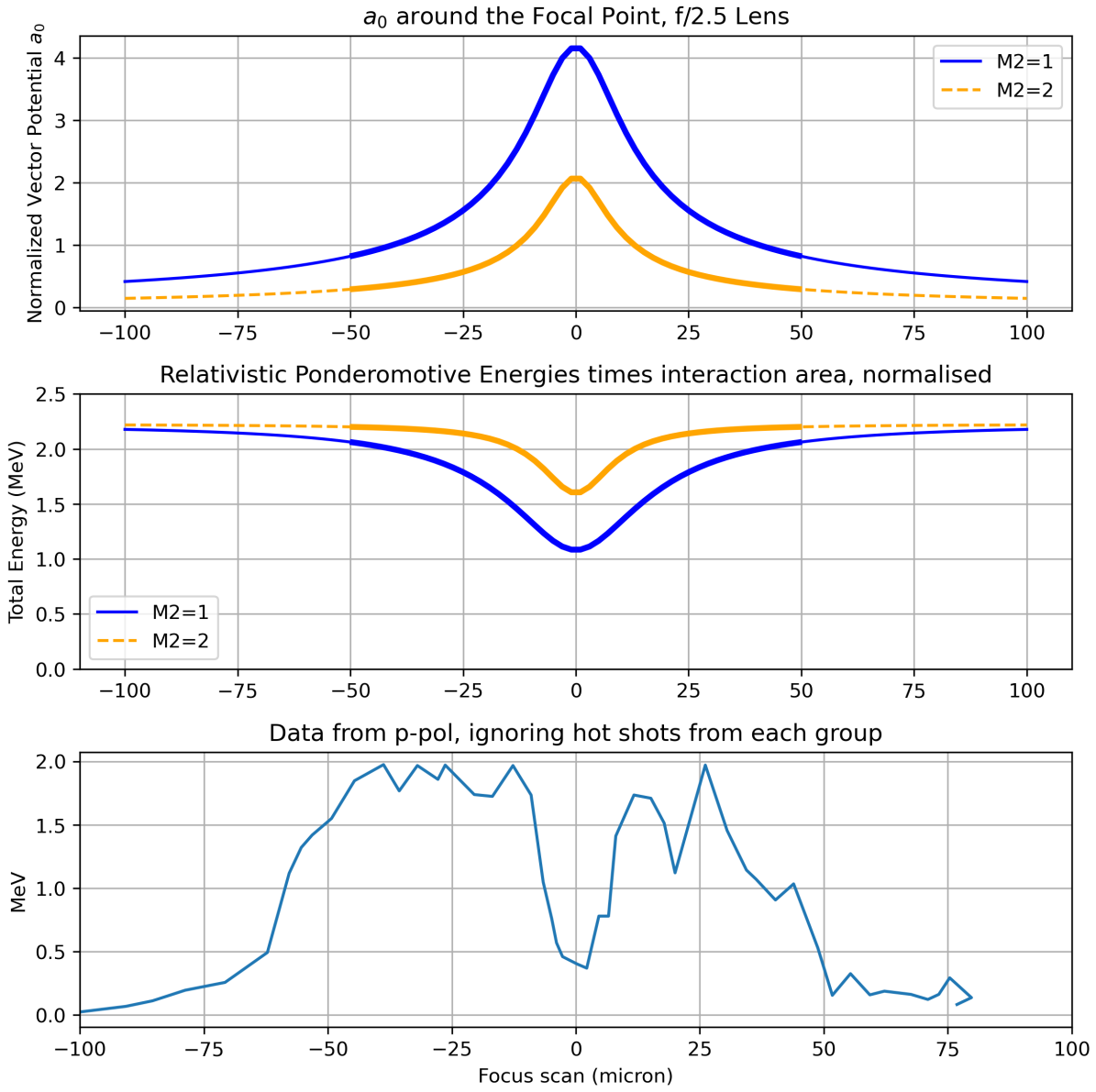


Figure 6.17: Comparison on a_0, ponderomotive energy scaling times the normalised interaction area, and experimental data.

This loss of performance around best focus can also be explained by a combination of a few other effects. One contribution to the discrepancy was from the actual laser M squared was not measured through focus, only best focus images were obtained, large wavefront aberration can produce a relatively constant peak intensity many Rayleigh length away from best focus. Close to best focus, preplasma effects due to laser prepulses would be more important. Hence, the self focusing effect and the pre-plasma density ramp can further broaden the focus scan response. This aspect of the pre-pulse induced density ramp will be investigated in the future with hydro and PIC simulations which due to time constrains were not finished. This can be

further implicated by the sudden lost of stability and sometimes peak energy shown in Figure 6.16.

References

[1] Marco Borghesi. Laser-driven ion acceleration: State of the art and emerging mechanisms. *Nuclear instruments and methods in Physics research section A: Accelerators, spectrometers, detectors and associated equipment*, 740:6–9, 2014.

[2] John T Morrison, Scott Feister, Kyle D Frische, Drake R Austin, Gregory K Ngirmang, Neil R Murphy, Chris Orban, Enam A Chowdhury, and W M Roquemore. MeV proton acceleration at kHz repetition rate from ultra-intense laser liquid interaction. *New Journal of Physics*, 20(2):022001, 2018.

[3] Bixue Hou, John Nees, James Easter, Jack Davis, George Petrov, Alexander Thomas, and Karl Krushelnick. Mev proton beams generated by 3 mJ ultrafast laser pulses at 0.5 kHz. *Applied Physics Letters*, 95(10), 2009.

[4] Muhammad Noaman-ul Haq, Hamad Ahmed, Thomas Sokollik, Lule Yu, Zezhou Liu, Xiaohui Yuan, Fang Yuan, Mohammad Mirzaie, Xulei Ge, Liming Chen, et al. Statistical analysis of laser driven protons using a high-repetition-rate tape drive target system. *Physical Review Accelerators and Beams*, 20(4):041301, 2017.

[5] NP Dover, M Nishiuchi, H Sakaki, Ko Kondo, HF Lowe, MA Alkhimova, EJ Ditter, OC Ettlinger, A Ya Faenov, M Hata, et al. Demonstration of repetitive energetic proton generation by ultra-intense laser interaction with a tape target. *High Energy Density Physics*, 37:100847, 2020.

[6] N Xu, MJV Streeter, OC Ettlinger, H Ahmed, S Astbury, M Borghesi, N Bourgeois, CB Curry, SJD Dann, NP Dover, et al. Versatile tape-drive target for high-repetition-rate laser-driven proton acceleration. *High Power Laser Science and Engineering*, 11:e23, 2023.

[7] M Oron. A static field mass spectrograph for laser induced plasma experiments. *Nuclear Instruments and Methods*, 139:235–237, 1976.

[8] R. Prasad, D. Doria, S. Ter-Avetisyan, P.S. Foster, K.E. Quinn, L. Romagnani, C.M. Brenner, J.S. Green, P. Gallegos, M.J.V. Streeter, D.C. Carroll, O. Tresca, N. Dover, C.A.J.

Palmer, J. Schreiber, D. Neely, Z. Najmudin, P. McKenna, M. Zepf, and M. Borghesi. Calibration of thomson parabola—mcp assembly for multi-mev ion spectroscopy. *Nuclear Instruments and Methods in Physics Research Section A: Accelerators, Spectrometers, Detectors and Associated Equipment*, 623(2), 2010. 1rs International Conference on Frontiers in Diagnostics Technologies.

[9] RH Hughes, RJ Anderson, CK Manka, MR Carruth, LG Gray, and JP Rosenfeld. Ion beams from laser-generated plasmas. *Journal of Applied Physics*, 51(8):4088–4093, 1980.

[10] Jay S Pearlman. Faraday cups for laser plasmas. *Review of Scientific Instruments*, 48(8):1064–1067, 1977.

[11] Martina Salvadori, F Consoli, C Verona, M Cipriani, MP Anania, PL Andreoli, P Antici, F Bisesto, G Costa, G Cristofari, et al. Accurate spectra for high energy ions by advanced time-of-flight diamond-detector schemes in experiments with high energy and intensity lasers. *Scientific Reports*, 11(1):3071, 2021.

[12] James R Andrews. Time domain reflectometry. In *Proceedings of the Symposium on Time Domain*, 1994.

[13] C Scullion, D Doria, L Romagnani, A Sgattoni, K Naughton, DR Symes, P McKenna, A Macchi, M Zepf, S Kar, et al. Polarization dependence of bulk ion acceleration from ultrathin foils irradiated by high-intensity ultrashort laser pulses. *Physical review letters*, 119(5):054801, 2017.

[14] SC Wilks, AB Langdon, TE Cowan, M Roth, M Singh, S Hatchett, MH Key, D Pennington, A MacKinnon, and RA Snavely. Energetic proton generation in ultra-intense laser–solid interactions. *Physics of Plasmas*, 8(2):542–549, 2001.

[15] P. Mora. Thin-foil expansion into a vacuum. *Phys. Rev. E*, 72:056401, 2005.

[16] NP Dover, M Nishiuchi, H Sakaki, Ko Kondo, MA Alkhimova, A Ya Faenov, M Hata, N Iwata, H Kiriyama, JK Koga, et al. Effect of small focus on electron heating and

proton acceleration in ultrarelativistic laser-solid interactions. *Physical Review Letters*, 124(8):084802, 2020.

Chapter 7

Conclusion and Future work

7.1 Conclusions

The design and development of a high repetition rate Ti:Sapphire laser amplifier system, along with a complementary solid target delivery system, have yielded satisfactory results and indicate scalability.

12.26 mJ of 0.91 % stability was achieved from the regenerative amplifier, with high vacuum cryogenic crystal cooling supporting many millions of shots, across one year operating period, without measurable deterioration of optical surfaces.

A diode pumped 1064 nm amplifier operating at 690 mJ was also operated without optical deterioration for more than one year, with depolarisation compensation optics.

Multi-pass amplifier with cryogenic cooling was operated at 20 times energy gain and 60 mJ output energy. This was partially characterised without an adequate seeding (less than 3 mJ was available) however performed with expected longevity. The crystal cooling apparatus and multi-pass optical architecture is being upgraded for better cooling performance and vacuum level during the writing of this thesis. It is expected to achieve 150 mJ with 8 mJ seeding.

This laser system will be suitable for parametric optimisation exploring many different parameter space with the help of machine learning optimisation algorithms. The energy jitter is well characterised to have not only good rms stability, but also peak to peak jitter, therefore converge rate and signal to noise ratio of various legacy optimisation algorithms is expected

to be better than previously achievable. Parameter such as target radius, pulse temporal phase, wavefront, pre-pulse strength, as well as target shaping pulse condition can be explored simultaneously.

Various applications involving high repetition rate lasers such as medical radiography and therapy, radioisotope generation for medical diagnostics can be studied using the laser system and targetry.

The experimental proton acceleration using the Astra laser and the tape target developed by the author has shown robust polarization comparison data and observed focus scan features that could have been overlooked previously due to the absence of a high repetition rate and a stable target.

The initial findings using the tape drive target suggest the potential for ion acceleration using a multi-beam non-coherent combined focal spot generated by an array of lasers. However, additional Particle-in-Cell (PIC) simulations are needed to provide further support for these possibilities.

7.2 Future works

7.2.1 Regenerative amplifier

Cavity stability, robustness against drift and vibration, will be explored in the future, alone with higher pump energy and contrast enhancement techniques such as saturable absorber and programmable gain filter. Better online diagnostics for amplifier performance tracking, vibration synchronisation, drift compensation and auto alignment will be experimented to provide better usability.

7.2.2 Multi-pass amplifier

Brewster-cut crystal with higher damage threshold will be explored to extract more energy while pumping in deeper saturation to improve stability.

Higher pump energy towards 1 J at 100 Hz output has already been designed, but due to

other limitations is yet to be procured and implemented.

7.2.3 Tape target

Utilisation of programmable torque control servo motor and drive unit will be explored to provide better operating robustness. Structures with thermally invariant materials such as technical ceramics and alloys will be explored to further reduce drift.

7.2.4 ToF

The Time-of-Flight diagnostics were performed with off-the-shelf oscilloscopes. This limited the data throughput to less than a few Hz due to the architecture of sampling oscilloscope and its data transfer rate. FPGA with fast ($\geq 100Gsps$) ADC [1][2] and accurate timing trigger can provide significantly higher repetition rate while also enabling real-time data processing to well beyond 1 kHz with FPGA performing the application domain down-sampling [3].

A signal chain from the diamond detector to ADC can be built completely from phase-stable coax cables, while paying close attention to impedance discontinuity of the connectors such as vacuum feedthroughs and coax to micro-strip transmission line conversion on the printed circuit boards. Connectors with single mode supporting the complete sampling analogue bandwidth should be chosen. For modern oscilloscope, with analogue bandwidth typically higher than 50 GHz, a type V (1.85 mm) connector with air dielectric should be chosen to provide a flat frequency response, further minimising overshoot and undershoot on impulses.

7.2.5 Target position on-shot monitoring

In the experiment described, the target focus position was determined by using the open loop translation stage commanded position. This was only verified with plasma self emission centroid. This poses uncertainty due to the size and shape of self emission plasma, as well as its brightness.

The target position could be monitored with a hetrodyne inteferometer operating in retro-reflecting mode. This setup was attempted during the last experimental run. However due to equipment limitations this was not successful.

7.2.6 High repetition rate support diagnostics

Cameras and spectrometers cannot currently run at high repetition rate without generating vast amount of data, overwhelming the computing setup commonly found in laser labs. A typical setup with 20 different 10 megapixel cameras running at 1 kHz would generate 3.2 terabits per seconds, although this can be easily handled by modern computing equipment with PCIexpress interface and solid-state storage arrays, a more budget friendly option would be utilising massively parallel capability of FPGA arrays. These FPGAs can sample the images, and perform filtering, down sampling in real time to only the required information such as beam centroid, electron or proton spectra, and saving them at significantly lower data rates.

References

[1] Viduneth Ariyarathna, Arjuna Madanayake, and Josep M Jornet. Toward real-time software-defined radios for ultrabroadband communication above 100 ghz [application notes]. *IEEE Microwave Magazine*, 24(8):50–59, 2023.

[2] Dimitrios Siafarikas and John L Volakis. Towards direct rf sampling for digital communications. *IEEE Microwave Magazine*, 2023.

[3] Joachim Meyer, Simon Menzel, Michael Dreschmann, Rene Schmogrow, David Hillerkuss, Wolfgang Freude, Juerg Leuthold, and Juergen Becker. Ultra high speed digital down converter design for virtex-6 fpgas. In *OFDM 2012; 17th International OFDM Workshop 2012 (InOWo'12)*, pages 1–5. VDE, 2012.